

Institut für Theoretische Physik
Fakultät Mathematik und Naturwissenschaften
Technische Universität Dresden

**Ab-Initio Molecular Dynamics Studies Of
Laser- And Collision-Induced Processes In
Multielectron Diatomics,
Organic Molecules And Fullerenes
Ionization, Isomerization, Fragmentation and Fusion**

Dissertation
zur Erlangung des akademischen Grades
Doctor rerum naturalium
(Dr. rer. nat.)

vorgelegt von
Jan Handt
geboren am 18. Juli 1978 in Lutherstadt Wittenberg

Dresden 2010



Eingereicht am 15.01.2010

1. Gutachter: Prof. Dr. Rüdiger Schmidt
2. Gutachter: Prof. Dr. Jan-Michael Rost

Verteidigt am 18.10.2010

Abstract

This work presents applications of an ab-initio molecular dynamics method, the so-called non-adiabatic quantum molecular dynamics (NA-QMD), for various molecular systems with many electronic and nuclear degrees of freedom. Thereby, the nuclei will be treated classically and the electrons with time-dependent density functional theory (TD-DFT) in basis expansion. Depending on the actual system and physical process, well suited basis sets for the Kohn-Sham orbitals has to be chosen. For the ionization process a novel absorber acting in the energy space as well as additional basis functions will be used depending on the laser frequency.

In the **first** part of the applications, a large variety of different **laser**-induced molecular processes will be investigated. This concerns, the orientation dependence of the ionization of multielectronic diatomics (N_2 , O_2), the isomerization of organic molecules (N_2H_2) and the giant excitation of the breathing mode in fullerenes (C_{60}).

In the **second** part, fullerene-fullerene **collisions** are investigated, for the first time in the whole range of relevant impact velocities concerning the vibrational and electronic energy transfer ("stopping power"). For low energetic (adiabatic) collisions, it is surprisingly found, that a two-dimensional (!), phenomenological collision model can reproduce (even quantitatively) the basic features of fusion and scattering observed in the fully microscopic calculations as well as in the experiment. For high energetic (nonadiabatic) collisions, the electronic and vibrational excitation regimes are predicted, leading to multifragmentation up to complete atomization.

Contents

1	Introduction	7
2	Theory: Ab-initio Molecular dynamics	11
2.1	Molecular dynamics methods	11
2.2	Adiabatic Quantum Molecular dynamics (QMD)	16
2.3	Nonadiabatic Quantum Molecular dynamics (NA-QMD)	17
2.3.1	The mixed classical-quantum equations of motion	17
2.3.2	NA-QMD and ionization	20
2.3.3	Definition of physical properties in the NA-QMD approach	23
2.3.4	Numerics	25
3	Laser-induced dynamics	29
3.1	Ionization of diatomics	29
3.1.1	The ground state properties of N ₂ and O ₂	31
3.1.2	Wavelength Dependence of the Ionization	35
3.1.3	Orientation Dependence of the Ionization	37
3.2	Isomerization and fragmentation of organic molecules	42
3.2.1	The ground state properties of the diimide molecule N ₂ H ₂	43
3.2.2	Isomerization via the 1st excited state	47
3.2.3	Selective fragmentation via higher excited states	51
3.3	Giant collective vibrational excitation in fullerenes	53
3.3.1	The ground state properties of C ₆₀	54
3.3.2	Resonant and nonresonant laser excitation	59
3.3.3	Laser excited breathing mode	61
3.3.4	Pump-probe scenario	63
4	Collision-induced fullerene dynamics	69
4.1	Adiabatic dynamics	69
4.1.1	C ₆₀ + C ₆₀ : Fusion versus scattering	70
4.1.2	A two-dimensional classical trajectory model	75
4.1.3	C ₆₀ + C ₆₀ : Fusion versus scattering for finite temperatures	83
4.1.4	C ₇₀ + C ₇₀ : Fusion versus scattering	87
4.2	Nonadiabatic dynamics of fullerene-fullerene collisions	92
4.2.1	Fragmentation regimes in C ₆₀ + C ₆₀ collisions	92
4.2.2	Dependence on the impact parameter	94
4.2.3	Comparison with Ion-Fullerene collisions	95
5	Outlook	97

Appendix A	99
A.1 Number of excited electrons in TD-DFT	99
A.2 Visualization of the electron dynamics	101
A.2.1 The electron localization function (ELF)	101
A.2.2 The dimers N ₂ and O ₂	102
A.2.3 The C ₆₀ molecule	104
Appendix B	107
B.1 Normal mode analysis	107
B.2 Normal modes of C ₆₀	109
Appendix C	111
C.1 Classical trajectory model for asymmetrical fullerene-fullerene collisions . . .	111
C.2 Analytical solution for symmetrical fullerene-fullerene collisions	113
Bibliography	115

1 Introduction

During the last two decades, large advances have been made in the experimental study of nonadiabatic processes in atoms, molecules and clusters, e.g. above-threshold ionization (ATI) [1] resp. above-threshold dissociation (ATD) [2], high harmonic generation (HHG) [3], charge resonant enhanced ionization (CREI) [4], molecular alignment [5], selective bond breaking [6] or Coulomb explosion [7]. Especially, the rapid progress in the creation and manipulation of femtosecond laser pulses with high intensities ($10^{12} - 10^{15} \frac{\text{W}}{\text{cm}^2}$) has lead to the new field of femtosecond physics [8] or femtochemistry [9]. Ultrashort light pulses can now be used to follow in real-time the primary events of many chemical but also physical or biological processes. Pump-probe experiments allow for the study the vibrational dynamics in diatomics and more complex molecules on the femtosecond scale using momentum imaging techniques for electrons, e.g. time-resolved photoelectron spectroscopy (TRPES) [10], and ion fragments [11–13].

In addition, also the control of atomic and molecular systems, e.g. chemical reactions, is the subject of recent research. In optimal control experiments the molecular response is manipulated by adaptive closed-loop feedback schemes using phase-shaped laser pulses in order to optimize chemical reactions [14, 15]. In Coherent Control [16] resp. Quantum Control [17] schemes, the electronic or nuclear wave packets dynamics can be manipulated by a sequence of short laser pulses with tuned relative phases, which steer the system into the desired quantum state. On the attosecond time scale, it has become possible to use High Harmonic Generation, both to generate attosecond XUV pulses [18] and to study molecular properties [19, 20].

On the other hand, ab initio calculations of the dynamics of atomic and molecular systems with many electronic resp. nuclear degrees of freedom is inherently a challenging task. Up to now, at maximum the five-dimensional time dependent Schrödinger equation (TDSE) can be propagated numerically only on large scaled parallel computers. This has been done for the laser-driven He-atom [21], e.g. to compare perturbation theory for the N-photon single ionization with numerics [22]. For molecular systems, only the smallest molecules, the D_2^+ in a laser field, has been treated fully quantum mechanically without any constraint, very recently [23, 24].

Therefore, the vibrational motion is usually approximated by a classical treatment of the nuclei in molecular dynamics (MD) methods [25]. The coupling to the multielectron system is still a tough problem (see Sec. 2.1 for an overview). The calculation of the time-independent electronic and atomic structure, however, can be done meanwhile by many quantum chemical methods like the Hartree-Fock approximation, or more sophisticated

methods like configuration-interaction (CI), multiconfigurational self-consistent field theory (MCSCF), or coupled-cluster theory (CC) [26]. However, all these methods are dealing with the many electron wavefunction in one or another way. Therefore, their applications are limited due to the large computational effort, especially in combination with molecular dynamics or even explicitly time-dependent situations. There are, however, a few methods, for example the time-dependent multiconfiguration theory [27], describing the multielectron dynamics of a molecule in laser fields. Much more efficient, however, is the use of a theory equivalent to the TDSE – the time-dependent density functional theory (TD-DFT) [28], which can cope with the many electron systems by reducing the problem of the multidimensional manybody wavefunction to the propagation of the one-particle density.

The first combination of TD-DFT with classical MD has been developed and realized by Saalman and Schmidt [29]. This method was named Non-Adiabatic Quantum Molecular Dynamics (NA-QMD). With this theory it became possible to treat simultaneously and self-consistently (quantum-mechanical) electronic excitations and (classical) nuclear motion in finite atomic many-body systems. From the historical point of view, the NA-QMD of Saalman and Schmidt represented the first attempt to generalize the till then existing QMD-methods (like the Car-Parrinello Theory [30]) to couple explicitly quantum-mechanically electronic excitations and transitions (i.e. non-adiabatic processes) with classical nuclear motion. So it became generally possible to investigate non-adiabatic processes in atomic many-body systems on a fully microscopic basis, like the electronic and nuclear "stopping power" in metallic clusters [31] and fullerenes [32], the charge transfer in ion-cluster collisions [33–36], or the reaction mechanism in collisions between ions and molecules or clusters [37–39] including an attempt to take into account quantum effects in the nuclear motion [40]. This early variant of the NA-QMD theory, however, was restricted to closed systems, because the classical equations of motion have been derived from the total energy conservation, as done in the theory of nuclear heavy-ion collisions [41,42]. Furthermore, it was an approximative (i.e. non ab-initio) method, because the exchange-correlation potential in the time-dependent Kohn-Sham equations has been approximated by a sum of atomic potentials [29].

The present ab-initio version of the NA-QMD and its extensions to open systems (to include e.g. also laser interactions) have been developed by Kunert and Schmidt [43,44]. Here, the classical equations of motion are obtained by the general variational principle leading to additional (velocity-dependent) correction terms in the forces acting on the nuclei. For the exchange correlation potential the time-dependent Local Density Approximation (LDA) as well as the Spin-dependent LDA (LSDA) have been numerically realized. Later, the whole formalism has been extended to describe also many-electron ionization [45–47]. However, up to now, most of the applications of the ab-initio NA-QMD are restricted to one or two electron systems like H_2^+ or H_2 in strong laser fields [43,48,49]. The isomerization of ethylene in femtosecond laser pulses has been treated as well [50]. Multielectron ionization, large

clusters in strong laser pulses, or non-adiabatic cluster collisions have not been examined up to now, but, represent the main topics of the present thesis.

The outline of the thesis is as follows:

In Chapter 2, first a general overview of different (ab-initio) molecular dynamics methods is presented (Sect. 2.1). The basic framework of QMD and NA-QMD are summarized in Sect. 2.2 and 2.3, respectively.

In Chapter 3, a large variety of different **laser**-induced molecular processes will be investigated. This concerns, the orientation dependence of the ionization of multielectronic diatomics (N_2 , O_2) [51], the isomerization of organic molecules (N_2H_2) [52] and the giant excitation of the breathing mode in fullerenes (C_{60}) [53].

In Chapter 4, fullerene-fullerene **collisions** are investigated, for the first time in the whole range of relevant impact velocities concerning the vibrational and electronic energy transfer ("stopping power"). For low energetic (adiabatic) collisions, it is surprisingly found, that a two-dimensional (!), phenomenological collision model can reproduce (even quantitatively) the basic features of fusion and scattering observed in the fully microscopic calculations as well as in the experiment [54,55]. For high energetic (nonadiabatic) collisions, the electronic and vibrational excitation regimes are predicted, leading to multifragmentation up to complete atomization [56].

Most of the technical details or analytical derivations are presented in the Appendices A-C. Among them, the visualization of the electronic structure and dynamics with the concept of the electron localization function (ELF) [57] will appear to be a very useful tool to display chemical bonds [58] (Appendix A.2).

The key point of the QMD or NA-QMD formalism represents the appropriate choice of the basis [46] in which the Kohn-Sham orbitals are expanded. Therefore, for each application presented in the thesis this important point will be discussed separately and in detail.

Throughout this work atomic units are used ($\hbar = e = m_e = 1\text{a.u.}$) if not stated otherwise.

2 Theory: Ab-initio Molecular dynamics

In this chapter we will present the molecular dynamics approach which allows the study of large systems, e.g. organic molecules or fullerenes with all electronic and nuclear degrees of freedom (DOF). At first we will give an overview of the large field of molecular dynamics methods in Section 2.1 in general. Secondly, we will summarize some results of the (adiabatic) quantum molecular dynamics (QMD) in Section 2.2, and at last the nonadiabatic quantum molecular dynamics approach (NA-QMD), developed in our group [44], will be presented in more detail.

2.1 Molecular dynamics methods

Molecular dynamics (MD) simulations are a powerful tool facilitating the understanding of various molecular processes. For reasons of simplicity the interaction with external fields is ignored here. We will refer to this case later. To illustrate the molecular dynamics techniques, we will show the main approach starting with the full nonrelativistic Hamiltonian of the atomic many-body system (without coupling to external fields):

$$H(\mathbf{r}, \mathbf{p}; \mathbf{R}, \mathbf{P}) = T(\mathbf{P}) + H_{el}(\mathbf{r}, \mathbf{p}; \mathbf{R}), \quad (2.1)$$

with the kinetic energy of the nuclei

$$T(\mathbf{P}) = \sum_{A=1}^{N_i} \frac{\mathbf{P}_A^2}{2M_A}, \quad (2.2)$$

and the electronic Hamiltonian ($\mathbf{r} = [\mathbf{r}_1 \dots \mathbf{r}_{N_e}]$)

$$H_{el}(\mathbf{r}, \mathbf{p}; \mathbf{R}) = \underbrace{\sum_{i=1}^{N_e} \frac{\mathbf{p}_i^2}{2}}_{T(\mathbf{p})} + \underbrace{\sum_{i<j}^{N_e} \frac{1}{|\mathbf{r}_i - \mathbf{r}_j|}}_{V(\mathbf{r})} + \underbrace{\sum_{i=1}^{N_e} \sum_{A=1}^{N_i} \frac{-Z_A}{|\mathbf{r}_i - \mathbf{R}_A|}}_{V_{int}(\mathbf{r}, \mathbf{R})} + \underbrace{\sum_{A<B}^{N_i} \frac{Z_A Z_B}{|\mathbf{R}_A - \mathbf{R}_B|}}_{U(\mathbf{R})}, \quad (2.3)$$

which is the sum of the kinetic energy of the electrons $T(\mathbf{p})$, the electron-electron interaction $V(\mathbf{r})$, the electronic-ion potential $V_{int}(\mathbf{r}, \mathbf{R})$, and the ion-ion repulsion potential $U(\mathbf{R})$ ¹.

¹The potential $U(\mathbf{R})$ does not depend on the electronic coordinates, and is only a constant for fixed nuclei. It does not change the electronic eigenvalue problem and is only included in the electronic Hamiltonian for the definition of the Born-Oppenheimer energy surfaces (see below).

To solve the many-body Schrödinger equation for $3N_e$ electronic coordinates \mathbf{r} and $3N_i$ nuclear coordinates ($\mathbf{R} = [\mathbf{R}_1 \dots \mathbf{R}_{N_i}]$)

$$i\frac{\partial}{\partial t}\Psi(\mathbf{r}, \mathbf{R}, t) = H(\mathbf{r}, \mathbf{p}; \mathbf{R}, \mathbf{P})\Psi(\mathbf{r}, \mathbf{R}, t), \quad (2.4)$$

it is common to use the *Born-Oppenheimer ansatz*

$$\Psi(\mathbf{r}, \mathbf{R}, t) = \sum_i \phi_i(\mathbf{r}; \mathbf{R})\Omega_i(\mathbf{R}, t) \quad (2.5)$$

for the total molecular wave function $\Psi(\mathbf{r}, \mathbf{R}, t)$. The eigenfunctions $\phi_i(\mathbf{r}; \mathbf{R})$ of the electronic system for fixed nuclear positions are defined by

$$H_{el}\phi_i(\mathbf{r}; \mathbf{R}) = E_i(\mathbf{R})\phi_i(\mathbf{r}; \mathbf{R}), \quad (2.6)$$

form a complete (orthonormalized) basis in the Hilbert space. Note, that the eigenfunctions and the Born-Oppenheimer energies $E_i(\mathbf{R})$ depend parametrically on the nuclear position. Inserting the Born-Oppenheimer ansatz (2.5) in the many-body Schrödinger equation (2.4), multiplying with $\phi_j^*(\mathbf{r}; \mathbf{R})$ and integrating over the electronic coordinates, gives a set of coupled partial differential equations for the nuclear wave functions $\Omega_i(\mathbf{R}, t)$:

$$i\frac{\partial}{\partial t}\Omega_j(\mathbf{R}, t) = [T(\mathbf{P}) + E_j(\mathbf{R})]\Omega_j(\mathbf{R}, t) + \sum_i C_{ji}\Omega_i(\mathbf{R}, t). \quad (2.7)$$

The nonadiabatic coupling elements C_{ji} are defined by

$$C_{ji} = -\sum_{A=1}^{N_i} \langle \phi_j | \frac{1}{2M_A} \frac{\partial^2}{\partial \mathbf{R}_A^2} | \phi_i \rangle - \sum_{A=1}^{N_i} \frac{1}{M_A} \langle \phi_j | \frac{\partial}{\partial \mathbf{R}_A} | \phi_i \rangle \frac{\partial}{\partial \mathbf{R}_A}, \quad (2.8)$$

where the bra-ket notation indicates only integration over the electronic coordinates. The MD approaches can be classified into *adiabatic* and *nonadiabatic* molecular dynamics. In the adiabatic approach the electronic system is fixed to a certain electronic state ϕ_i , in most cases the ground state, whereas in the nonadiabatic case the system can change its electronic state. In the first case, also called *Born-Oppenheimer approximation*, the nonadiabatic coupling elements C_{ji} are set to zero, which allows us to separate the nuclear motion on each electronic potential energy surface (PES) $E_i(\mathbf{R})$:

$$i\frac{\partial}{\partial t}\Omega_i(\mathbf{R}, t) = [T(\mathbf{P}) + E_i(\mathbf{R})]\Omega_i(\mathbf{R}, t). \quad (2.9)$$

For many chemical reactions the ground state energy surface $E_0(\mathbf{R})$ is well separated from higher lying electronic states, and therefore, equation (2.9) (with $i = 0$) is applicable². Near

²A decision between adiabatic and nonadiabatic processes can be made with the so-called Massey parameter [59] $\epsilon = \frac{(E_i(\mathbf{R}) - E_j(\mathbf{R}))l}{\dot{R}}$, where l is a characteristic length of the nuclear motion. For values $\epsilon \gg 1$, i.e. large energy gaps and small nuclear velocities \dot{R} , nonadiabatic effects are negligible.

avoided crossings, respectively conical intersections, the Born-Oppenheimer approximation fails.

A further approximation in standard molecular dynamics is the treatment of the nuclei as classical particles governed by the Newton equation

$$M_A \ddot{\mathbf{R}}_A = -\frac{\partial}{\partial \mathbf{R}_A} E(\mathbf{R}), \quad (2.10)$$

which makes it possible to study systems with many hundreds or thousands degrees of freedom if the potential surface $E(\mathbf{R})$ is known [25]. The reduction of the quantum picture (Eq. (2.9)) to the classical picture (Eq. (2.10)) can be achieved in the classical limit $\hbar \rightarrow 0$, for a detailed derivation see reference [60]. Thereby, the nuclear density $|\Omega(\mathbf{R})|^2$ is replaced by a product of delta functions $\prod_i \delta(\mathbf{R}_i - \mathbf{R}_i(t))$ located at the actual positions $\mathbf{R}_i(t)$ of the classical nuclei.

We will now present the different adiabatic molecular dynamics methods, an overview can be found in [60, 61]. In the *classical molecular dynamics* the interaction between nuclei and electrons, i.e. the potential $E(\mathbf{R})$ in Eq. (2.10), is computed by using predefined potentials, which have been obtained either from empirical data (force-field approaches) or ab-initio electronic structure calculations. Sophisticated methods have been developed to approximate the interatomic potentials by analytical two-body or also three-body potentials including short and long-ranged parts. By replacing the electronic degrees of freedom by the parametrized potentials very large system can be investigated, e.g. the dynamics of solids [62] or fluids [63]. However, the drawback is the need for many different interatomic potentials for all kinds of combinations of atoms in various molecules. Furthermore the bond characteristics are fixed during the simulation, allowing for example no change from single to double bonds.

The drawback for the so-called "chemically complex" reactions could be circumvented by using the global potential surface from ab-initio methods, which is in most cases impossible due to the so-called "dimensionality bottleneck". This means, that due to the high dimensionality in the N-body problem, a mapping of the potential needs $\sim 10^{3N-6}$ electronic structure calculations if only 10 grid points in each direction are taken.

The "dimensionality bottleneck" can be avoided either by reducing the active degrees of freedom or by approximating the potential surface, as mentioned above.

A third approach is to calculate the ab initio potential "**on the fly**" for each timestep of the nuclear trajectory. This is the so-called *ab initio molecular dynamics* (AIMD).

In the AIMD different methods can be distinguished. The *Born-Oppenheimer dynamics* is characterized by solving the time-independent problem of the electronic system, e.g. with the Schrödinger equation (Eq. (2.6)) or equivalent methods like density functional theory (DFT), for each nuclear geometry at a given time step of the trajectory determined by the Newton equation (2.10). An advantage is that the dynamics is determined by the motion of the nuclei, whereas the electron system is static, so only the classical time step occurs in

the propagation scheme. On the other hand, solving the electronic eigenvalue problem for a multielectron system is computationally very demanding.

A very popular ansatz is the so-called *Car-Parrinello method* [30], in which the electrons are described by DFT using the Kohn-Sham approach [64]. There, the solution of the time-independent Kohn-Sham equations is circumvented with the so-called simulated annealing strategy by introducing the dynamics of a classical field, which has to be solved self-consistently with the Newton equations. The equations are more complex because of additional constraints, but the time step for the classical field and the nuclei are of the same order, allowing for a fast propagation.

A third method is the *Ehrenfest molecular dynamics* or *mean-field approach*³, in which the electrons are described with the time-dependent Schrödinger equation (TDSE)

$$i\frac{\partial}{\partial t}\psi(\mathbf{r}, t) = H_{el}(\mathbf{r}, \mathbf{p}; \mathbf{R})\psi(\mathbf{r}, t). \quad (2.11)$$

The motion of the nuclei is determined by the Newton equation

$$M_A\ddot{\mathbf{R}}_A = -\frac{\partial}{\partial \mathbf{R}_A} \langle \psi | H_{el}(\mathbf{r}, \mathbf{p}; \mathbf{R}) | \psi \rangle \quad (2.12)$$

with the gradient of the expectation value of the electronic Hamiltonian, a term Ehrenfest originally derived by investigating the transition from quantum dynamics to classical dynamics [65]. Whereas the *Born-Oppenheimer dynamics* and the *Car-Parrinello method* is only valid on the electronic ground state surface, the *Ehrenfest molecular dynamics* is in principle also applicable for *nonadiabatic* processes (electronic excitations) due to the time-dependence of the electronic wavefunction $\psi(\mathbf{r}, t)$ which is in general a superposition of all electronic eigenstates

$$\psi(\mathbf{r}, t) = \sum_i c_i(t)\psi_i(\mathbf{r}, \mathbf{R}(t)). \quad (2.13)$$

Electronic state transitions are accessible by the nonadiabatic coupling terms incorporated naturally in the approach. The disadvantage is that due to the different time scales of the fast electronic and the slow nuclear dynamics, the propagation is computationally very demanding.

Our method, the *nonadiabatic quantum molecular dynamics* (NA-QMD), is based on the mean-field approach combined with time-dependent density functional theory in the spirit of a time-dependent version of *Car-Parrinello molecular dynamics*, and will be described in the next section.

Other *nonadiabatic* approaches [66, 67] do not calculate the classical trajectories on the

³The following equations can be derived from the molecular SE (2.4) by using a single-configuration ansatz for the total wave function $\Psi \approx \psi(\mathbf{r}, t)\Omega(\mathbf{R}) A(t)$, where $A(t)$ is a phase factor, and the approximation of classical nuclei.

mean-field electronic surface but stepwise on individual excited states considering different reaction channels. Electronic transitions are done by hopping between the different electronic states taking into account the electron-nuclear correlation. The method was developed by Tully, for nonadiabatic molecular collisions [68] and in general for molecular dynamics [69]. It uses the fewest switch criterion on each time step to decide whether to hop to another electronic state surface or to stay on the current surface. The theory was also generalized to continuum states [70]. A critical point is that it is necessary to know all the excited electronic states (and transition elements) involved. They have to be calculated using quantum chemistry methods like Hartree-Fock, CASSCF or CI. Using density functional methods for hopping is rather difficult due to the severity to calculate excited states. For a two state system, hopping between the ground and first excited state surface, called nonadiabatic Car-Parrinello [71] method, was proposed describing for example the photoisomerization of formaldehyde. There, the first excited state is computed with the restricted Open-Shell Kohn-Sham (ROKS) method [72]. In another approach using the full time-dependent Kohn-Sham equations a hopping between all adiabatic Kohn-Sham-eigenstates was applied to the relaxation processes in protein chromophores [73]. Also a mixture of hopping and mean-field approaches with TD-DFT was proposed [74].

Great efforts have been made to go beyond the approximation of the classical nuclei which suffers by neglecting the nuclear-nuclear correlation, e.g. coherence effects, quantum dispersion broadening or tunneling. The most natural way is to treat the nuclei fully quantum mechanically, propagating the nuclear wave packet on coupled potential surfaces. But wave packet simulations are only possible for small systems with restricted degrees of freedom. A very powerful wavepacket dynamics algorithm, able to treat larger systems than the standard method, is the multiconfiguration time-dependent Hartree approach (MCTDH) [75, 76]. Up to 15 dimensional quantum-dynamical simulation of the protonated water dimer has been performed [77, 78]. In another method, the nuclear Schrödinger equation is not solved, but rather an *ab initio* path-integral technique [79] is used. The path-integral method allows the description of up to 100 nuclear DOF, see for example [80], but deals only with the electronic ground state surface. A method which combines classical trajectory hopping and wave packet dynamics is the so-called *ab initio* multiple spawning method (AIMS) [81] in which the nuclear wave function is approximated by frozen Gaussians. The AIMS method is basically a nonadiabatic extension of the frozen Gaussian wave packet dynamics in semiclassical [82, 83]. A wide range of applications has been investigated, i.e. the photoisomerization of organic molecules (azobenzene) [84], chromophores [85], DNA [86] or proton transfer [87]. Thereby, the electronic surfaces, in most cases only two surfaces, were calculated using quantum chemical methods like the CASSCF-method, or semiempirical methods such as AM1 (see ref. in [88]).

More sophisticated methods have been developed, which are only applicable for one- or two-dimensional systems. For example, a surface hopping of Gaussian phase-space packets

with variable width was implemented solving the adiabatic quantum-classical Liouville equation [89]. It was applied to a two-state model of photodissociation of molecular fluorine [90]. We shortly note, that also a completely different approach, the so-called multicomponent DFT [91], was developed using density functional theory for both types of particles, electrons and nuclei. However, the method suffers from the unknown exchange-correlation functional which is needed in that case also for the nuclear system.

2.2 Adiabatic Quantum Molecular dynamics (QMD)

For adiabatic processes only the knowledge of the electronic ground state surface is necessary. In principle, we have to solve the many-electron SE (2.6), which is for large systems barely not possible or computationally too demanding for standard quantum chemical techniques like configuraton interaction (CI).

Another method is to calculate the Born-Oppenheimer surface by the *time-independent density functional theory* [92] solving the coupled single-particle Kohn-Sham equations [64] for the $j = 1 \dots N_e^\sigma$ electrons with spin $\sigma = \uparrow, \downarrow$:

$$\left(-\frac{\Delta}{2} + V_{eff}[\rho](\mathbf{r}, \mathbf{R}) \right) \phi^{j\sigma}(\mathbf{r}) = \epsilon_{j\sigma} \phi^{j\sigma}(\mathbf{r}). \quad (2.14)$$

The effective potential $V_{eff}[\rho](\mathbf{r}, \mathbf{R})$ depends on the one-particle electronic density

$$\rho(\mathbf{r}) = \sum_{\sigma=\uparrow,\downarrow} \sum_{j=1}^{N_e^\sigma} |\phi^{j\sigma}(\mathbf{r})|^2. \quad (2.15)$$

Note, that from now on \mathbf{r} is only the electronic position vector of a single particle, and not of all electrons as before. The effective potential $V_{eff}[\rho](\mathbf{r}, \mathbf{R})$ depends on the positions $\mathbf{R} = [\mathbf{R}_1, \dots, \mathbf{R}_{N_i}]$ of all N_i nuclei. It includes the generally unknown exchange-correlation potential $V_{xc}[\rho]$, which has to be approximated. The equations of motion for the nuclei are the Newton equations:

$$M_A \ddot{\mathbf{R}}_A = -\frac{\partial E}{\partial \mathbf{R}_A}. \quad (2.16)$$

The potential $E = E[\rho](\mathbf{R})$ depends on the electron density and contains the electron-vibrational coupling term. The QMD approach solves the equations by expanding the Kohn-Sham orbitals in a local basis set of contracted, e.g. LCAO, respectively primitive Gaussians. The quantum molecular dynamics is a limiting case of the more general nonadiabatic quantum molecular dynamics (NA-QMD), so the basis expansion will be explained in more detail in the next section. It has been succesfully applied to collisions mainly with fullerenes (for an overview see in [93]). In particular, atom-cluster collisions have been investigated with classical MD [94–96] using empirical potentials [97,98], molecule-cluster collisions [99,100] with QMD with approximations for the effective potential $V_{eff}[\rho](\mathbf{r}, \mathbf{R})$ and also cluster-cluster collisions [94,101–105].

2.3 Nonadiabatic Quantum Molecular dynamics (NA-QMD)

The *nonadiabatic quantum molecular dynamics* combines classical molecular dynamics with *time-dependent density functional theory in basis expansion* for describing the electrons. Similar methods were developed in which the TD-DFT equations are solved numerically on a *grid in real space* [106–108] or for the special case of cylindrical symmetry [109].

The nonadiabatic Quantum Molecular dynamics was developed to describe cluster collision with electronic excitation processes [29], e.g. metallic cluster collisions: $\text{Na}_9^+ + \text{Na}$, $\text{Na}_9^+ + \text{He}$ [31], $\text{Na}_4 + \text{Cs}$ collisions [35], and charge transfer in collisions of sodium clusters with sodium atoms ($\text{Na}_n^+ + \text{Na}(3s/3p) \rightarrow \text{Na}_n + \text{Na}^+$) [34]. Later, the theory was extended to include explicitly the coupling to external fields [44] and to incorporate absorber potentials to describe ionization efficiently [47]. The NA-QMD formalism is rather general and allows for the investigation of very different nonadiabatic phenomena. So far, it has been applied to the description of atom-cluster collisions [31], high energy ion (H^+ , C^+ , Ar^+) - fullerene collisions [32], the laser induced alignment and fragmentation of H_2 and H_2^+ [48, 49], the fragmentation and isomerization of organic molecules [50, 52] as well as the laser excitation of C_{60} [53].

2.3.1 The mixed classical-quantum equations of motion

General approach

In this section, we present a summary of the NA-QMD theory (for a complete derivation of the equations of motion see ref. [43] and for an extension of the formalism to non-local functionals see ref. [50]). As mentioned, the theory combines a classical description of the nuclear motion with a quantum mechanical treatment of the electronic dynamics using time-dependent density functional theory (TD-DFT) [43] or Hartree-Fock theory [50] in basis expansion. This way, all (nuclear and electronic) degrees of freedom are treated explicitly.

The equations of motion (EOM) are derived from the variational principle for the total action, which consists of a classical and a quantum part describing the nuclear resp. the electronic dynamics. By the variation with respect to nuclear coordinates \mathbf{R}_{A_α} and the many-electron wavefunction $|\Psi\rangle$, the equations of motion for both subsystems will be derived. The following Schrödinger equation for the electronic system will be solved by the equivalent description using the density functional theory. The obtained equations for the N_e^\uparrow spin-up and N_e^\downarrow spin-down electrons ($N_e = N_e^\uparrow + N_e^\downarrow$) are the time-dependent Kohn-

Sham-equations for the (single-particle) Kohn-Sham functions $\Psi^{j\sigma}$ ($j = 1 \dots N_e^\sigma$):

$$i \frac{\partial}{\partial t} \Psi^{j\sigma}(\mathbf{r}, t) = \left(-\frac{1}{2} \frac{\partial^2}{\partial \mathbf{r}^2} + V_{\text{eff}}^\sigma(\mathbf{r}, t) \right) \Psi^{j\sigma}(\mathbf{r}, t) \quad (2.17)$$

with the effective potential

$$V_{\text{eff}}^\sigma(\mathbf{r}, t) = V(\mathbf{r}, \mathbf{R}, t) + \int d^3 r' \frac{\rho(\mathbf{r}', t)}{|\mathbf{r} - \mathbf{r}'|} + V_{\text{xc}}^\sigma(\mathbf{r}, t). \quad (2.18)$$

The external potential

$$V(\mathbf{r}, \mathbf{R}, t) = V_{\text{int}}(\mathbf{r}, \mathbf{R}) + V_{\text{L}}(\mathbf{r}, t) \quad (2.19)$$

includes the interaction potential between an electron and the nuclei

$$V_{\text{int}}(\mathbf{r}, \mathbf{R}) = - \sum_A^{N_i} \frac{Z_A}{|\mathbf{r} - \mathbf{R}|} \quad (2.20)$$

and the electron-laser interaction potential

$$V_{\text{L}}(\mathbf{r}, t) = e \mathbf{r} \cdot \mathbf{E}(t) \quad (2.21)$$

in the dipole approximation with the time-dependent electric field vector $\mathbf{E}(t)$. $V_{\text{xc}}^\sigma(\mathbf{r}, t)$ is the exchange-correlation potential which depends on the electronic spin densities

$$\rho^\sigma(\mathbf{r}, t) = \sum_j^{N^\sigma} |\Psi^{j\sigma}(\mathbf{r}, t)|^2 \quad \sigma = \uparrow, \downarrow. \quad (2.22)$$

The (time-dependent) total electron density is defined as the sum of both spin densities:

$$\rho(\mathbf{r}, t) = \sum_{\sigma=\uparrow, \downarrow} \rho^\sigma(\mathbf{r}, t). \quad (2.23)$$

The equations of motion in basis expansion

The Kohn-Sham functions $|\Psi^{j\sigma}\rangle$ are expanded in a local basis $\{\Phi_\alpha\}$

$$\Psi^{j\sigma}(\mathbf{r}, t) = \sum_\alpha a_\alpha^{j\sigma}(t) \Phi_\alpha(\mathbf{r} - \mathbf{R}_{A_\alpha}(t)) \quad (2.24)$$

centered at the nuclear positions \mathbf{R}_{A_α} . With the help of the expansion coefficients $a_\alpha^{j\sigma}$, the spin-dependent density matrix

$$\gamma_{\beta\alpha}^\sigma(t) = \sum_{j=1}^{N^\sigma} a_\alpha^{j\sigma*}(t) a_\beta^{j\sigma}(t) \quad (2.25)$$

and the total density matrix

$$\gamma_{\beta\alpha} = \gamma_{\beta\alpha}^\uparrow + \gamma_{\beta\alpha}^\downarrow \quad (2.26)$$

in basis representation, can be defined.

Using Eq. (2.17) and (2.24) the equations of the time-dependent expansion coefficients $a_\alpha^{j\sigma}$ follow

$$\boxed{\frac{d}{dt} a_\alpha^{j\sigma} = - \sum_{\beta\gamma} S_{\alpha\beta}^{-1} (iH_{\beta\gamma}^\sigma + B_{\beta\gamma}) a_\gamma^{j\sigma}}. \quad (2.27)$$

Here, the overlap matrix

$$S_{\alpha\beta} = \langle \Phi_\alpha | \Phi_\beta \rangle, \quad (2.28)$$

the Hamilton matrix

$$H_{\alpha\beta}^\sigma = \langle \Phi_\alpha | -\frac{1}{2} \frac{\partial^2}{\partial \mathbf{r}^2} + V_{\text{eff}}^\sigma | \Phi_\beta \rangle, \quad (2.29)$$

and the nonadiabatic coupling matrix

$$B_{\alpha\beta} = \langle \Phi_\alpha | \frac{d}{dt} | \Phi_\beta \rangle \quad (2.30)$$

are introduced with the notation $\Phi_\alpha \equiv \Phi_\alpha(\mathbf{r} - \mathbf{R}_{A_\alpha})$. The brackets denote the integration over the electronic coordinate \mathbf{r} .

The effective potential matrix $V_{\text{eff},\alpha\beta}^\sigma = \langle \Phi_\alpha | V_{\text{eff}}^\sigma | \Phi_\beta \rangle$ can be decomposed into

$$V_{\text{eff},\alpha\beta}^\sigma = \int \Phi_\alpha^*(\mathbf{r} - \mathbf{R}_{A_\alpha}) \left(V(\mathbf{r}, \mathbf{R}, t) + \int \frac{\rho(\mathbf{r}', t)}{|\mathbf{r} - \mathbf{r}'|} d^3r' \right) \Phi_\beta(\mathbf{r} - \mathbf{R}_{A_\beta}) d^3r + \frac{\delta A_{\text{xc}}}{\delta \gamma_{\beta\alpha}^\sigma}. \quad (2.31)$$

The xc-term is the matrix of a local potential

$$\frac{\delta A_{\text{xc}}[\rho^\uparrow, \rho^\downarrow]}{\delta \gamma_{\beta\alpha}^\sigma} = V_{\text{xc}\alpha\beta}^\sigma = \int \Phi_\alpha^*(\mathbf{r} - \mathbf{R}_{A_\alpha}) V_{\text{xc}}^\sigma(\mathbf{r}) \Phi_\beta(\mathbf{r} - \mathbf{R}_{A_\beta}) d^3r \quad (2.32)$$

with

$$V_{\text{xc}}^\sigma(\mathbf{r}) = \frac{\delta A_{\text{xc}}[\rho^\uparrow, \rho^\downarrow]}{\delta \rho^\sigma(\mathbf{r})} \quad (2.33)$$

if the xc-action $A_{\text{xc}} = A_{\text{xc}}[\rho^\uparrow, \rho^\downarrow]$ depends only on the densities ρ^\uparrow and ρ^\downarrow . In all other cases the xc-potential is non-local. In general, the matrix elements of this operator have to be written as

$$V_{\text{xc}\alpha\beta}^\sigma = \int \Phi_\alpha^*(\mathbf{r} - \mathbf{R}_{A_\alpha}) V_{\text{xc}}^\sigma(\mathbf{r}, \mathbf{r}') \Phi_\beta(\mathbf{r} - \mathbf{R}_{A_\beta}) d^3r d^3r' \quad (2.34)$$

with an integral kernel

$$V_{\text{xc}}^\sigma(\mathbf{r}, \mathbf{r}') = \frac{\delta A_{\text{xc}}}{\delta \gamma^\sigma(\mathbf{r}', \mathbf{r})}, \quad (2.35)$$

with the density matrix in position space representation

$$\gamma^\sigma(\mathbf{r}, \mathbf{r}') = \sum_{j=1}^{N^\sigma} \Psi^{j\sigma}(\mathbf{r}, t) \Psi^{j\sigma*}(\mathbf{r}', t) = \sum_{\alpha\beta} \gamma_{\beta\alpha}^\sigma \Phi_\alpha^*(\mathbf{r}' - \mathbf{R}_{A_\alpha}) \Phi_\beta(\mathbf{r} - \mathbf{R}_{A_\beta}). \quad (2.36)$$

For the special case of the Hartree-Fock method, the kernel is given by

$$V_{\text{xc}}^{\text{HF}\sigma}(\mathbf{r}, \mathbf{r}') = -\frac{\gamma^\sigma(\mathbf{r}, \mathbf{r}')}{|\mathbf{r} - \mathbf{r}'|}. \quad (2.37)$$

The dynamics of the nuclei is determined by the classical EOM

$$\boxed{M_A \ddot{\mathbf{R}}_A = -\frac{\partial U}{\partial \mathbf{R}_A} + \sum_{\sigma, j} \sum_{\alpha\beta} a_\alpha^{j\sigma*} \left(-\frac{\partial H_{\alpha\beta}^\sigma}{\partial \mathbf{R}_A} + \mathbf{D}_{\alpha\beta}^{A\sigma} \right) a_\beta^{j\sigma}}, \quad (2.38)$$

with the classical potential

$$U(\mathbf{R}, t) = \sum_{A < B}^{N_i} \frac{Z_A Z_B}{|\mathbf{R}_A - \mathbf{R}_B|} + \sum_A^{N_i} Z_A \mathbf{R}_A \mathbf{E}(t) \quad (2.39)$$

as the sum of the nucleus-nucleus repulsion potential and the nucleus-laser interaction potential, and the electron-nuclear interaction described by $\frac{\partial H_{\alpha\beta}^\sigma}{\partial \mathbf{R}_A}$. The velocity-dependent matrix

$$\begin{aligned} \mathbf{D}_{\alpha\beta}^{A\sigma} = & \sum_{\gamma\delta} (\mathbf{B}_{\alpha\gamma}^{A+} S_{\gamma\delta}^{-1} H_{\delta\beta}^\sigma + H_{\alpha\gamma}^\sigma S_{\gamma\delta}^{-1} \mathbf{B}_{\delta\beta}^A) \\ & + i \left[\mathbf{C}_{\alpha\beta}^{A+} - \mathbf{C}_{\alpha\beta}^A + \sum_{\gamma\delta} (B_{\alpha\gamma}^+ S_{\gamma\delta}^{-1} \mathbf{B}_{\delta\beta}^A - \mathbf{B}_{\alpha\gamma}^{A+} S_{\gamma\delta}^{-1} B_{\delta\beta}) \right] \end{aligned} \quad (2.40)$$

with

$$\mathbf{B}_{\alpha\beta}^A = \langle \Phi_\alpha | \frac{\partial}{\partial \mathbf{R}_A} \Phi_\beta \rangle, \text{ and } \mathbf{C}_{\alpha\beta}^A = \langle \frac{d}{dt} \Phi_\alpha | \frac{\partial}{\partial \mathbf{R}_A} \Phi_\beta \rangle \quad (2.41)$$

appears due to the finiteness of the basis, and vanishes for a complete or nonlocal basis set [43]. The term is related to the so-called pulay forces (see for example in ref. [61]).

Due to the basis expansion a basis error occurs caused by the limited Hilbert space for the Kohn-Sham orbitals. It is a big problem to find an appropriate basis set for a given molecular system. But, it has been shown that the basis error can be estimated in time-dependent calculations. [46]. Unfortunately, the computation of the basis error is very demanding and has been done only for a one-electron system (hydrogen atom) [46].

2.3.2 NA-QMD and ionization

In principle, the NA-QMD approach also includes ionization if the basis set is large enough resp. is complete in Hilbert space. However, for numerical reasons (to avoid unphysical reflexions) it is necessary to define an absorber for the electronic motion, which should be suited to the basis set approach. A natural way in a basis set approach is to define the absorber in the energy domain, which is rather unusual in grid based methods, where

absorber potentials in real space are in use. To do so, basis sets describing continuum states are necessary. Therefore, we use larger basis sets, which are not only centered at the nuclear positions but rather fill out a larger region in space. This will be done by employing a grid fixed in space with Gaussians centered at the grid points, also allowing electronic motion far away from the nuclei, e.g. the quiver motion in an electric field.

Definition of the absorber potential

The absorber potential $\hat{V}_{\text{abs}}^\sigma$ is defined as a weighted sum of all eigenstate-projectors, e.g.

$$\hat{V}_{\text{abs}}^\sigma = \sum_a f_a^\sigma |\chi_a^\sigma\rangle \langle \chi_a^\sigma| \quad (2.42)$$

with the time-dependent adiabatic eigenfunctions $|\chi_a^\sigma\rangle$ evaluated by

$$\langle \chi_a^\sigma | \hat{H}_{\text{eff}}^\sigma(t) | \chi_b^\sigma \rangle = \epsilon_a^\sigma(t) \delta_{ab} \quad (2.43)$$

The factors for decay $f_a^\sigma = \frac{1}{2\tau_a^\sigma}$ are determined by the life time τ_a^σ of the states $|\chi_a^\sigma\rangle$:

$$\tau_a^\sigma = \begin{cases} \infty & \epsilon_a^\sigma \leq 0 \text{ a.u.} \\ \frac{\tau_{\text{min}}}{\sin^2\left(\frac{\epsilon_a^\sigma \pi}{2E_{\text{ref}}}\right)} & 0 < \epsilon_a^\sigma < E_{\text{ref}}, \\ \tau_{\text{min}} & \epsilon_a^\sigma \geq E_{\text{ref}} \end{cases}, \quad (2.44)$$

and depend on the adiabatic eigenenergies ϵ_a^σ . The definition guarantees that only states with positive eigenenergies ϵ_a^σ will be depopulated, whereas the electron density of bound states is not affected. The absorber parameters are fixed to be $E_{\text{ref}} = 0.3$ a.u. and $\tau_{\text{min}} = 4.76$ a.u. guaranteeing a smooth absorption of states with positive energies (see for details ref. [48]).

Equations of motion with absorber

To ensure a decreasing norm, i.e. ionization, the Kohn-Sham equations (2.27) are modified by the additional imaginary absorber potential ($H \rightarrow H - iV_{\text{abs}}$). Therefore, the full Hamiltonian is no longer hermitian, and the norm is no longer a conserved quantity. The equations of the expansion coefficients $a_\alpha^{j\sigma}$ follow

$$\frac{d}{dt} a_\alpha^{j\sigma} = - \sum_{\beta\gamma} S_{\alpha\beta}^{-1} (iH_{\beta\gamma}^\sigma + B_{\beta\gamma} + V_{\text{abs},\beta\gamma}^\sigma) a_\gamma^{j\sigma} \quad (2.45)$$

with the additional matrix element describing the (semi-positive definite) absorber

$$V_{\text{abs},\beta\gamma}^\sigma := \langle \Phi_\alpha | \hat{V}_{\text{abs}}^\sigma | \Phi_\beta \rangle. \quad (2.46)$$

Expanding the Kohn-Sham orbitals

$$|\psi^{j\sigma}\rangle = \sum_a a_a^{j\sigma} |\chi_a^\sigma\rangle \quad (2.47)$$

in the basis of the adiabatic eigenstates $|\chi_a^\sigma\rangle$ (see Eq. (2.43)), we find that the norm $N^{j\sigma} = \langle \psi^{j\sigma} | \psi^{j\sigma} \rangle$ decreases in time, if states $|\chi_a^\sigma\rangle$ with positive energies $\epsilon_a^\sigma > 0$ were populated:

$$\frac{d}{dt} N^{j\sigma} = -2 \sum_a V_{\text{abs},aa}^\sigma |a_a^{j\sigma}|^2 = -2 \sum_a f_a^\sigma |a_a^{j\sigma}|^2. \quad (2.48)$$

The nuclear equations of motion will not be changed explicitly, so the nuclei move according to equation 2.38 ⁴.

Definition of ionization probabilities

Within density functional theory, all observables are functionals of the electron density. However, in most cases the functionals are unknown and have to be approximated. The best example is the energy functional $E[\rho](t)$ where the exchange-correlation energy is generally unknown. This is also the case for the single or multiple ionization probabilities. As a first approximation, the Slater-determinant of the fictitious Kohn-Sham system is taken seriously, meaning as the real physical many-body wave function. Then, the single ionization probability $P^1(t)$ can be computed according to the single-particle picture of non-interacting particles:

$$P^1[\rho](t) \approx \sum_{i=1}^{N_e} N^1(t) \dots N^{i-1}(t) \overline{N^i}(t) N^{i+1}(t) \dots N^{N_e}(t) \quad (2.49)$$

with the occupation probability $N^i(t)$ and the ionization probability $\overline{N^i}(t) = 1 - N^i(t)$ of the i th Kohn-Sham orbital. Note, that in the definition (2.49) the index i is a superindex including the spin ($i = (1, \uparrow) \dots (N_e^\uparrow, \uparrow) (1, \downarrow) \dots (N_e^\downarrow, \downarrow)$). Very similar, the double ionization $P^2(t)$ is defined by the sum over all combinations with two ionized Kohn-Sham orbitals (i, j)

$$P^2[\rho](t) \approx \sum_{i < j}^{N_e} N^1(t) \dots N^{i-1}(t) \overline{N^i}(t) N^{i+1}(t) \dots N^{j-1}(t) \overline{N^j}(t) N^{j+1}(t) \dots N^{N_e}(t) \quad (2.50)$$

with i and j being composed indices as mentioned above. The definition for higher multiple ionization probabilities can be defined in the same manner.

⁴Note, that in a sense the coupled system of Kohn-Sham equations (2.45) and Newton-equations (2.38) is not self-consistent anymore as a consequence of including the absorber only in (2.45). But modifying also the Newton-equations allow for the creation of (unphysical) complex trajectories, which we would have to deal with.

2.3.3 Definition of physical properties in the NA-QMD approach

In the following some quantities which will be used throughout this work will be defined in the context of the NA-QMD approach. Note, that the following properties are only defined properly if no absorber potential is used.

The total energy $E(t)$

The total energy of the molecular system E

$$E(\gamma, \mathbf{R}, \dot{\mathbf{R}}, t) = U(\mathbf{R}, t) + E_{\text{kin}}^{\text{nuc}}(\dot{\mathbf{R}}, t) + E_{\text{kin}}^{\text{el}}(\gamma, \mathbf{R}, t) + E_{\text{int}}(\gamma, \mathbf{R}, t) + E_{\text{Q}}(\gamma, \mathbf{R}, t) + E_{\text{xc}}(\gamma, \mathbf{R}, t) \quad (2.51)$$

contains the potential energy of the nuclei $U(\mathbf{R}, t)$ in the laser field (Eq. (2.39)), the kinetic energy of the nuclei

$$E_{\text{kin}}^{\text{nuc}} = \sum_{A=1}^{N_i} \frac{M_A}{2} \dot{\mathbf{R}}_A^2, \quad (2.52)$$

the kinetic energy of the electrons

$$E_{\text{kin}}^{\text{el}} = \sum_{\sigma, j} \langle \Psi^{j\sigma} | -\frac{1}{2} \frac{\partial^2}{\partial \mathbf{r}^2} | \Psi^{j\sigma} \rangle = \sum_{\alpha\beta}^{N_b} \gamma_{\beta\alpha} T_{\alpha\beta}, \quad (2.53)$$

the nuclei-electron and laser-electron interaction energy (see Eq. (2.19))

$$E_{\text{int}} = \int d^3r \rho(\mathbf{r}, t) V(\mathbf{r}, \mathbf{R}, t) = \sum_{\alpha\beta}^{N_b} \gamma_{\beta\alpha} V_{\alpha\beta} \quad (2.54)$$

with

$$V_{\alpha\beta} = \langle \Phi_{\alpha} | V(\mathbf{r}, \mathbf{R}, t) | \Phi_{\beta} \rangle, \quad (2.55)$$

the Coulomb energy

$$E_{\text{Q}} = \frac{1}{2} \int \frac{\rho(\mathbf{r})\rho(\mathbf{r}')}{|\mathbf{r} - \mathbf{r}'|} d^3r d^3r' = \frac{1}{2} \sum_{\alpha\beta\gamma\delta}^{N_b} Q_{\alpha\beta\gamma\delta} \gamma_{\beta\alpha} \gamma_{\delta\gamma} \quad (2.56)$$

with

$$Q_{\alpha\beta\gamma\delta} = \int \frac{\phi_{\alpha}^*(\mathbf{r})\phi_{\beta}(\mathbf{r})\phi_{\gamma}^*(\mathbf{r}')\phi_{\delta}(\mathbf{r}')}{|\mathbf{r} - \mathbf{r}'|} d^3r d^3r' \quad (2.57)$$

and the exchange and correlation energy E_{xc} .

The energy balance can be derived from the definition (2.51) using the equations of motion (2.27), (2.38). The expected result is that the total energy is only changed by time-dependent external (laser) fields:

$$\frac{d}{dt} E = \int \rho(\mathbf{r}, t) \frac{\partial V_{\text{L}}(\mathbf{r}, t)}{\partial t} d^3r - \sum_{A=1}^{N_i} Z_A \frac{\partial V_{\text{L}}(\mathbf{R}_A, t)}{\partial t}. \quad (2.58)$$

The absorbed energy $E_{\text{abs}}(\mathbf{t})$

The absorbed energy or total excitation energy E_{abs} is given by the difference of the current energy $E(t)$ at time t and the initial energy $E(t=0)$ which is in most cases the (electronic) ground state energy E_{gs} of the initial geometrical conformation $\mathbf{R}(t=0)$:

$$E_{\text{abs}}(t) = E(t) - E(t=0). \quad (2.59)$$

The electronic excitation energy $E_{\text{exc}}(\mathbf{t})$

As seen before, the system can be excited by external fields. Depending on the parameters of the external field, either the nuclear (second term on the right hand side of Eq. (2.58)) or the electronic system (first term on the right hand side of Eq. (2.58)) will be excited dominantly. A measurement of the electronic excitation is the electronic excitation energy. It is defined as

$$E_{\text{exc}}(t) = E_e^{td}(t) - E_e^{gs}(\mathbf{R}(t)), \quad (2.60)$$

where

$$\begin{aligned} E_e^{td}(t) = & \sum_{\sigma=\uparrow,\downarrow} \sum_{j=1}^{N_e^\sigma} \langle \Psi^{j\sigma}(t) | -\frac{1}{2} \frac{\partial^2}{\partial \mathbf{r}^2} | \Psi^{j\sigma}(t) \rangle + \int d^3r \rho(\mathbf{r}, t) [V(\mathbf{r}, \mathbf{R}, t) \\ & + \frac{1}{2} \int d^3r' \frac{\rho(\mathbf{r}', t)}{|\mathbf{r} - \mathbf{r}'|}] + E_{\text{xc}}[\rho](\mathbf{r}, t) \end{aligned} \quad (2.61)$$

is the time-dependent electronic energy and $E_e^{gs}(\mathbf{R}(t))$ denotes the ground state energy of the electrons for the current nuclear configuration $\mathbf{R}(t)$

$$\begin{aligned} E_e^{gs}(\mathbf{R}(t)) = & \sum_{\sigma=\uparrow,\downarrow} \sum_{j=1}^{N_e^\sigma} \langle \phi^{j\sigma} | -\frac{1}{2} \frac{\partial^2}{\partial \mathbf{r}^2} | \phi^{j\sigma}(t) \rangle + \int d^3r \rho(\mathbf{r}) [V(\mathbf{r}, \mathbf{R}) \\ & + \frac{1}{2} \int d^3r' \frac{\rho(\mathbf{r}')}{|\mathbf{r} - \mathbf{r}'|}] + E_{\text{xc}}[\rho](\mathbf{r}) \end{aligned} \quad (2.62)$$

using the time-independent Kohn-Sham orbitals $|\phi^{j\sigma}\rangle_{|\mathbf{R}(t)}$ resp. the density $\rho(\mathbf{r})_{|\mathbf{R}(t)}$ of Eq. (2.14).

The electronic system can also be excited through the energy transfer from the nuclear degrees of freedom to the electrons, e.g. in high energy collisions.

The number of excited electrons $N_{\text{exc}}(\mathbf{t})$

Besides the energy properties defined above also the number of excited electrons $N_{\text{exc}}(t)$ is of interest making it possible to distinguish between single electron and multi electron dynamics. The number of excited electrons in DFT is defined as

$$N_{\text{exc}}(t) = N_{\text{exc}}^\uparrow(t) + N_{\text{exc}}^\downarrow(t) \quad (2.63)$$

with the spin components

$$N_{exc}^{\sigma}(t) = N_e^{\sigma} - \sum_{a=1}^{N_e^{\sigma}} n_a^{\sigma}(t). \quad (2.64)$$

Thereby, the occupation numbers n_a^{σ} are calculated by projecting the Kohn-Sham orbitals $|\Psi^{j\sigma}(t)\rangle$ on the ground state Kohn-Sham orbitals $|\phi^{a\sigma}\rangle_{\mathbf{R}(t)}$. A more detailed derivation and the formula in basis expansion is given in Appendix A.1.

2.3.4 Numerics

Gaussian basis set

In the NA-QMD approach the basis for the Kohn-Sham functions consists of primitive and/or contracted Gaussian functions centered at the nuclear positions or at fixed positions in space. A (normalized) primitive Gaussian function is given by

$$\Phi_{\alpha}(\mathbf{r} - \mathbf{R}_{A_{\alpha}}) = g_0(\sigma_{\alpha}, \mathbf{r} - \mathbf{R}_{A_{\alpha}}) J_i(\sigma_{\alpha}, \mathbf{r} - \mathbf{R}_{A_{\alpha}}) \quad (2.65)$$

with the s-type Gaussian ($l = 0$)

$$g_0(\sigma, \mathbf{r}) = \left(\frac{2}{\pi\sigma^2} \right)^{\frac{3}{4}} e^{-\frac{\mathbf{r}^2}{\sigma^2}} \quad (2.66)$$

The angular functions J_i for the angular momentum $l = i$ are a polynomial of order i in the cartesian coordinates x, y, z [44]. A general primitive Gaussian function can also be expressed by a differential operator D_i applied to a s-type Gaussian:

$$\Phi_{\alpha}(\mathbf{r} - \mathbf{R}_{A_{\alpha}}) = D_i(\sigma_{\alpha}, \mathbf{r}) g_0(\sigma_{\alpha}, \mathbf{r} - \mathbf{R}_{A_{\alpha}}), \quad (2.67)$$

which is helpful for the calculation of matrix elements. The simple Gaussians are normalized

$$\langle \Phi_{\alpha} | \Phi_{\alpha} \rangle = 1 \quad (2.68)$$

and Gaussians of different angular momentum are orthogonal to each other.

Contracted Gaussians are a linear combination of simple Gaussians. They are suited to mimic atomic orbitals and are commonly used in quantum chemistry basis sets.

The density is also expanded in an auxiliary basis

$$\rho^{\sigma}(\mathbf{r}, t) = \sum_{\alpha=1}^{N_{\rho}} \Phi_{\alpha}^{\rho}(\mathbf{r} - \mathbf{R}_{A_{\alpha}}), \quad (2.69)$$

which has to be chosen separately. The definition of the Gaussians Φ_{α}^{ρ} differs from the Φ_{α} only by a constant factor due to the other normalization procedure.

Matrix elements

A main advantage of a Gaussian basis set is that the calculation of many matrix elements occurring in the Kohn-Sham equations (2.27) and in the Newton equations (2.38) can be performed analytically. Four different types of matrix elements occur:

- one-center matrix elements depending only on one nuclear position
- two-center matrix elements depending on two nuclear positions
- three-center matrix elements depending on three nuclear positions
- four-center matrix elements depending on four nuclear positions

which require increasing numerical effort.

All the one and two-center matrix elements can be calculated analytically, e.g. $S_{\alpha\beta}$, $T_{\alpha\beta}$ or $B_{\alpha\beta}$. Fortunately, it is possible to calculate all higher matrix elements from two-center matrix elements using the auxiliary basis expansion of the density ρ and some approximations (Coulomb-interaction). The two-center matrix elements can be stored as a function of distance which reduces the numerical effort considerably. The angular dependence in the two-center matrix elements can be separated by a rotational transformation.

Due to the complicated nonlinear dependence on the density ρ only the matrix elements containing the xc-potential will be calculated numerically on a grid.

The L(S)DA functional

In the local spin density approximation (LSDA) the electronic system will be treated as homogeneous electron gas. The exchange-correlation energy is given by

$$E^{LSDA}[\rho^\uparrow, \rho^\downarrow] = E_x^{LSDA}[\rho^\uparrow, \rho^\downarrow] + E_c^{LSDA}[\rho^\uparrow, \rho^\downarrow]. \quad (2.70)$$

The exchange energy E_x^{LSDA} of the homogeneous electron gas is known analytically as

$$E_x^{LSDA} = -\frac{3}{2} \left(\frac{3}{4\pi} \right)^{\frac{1}{3}} \sum_{\sigma} \int \rho^{\sigma}(\mathbf{r})^{\frac{4}{3}} d^3r. \quad (2.71)$$

The correlation energy E_c^{LSDA} can be written in the same way as

$$E_c^{LSDA} = \int \rho(\mathbf{r}) \epsilon_c(\mathbf{r}) d^3r \quad (2.72)$$

No exact analytical expression for the correlation energy per particle $\epsilon_c(\mathbf{r})$ is known and so it has to be calculated numerically. In the implementation of DYMOL [110] the parametrization by Perdew and Wang will be used [111].

The LDA functional for closed shell systems (singlet states) with the same number of spin-up and spin-down electrons ($\rho_{\uparrow} = \rho_{\downarrow} = \frac{\rho}{2}$) is given by

$$E^{LDA}[\rho] = E^{LSDA}\left[\frac{\rho}{2}, \frac{\rho}{2}\right]. \quad (2.73)$$

The LSDA functional has to be determined on a real space grid since no formalism for the calculation in basis expansion exists in contrast to the LDA functional (cf. also [44]). Furthermore, it is even for the LDA better to use the LDA integration on a grid because this grid based determination of the functionals is numerically more stable. Two different kinds of grids will be used, (i) atomic grids that can be located at each nucleus and (ii) a simple cubic grid that extends the atomic grids.

The atomic grid points are arranged in shells around the nucleus. The distance of the i th shell from the center is given by

$$r_i = -\alpha_{\text{grid}} \log \left(1 - \left(\frac{i}{N_{\text{grid}}} \right)^{\beta_{\text{grid}}} \right). \quad (2.74)$$

The parameters that have to be specified in actual calculations are the stretching factor α_{grid} , the number of shells N_{grid} and the exponent β_{grid} . The standard values used in the DYMOL implementation [110] are $\alpha_{\text{grid}} = 3$, $N_{\text{grid}} = 30$ and $\beta_{\text{grid}} = 3$.

For each shell an angular grid is laid out. This angular grid is determined by the maximal l of spherical harmonics for which the angular integration on this grid is exact (see [44] and references therein for details). This l is determined from the radial density of points $r_i/\Delta r_i$ with

$$\Delta r_i = \frac{\beta_{\text{grid}} \alpha_{\text{grid}} \left(\frac{i}{N_{\text{grid}}} \right)^{\beta_{\text{grid}}-1}}{N \left(1 - \left(\frac{i}{N_{\text{grid}}} \right)^{\beta_{\text{grid}}} \right)}. \quad (2.75)$$

The maximal $l_{i,\text{grid}}$ of the i th shell is then

$$l_{i,\text{grid}} = \begin{cases} \left[\frac{r_i}{\Delta r_i} \gamma_{\text{grid}} \sqrt{8\pi} \right] - 1 & \text{if result} \leq l_{\text{grid}}^{\text{max}} \\ l_{\text{grid}}^{\text{max}} & \text{otherwise} \end{cases}. \quad (2.76)$$

Two further parameters occur, γ_{grid} the ratio of angular and radial point density and $l_{\text{grid}}^{\text{max}}$ the maximal possible $l_{i,\text{grid}}$. The standard parameters in DYMOL are $\gamma_{\text{grid}} = 0.8$ and $l_{i,\text{grid}}^{\text{max}} = 50$. Additional basis functions centered on a grid in space have to be taken into account to describe ionization. Therefore, an additional numerical simple cubic (sc) grid for the L(S)DA integration will be used. The sc grid is in all three dimensions (i=x,y,z) symmetric to the origin and each direction is determined by the number of points in that direction N_i and the spacing between points Δ_i . The total sc grid size is then given by $N_x N_y N_z$. The parameters of the sc grid have to match the basis function grid in a way that the spacing between the basis function centers is a multiple of Δ_i . Thus the sc grid ensures a good description of the density far away from the nuclei, whereas atomic grids must still be placed on the nuclei describing the density close to the nuclei.

Calculation scheme

Preparation of the initial state

Before the propagation starts the initial state has to be determined. This is done by calculating the electronic ground state for the given geometrical configuration solving the time-independent Kohn-Sham equations (Eq. (2.14)) in basis expansion

$$\sum_{\beta} (H_{\alpha\beta}^{\sigma} - \epsilon_{j\sigma} S_{\alpha\beta}) a_{\beta}^{j\sigma} = 0. \quad (2.77)$$

The secular equation (2.77) has to be solved for the unknown coefficients $a_{\beta}^{j\sigma}$ and Kohn-Sham energies $\epsilon_{j\sigma}$ iteratively since the Hamilton-matrix $H_{\beta\gamma}^{\sigma}$ depends itself on the electronic density, i. e. on $a_{\beta}^{j\sigma}$. In order to do so a relaxed constrained algorithm is being used [112]. The geometrical groundstate configuration, i.e. the nuclear equilibrium configuration, will be found by minimizing the total groundstate energy. The optimization of the geometrical groundstate configuration is done by using a Polak-Ribiere variant of the conjugated gradient method [113].

Electronic and nuclear propagation

In the dynamical calculations two different time domains occur due to the fast electronic motion and the (in most cases) slow nuclear motion. In most cases the electronic motion is much faster than the nuclear motion due to the different mass. Therefore, the electronic system is propagated with a much smaller time step (~ 0.1 a.u.) than for the propagation of the nuclei (factor 10 of the electronic time step and more). The electronic time step is set automatically by an adaptive multistep method [114] which solves the coupled system of ordinary differential equations (2.27) resp. (2.45).

The classical time step taken to solve the Newton equations (2.38) is adapted to the particular problem and covers the range from 0.1 a.u. for high-energy collisions to 50 a.u. for low-energy collisions without electronic excitation. The Newton equations (2.38) are solved by using the Verlet-algorithm taking two previous nuclear positions into account.

3 Laser-induced dynamics

In this chapter we will show three different nonadiabatic molecular processes in different many-electron systems calculated with the NA-QMD formalism.

The first application is the investigation of the ionization of the dimers N_2 and O_2 which depends strongly on the electronic structure as well as on the orientation between laser field and molecule. In most cases, single electron methods using perturbation theory will be used to calculate ionization probabilities neglecting the many-electron interaction. Here, we will show full ab-initio calculations for the ionization of unaligned molecules taking into account all valence electrons. We will find, that the shape of the outermost molecular orbital defines mainly the orientation dependence of the ionization but also other lower lying electronic states contribute to the ionization. In particular, the ionization of N_2 has a maximum for aligned molecules whereas the ionization of O_2 is peaked at an angle of 40° . This is caused by the different shape of the highest occupied orbitals (HOMO). Describing the ionization is numerically a tough task. Therefore, molecular motion will not be considered in this case. In the second example the molecular dynamics of the diimide molecule N_2H_2 , a prototype for an organic molecule, excited by a fs laser pulse will be shown. The dynamics depends strongly on the electronic excitation which can be tuned by varying the laser frequency. Besides different fragmentation reactions, a very important reaction in photophysics, the laser-induced isomerization, will be investigated.

In the last part, the laser-induced dynamics of a much larger system, the fullerene C_{60} with 174 nuclear degrees of freedom, is presented. We will show, that for high electronic excitation energies the vibrational motion is dominated only by a single vibrational mode – the breathing mode.

3.1 Ionization of diatomics

Since the basic process for describing multiple ionization or high harmonic generation is the single ionization, the ionization itself is of particular interest. In the most simplified picture the single ionization rate depends only on one intrinsic parameter, the ionization energy I_P . So there should be no differences between ionization in atoms and molecules with the same ionization energy, but it has been shown that molecular effects are important. One effect is the suppression of ionization compared to companion atoms with the same ionization energy, e.g. N_2 and Ar.

Experimental works were done for the dimers N_2 and O_2 [115, 116] resp. F_2 and S_2 [115] but also for CO_2 [116]. Since it is very difficult to compute the ionization in multielectron

systems exactly, most groups are using approximated theories. Two approximated single electron theories were developed to describe the ionization in the tunneling or the multi-photon regime taking into account only the outermost electronic orbital. The first is the ADK theory, which is a quasistatic tunneling model. This theory describes how the electron tunnels through a barrier which is given by the sum of the internal potential and the external field potential at a given time. The original theory for atomic systems was extended to molecules [117] where the shape of the outermost orbital plays the important role.

In the other approach perturbation theory is used. It was developed by Keldysh/Faisal/Reiss (KFR theory) [118–121] and later extended to the so-called Intense-field Many-body S-Matrix Theory (IMST) [122, 123] respectively to the equivalent Molecular Orbital Strong-Field Approximation (MO-SFA) [124]. Thereby, the S-matrix will be calculated using a final product state of the ionic ground state and the (free electron) Volkov-state. In this approach the symmetry of the orbital is very important, in that an interference term reduces the ionization for antibonding orbitals. The interference term occurs in the limit $k_N R \ll 1$ (kinetic energy of the ionized electron for a N-photon process: $\frac{k_N^2}{2}$, R: bond length), i.e. smaller wavelengths λ . An example is suppression of the O₂ single ionization compared with Xe for 800 nm [125] but not for 1064 nm [126].

Both approaches describe the ionization behavior of N₂ and O₂ correctly, but fail in the case of F₂. An explanation was given by Dundas et.al. [127] using a grid-based TD-DFT approach adapted to the cylindrical symmetry suited to the special case of molecules aligned with the laser field. They showed for aligned F₂ molecules, that not only the (antibonding) highest occupied orbital but also other orbitals (with other symmetry) are needed for the description of the ionization. A similar TD-DFT approach was developed by Chu [128, 129] investigating also the ionization of aligned dimers with a self-interaction corrected xc-functional ansatz, showing the importance of multielectron effects especially for large laser intensities. Due to the molecular structure, a second effect, not known from atoms, occurs – the orientation dependence of the ionization. The effect can be measured nowadays due to the recent possibilities to prepare aligned molecules (see refs. in [130–132]). So for example, the angle dependent ionization rate of N₂ and O₂ has been measured in experiments of Cocke [131, 132] with a Ti:Sapphire laser (800nm). This effect has been only investigated theoretically by the approximated single active electron methods (ADK [117] resp. MO-SFA [124]), reproducing the main effect caused by the electron in the outermost orbital. However, it is desirable to check if the orientation dependence is influenced by many-electron effects. In this case, the TD-DFT methods in refs. [127, 128] are not applicable due to the broken cylindrical symmetry. However, the big advantage of the NA-QMD approach is that no symmetry restrictions exist due to the basis expansion ansatz with Gaussians. So far, the method has been mainly used to describe molecular alignment and fragmentation for the most simplest diatomics H₂⁺ resp. H₂ [45, 48, 49].

Here, we will investigate the angular dependent ionization of the "real" many-electron dimers

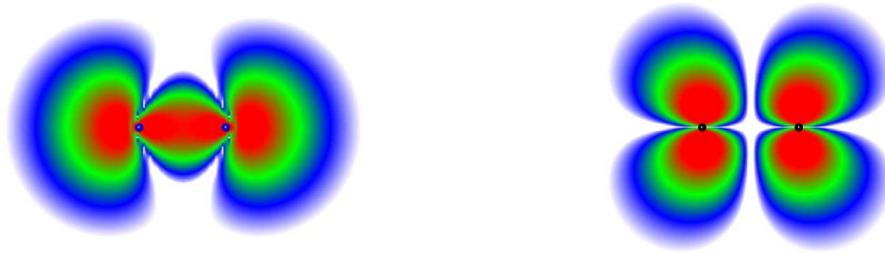


Figure 3.1: The highest occupied orbital (HOMO) for the molecules nitrogen ($3\sigma_g$ orbital) and oxygen ($1\pi_g$ orbital). The density $|\psi_{\text{HOMO}}|^2$ of the orbitals is shown in the molecular yz -plane (maximal value in red). The dimers are located horizontally (z -direction), and the nuclei are indicated by small spheres.

N_2 and O_2 caused by few-cycle laser pulses ($T = 8$ fs) with different laser frequencies. The laser is defined by

$$\mathbf{E}(t) = \begin{cases} \mathbf{E}_0 \sin^2 \frac{\pi t}{2T} \cos \omega t & \text{for } 0 \leq t \leq 2T \\ \mathbf{0} & \text{else} \end{cases} \quad (3.1)$$

where $\mathbf{E}_0 = E_0 \mathbf{e}_z$ denotes the amplitude of the linearly polarized electric field (in z -direction), $2T$ the total pulse duration and ω the central frequency of the laser. In a first approximation no nuclear motion is considered restricting us to fixed dimers at the equilibrium bond length, which is computationally much more feasible. However, the difference should be small for cold molecules in the vibrational ground state, whereas for higher excited vibrational states deviations may occur.

3.1.1 The ground state properties of N_2 and O_2

For the xc-potential we use the LSDA-functional which gives satisfying results for the ground state properties of the dimers. It is not sufficient to apply the restricted Kohn-Sham theory, i.e. treating spin-up and spin-down electrons in the same way. In particular, it is not possible for the O_2 -molecule, which has a triplet ground state with 9 spin-up and 7 spin-down electrons. The N_2 molecule has a singlet ground state with 7 spin-up and 7 spin-down electrons, but it will also be treated with the more general unrestricted Kohn-Sham approach to allow comparability on the same level as the O_2 calculations. The 1s-core electrons of the nitrogen and oxygen atoms are treated in the frozen core approximation, and do not contribute to the electron dynamics. Thereby, the 1s orbitals were obtained by atomic ground state calculations for the two species. 5 spin-up and spin-down valence electrons for N_2 , and

7 spin-up resp. 5 spin-down valence electrons for O_2 remain in the molecular framework and have to be treated explicitly with the help of the Kohn-Sham equations.

For the valence electrons the parameters of the Gaussian basis, located at each of the nitrogen respectively oxygen atoms, are given in Table 3.1 resp. 3.2. Also the parameters of an auxiliary basis set for the expansion of the density are displayed.

Additional basis functions are used which are located in the plane characterized by the molecular and the laser polarization axis. A sketch of the positions of the additional Gaussians in the y - z plane is shown in Fig. 3.2. These s -type Gaussians located at hexagonal grid points are constructed according to the parameters in Table 3.3. The hexagonal grid in the y - z plane is defined with the grid parameters d , N_1 and N_2 as

$$\begin{pmatrix} x_{ij} \\ y_{ij} \\ z_{ij} \end{pmatrix} = \begin{pmatrix} 0 \\ (i - \frac{N_1-1}{2}) \frac{d}{2} \\ (j - \frac{N_2}{2}) \sqrt{3}d + |(i - \frac{N_1-1}{2}) \bmod 2| \frac{\sqrt{3}}{2}d \end{pmatrix} \quad (3.2)$$

with

$$\begin{aligned} 0 \leq i < N_1 & \quad \text{and} \\ 0 \leq j < N_2 - 1 & \quad \text{if } N_1 + i \text{ even} \quad \text{or} \\ 0 \leq j < N_2 & \quad \text{if } N_1 + i \text{ odd.} \end{aligned}$$

In total, we use 106 resp. 144 basis functions located at the nitrogen resp. oxygen nuclei plus 70 or more additional basis functions. The choice of the grid parameters is a nontrivial problem. There exists an estimation of the basis error in the NA-QMD formalism but due to the computational costs, calculations are only possible for the hydrogen atom [46]. So the parameters of the additional basis functions were obtained by minimizing the basis error of hydrogen calculations using the laser parameters of the calculations for the diatomics. Furthermore, two density basis functions with $\sigma_{\rho i} = \frac{\sigma_{\rho}}{2^i}$ and $i = 0, 1$ are pinned to each of the additional centers (see Table 3.3). The Gaussian width σ_{ρ} for the density is calculated as $\sigma_{\rho} = \frac{\sigma}{\sqrt{2}}$ with the width σ taken from Table 3.3.¹ Also an additional cubic grid adapted to the hexagonal grid for the LSDA integration was used.

In Figure 3.3 the potential energy surface of the ground state of both dimers is depicted. The equilibrium distance R_0 for N_2/O_2 is obtained with 2.06/2.304 a.u. which is near the experimental values of 2.072/2.279 a.u. [133].

To give us a clue to the physical mechanism in the ionization process, we examined the Kohn-Sham orbitals. Though the Kohn-Sham orbitals are calculated for the fictitious Kohn-Sham system, the molecular orbitals are very similar to that of the Hartree-Fock scheme. In fact,

¹The Gaussian density basis function ϕ_{ρ} should match the Gaussian orbital basis function ϕ_{ks} at least. With $\phi_{\rho} \sim \phi_{ks}^2 \sim e^{\frac{-r^2}{2\sigma^2}} e^{\frac{-r^2}{2\sigma^2}}$ follows $\phi_{\rho} \sim e^{\frac{-r^2}{\sigma^2}}$ with $\sigma_{\rho} = \frac{\sigma}{\sqrt{2}}$. Also a second ϕ_{ρ} with half of the width is taken into account.

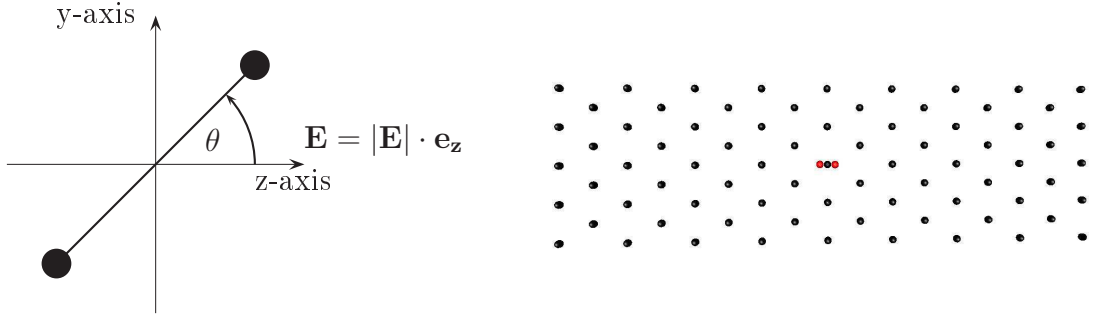


Figure 3.2: Left) Sketch of a dimer in the electric field \mathbf{E} under an angle θ . Right) The hexagonal grid with $N_1 = 9$, $N_2 = 9$ (black points) and an aligned ($\theta = 0$) O_2 molecule (red points) in the yz -plane with the same coordinate system as in the left figure.

more sophisticated quantum chemistry methods show that the single-particle picture is a good approximation. This gives us the opportunity to use the Kohn-Sham orbitals to analyze the ionization process. In particular, the valence shell is of special interest, since the laser-electron interaction affects primarily the weakly bound valence electrons.

The Kohn-Sham spectrum is plotted in Fig. 3.3, where also the occupied orbitals are indicated by their symmetry labels. There, nondegenerate σ -orbitals and doubly degenerate π -orbitals (for one spin-component) appear, which are *gerade* (index g) or *ungerade* (index u) under inversion. The doubly degenerate π -state can be located in the yz -plane defined by the laser polarization and the molecular axis, than indicated as $\pi^{(y)}$, or perpendicular marked as $\pi^{(x)}$. As one can see, the next unoccupied orbitals have much higher eigenenergies near the threshold to the continuum ($E = 0$). Furthermore, many continuum states ($E > 0$) occur due to the additional basis functions in the yz -plane filling the continuum very densely up to energies of 20 eV. They are necessary for a good description of the ionization process which we are interested in. The electronic ground state of N_2 (singlet state: $1\sigma_g^2 1\sigma_u^2 2\sigma_g^2 2\sigma_u^2 1\pi_u^4 3\sigma_g^2$) and O_2 (triplet state: $1\sigma_g^2 1\sigma_u^2 2\sigma_g^2 2\sigma_u^2 1\pi_u^4 3\sigma_g^2 1\pi_g^2$) show significant differences. While the highest occupied molecular orbital (HOMO) in the nitrogen molecule is a bonding σ_g orbital, we find for the oxygen dimer an antibonding π_g orbital (see Fig. 3.1). Due to the symmetry, the electronic density of the HOMO is located along the molecular axis for nitrogen and perpendicular to the molecular axis for oxygen.

It is known from Koopman's Theorem for the DFT-theory [134, 135] that the Kohn-Sham energy of the HOMO has a physical meaning and is equal to the ionization energy I_p which gives for N_2 10.8 eV ($3\sigma_g$ orbital) and for O_2 8.2 eV ($1\pi_g$ orbital). Due to the LSDA approximation, we find that the ionization energy is underestimated in comparison with the

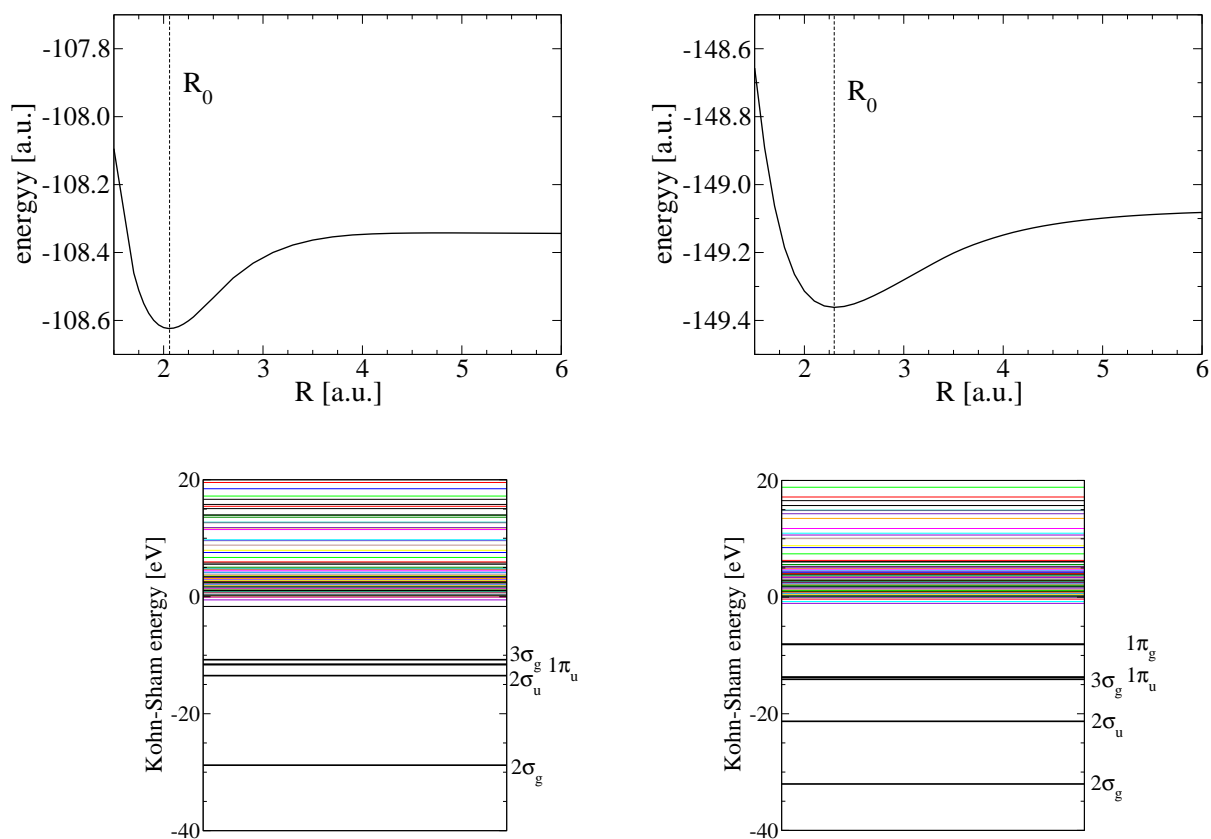


Figure 3.3: The ground state potential energy surface (top), and the Kohn-Sham energy spectrum (bottom) of N_2 (left) and O_2 (right) for the equilibrium distance R_0 . The occupied orbitals are labeled by their symmetry.

Kohn-Sham basis					density basis				
l	f	σ_1 [a.u.]	σ_{max} [a.u.]	N	l	f	σ_1 [a.u.]	σ_{max} [a.u.]	N
0	1.8	0.032	6.243	10	0	1.8	0.01	3.493	11
1	1.8	0.414	7.817	6	1	1.8	0.248	4.686	6
2	1.8	0.906	9.509	5	2	-	-	-	-

Table 3.1: Gaussian basis centered at each nitrogen nucleus for the Kohn-Sham orbitals (left) and the density (right).

Kohn-Sham basis					density basis				
l	f	σ_1 [a.u.]	σ_{max} [a.u.]	N	l	f	σ_1 [a.u.]	σ_{max} [a.u.]	N
0	1.8	0.029	5.784	10	0	1.8	0.006	4.090	12
1	1.8	0.064	7.053	9	1	1.8	0.045	4.975	9
2	1.8	0.252	8.571	7	2	1.8	1.038	6.052	4

Table 3.2: Gaussian basis centered at each oxygen nucleus for the Kohn-Sham orbitals (left) and the density (right).

experimental values of 15.6 eV (N_2) resp. 12.3 eV (O_2) [136]. Therefore, the single ionization probability will generally be overestimated in the LSDA calculations. To obtain better results, more complicated xc-functionals than the LSDA functional had to be used which is beyond the scope of this thesis. However, the order of the ionization energies of N_2 and O_2 , obtained by using Koopman's Theorem, are correct ², and we are more interested in the wavelengths- and orientation dependence of the ionization than in the absolute values of the ionization probabilities.

3.1.2 Wavelength Dependence of the Ionization

While experiments were done with a 800 nm laser showing the angular dependence of the ionization probability for N_2 and O_2 [130], we are also interested in effects for other wavelengths experimentally available in the infrared to near ultraviolet domain (1064 nm – 266 nm). Therefore, calculations were performed for aligned molecules with a fixed pulse length of 8 fs and an intensity of $2 \cdot 10^{14} \frac{W}{cm^2}$ and different laser frequencies. The single and double ionization was calculated using the definitions (2.49) and (2.50). For these laser pa-

²The experimental values can be obtained by scaling with the same factor of nearly 1.45.

λ [nm]	σ [a.u.]	d [a.u.]	N_1	N_2
266	6.653	5.36	9	7
355	5.080	5.3	9	9
400	4.588	3.88	9	9
800	5.448	5.7	9	9
1064	3.039	3.38	9	9

Table 3.3: Parameters of the hexagonal grid of s-type Gaussians laid out in the y-z plane. (σ width of the Gaussians).

parameters the Keldysh parameter γ ³, commonly used to distinguish between the tunneling ($\gamma \ll 1$) and multiphoton regime ($\gamma \gg 1$) of ionization, lies between 2.4 (266 nm) and 0.8 (800 nm) which is more or less near the limit between the tunneling and multiphoton regime. In Figure 3.4 (left) the time-dependence of the single ionization probability of N_2 is plotted for different wavelengths. The qualitative behaviour is very similar for all wavelengths. The strongest increase of ionization is around 8 fs, where the laser intensity is maximal. A step-like behaviour is found with half the period of the laser. The modulation is caused by the current electric field and is most pronounced for the longest wavelength of 800 nm, in particular. The plateaus indicate the time for the zero-crossing of the electric field and the rising edges the time with the maximal absolute field strength. The right side of Fig. 3.4 shows the strong dependence of the ionization on the laser wavelength. For longer wavelengths the ionization is much smaller than for shorter ones, which is understandable in the multiphoton picture due to the different photon energies (266 nm: 4.66 eV versus 800 nm: 1.55 eV). Therefore, far fewer photons for a wavelength of 266 nm are necessary to ionize the nitrogen resp. oxygen molecule, which has an ionization energy of 15.6 eV resp. 12.3 eV [136]. Furthermore, the ionization is of the same order of magnitude for both dimer species due to similar ionization energies.

Double ionization is much smaller than single ionization, as expected, and shows the same qualitative behaviour as a function of the wavelength since the primary effect is the single ionization. Note, that the double ionization probability may be underestimated, since the TDDFT-calculations with the LSDA-functional are not capable to describe nonsequential double ionization (NSDI) (see for example in [137]).

³The Keldysh parameter is defined as $\gamma = \sqrt{\frac{I_p}{2U_p}}$ with the ionization potential I_p and the ponderomotive potential $U_p = \frac{\mathbf{E}^2}{4\omega^2}$ (energy of a laser-driven free electron).

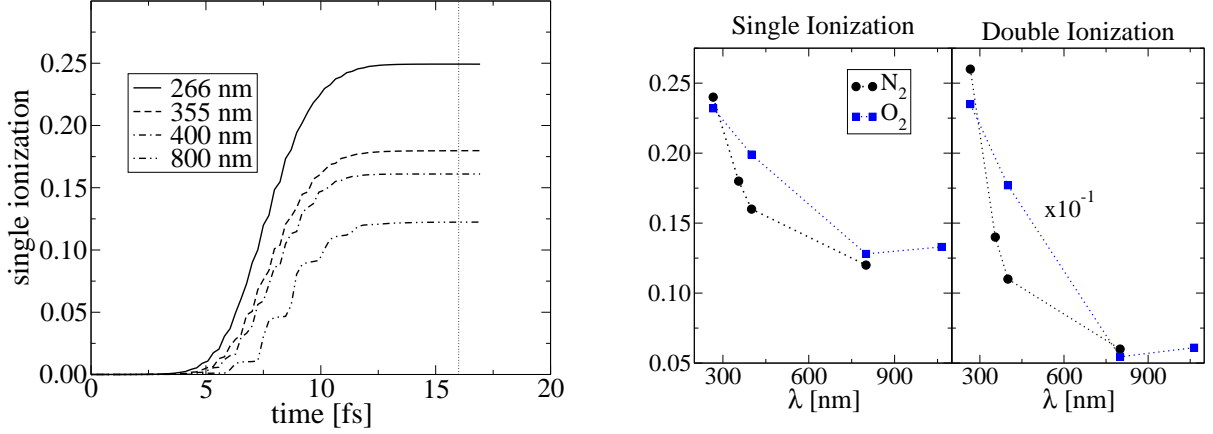


Figure 3.4: (Left) Single ionization probability of aligned N_2 as a function of time for different wavelengths (laser parameters: pulse length $T = 8$ fs, intensity $I = 2 \cdot 10^{14} \frac{W}{cm^2}$). (Right) Wavelength dependence of the single and double ionization probability of the aligned N_2 and O_2 molecule.

3.1.3 Orientation Dependence of the Ionization

Using the same laser pulse with a pulse length of 8 fs and intensity of $2 \cdot 10^{14} \frac{W}{cm^2}$ we have calculated the ionization probabilities depending on the angle between the laser polarization and the molecular axis θ ⁴.

Nitrogen

For nitrogen one can see the characteristic decrease of the single ionization probability P^1 (and also of the double ionization probability P^2) with increasing θ for all shown wavelengths in Fig. 3.5. The functional dependence can be plotted as

$$P(\theta) = P_{\parallel} \cos^2(\theta) + P_{\perp} \sin^2(\theta), \quad (3.3)$$

where P_{\parallel} and P_{\perp} are the ionization probability for $\theta = 0^\circ$ resp. $\theta = 90^\circ$. The ratio $\frac{P_{\parallel}}{P_{\perp}}$ varies between 1.3 (for 266 nm, 355 nm and 400 nm) and 1.6 (800 nm). In the experimental work of Corkum [130] the effect was much larger ($\frac{P_{\parallel}}{P_{\perp}} \approx 4$) which may be caused by the longer laser pulse of 40 fs with the same intensity of $2 \cdot 10^{14} \frac{W}{cm^2}$ ($\lambda = 800$ nm).

The study of the Kohn-Sham orbitals gives a clue about the physical mechanism of the alignment-dependent ionization. In the upper left of Fig. 3.6 the norms of the distinct Kohn-Sham orbitals after the laser pulse are plotted as function of the angle θ for $\lambda = 266$ nm⁵. The deeper bound KS-orbitals are unaffected ($2\sigma_g$) or nearly unaffected ($2\sigma_u$ and $1\pi_u^{(x)}$) by

⁴For numerical reasons the dimer was rotated, and the laser polarization was fixed to the z-direction in which the Gaussian grid has the largest extension (see picture 3.2).

⁵Only the orbitals of the spin-up electrons are shown since the orbitals of the spin-down electrons are similar.

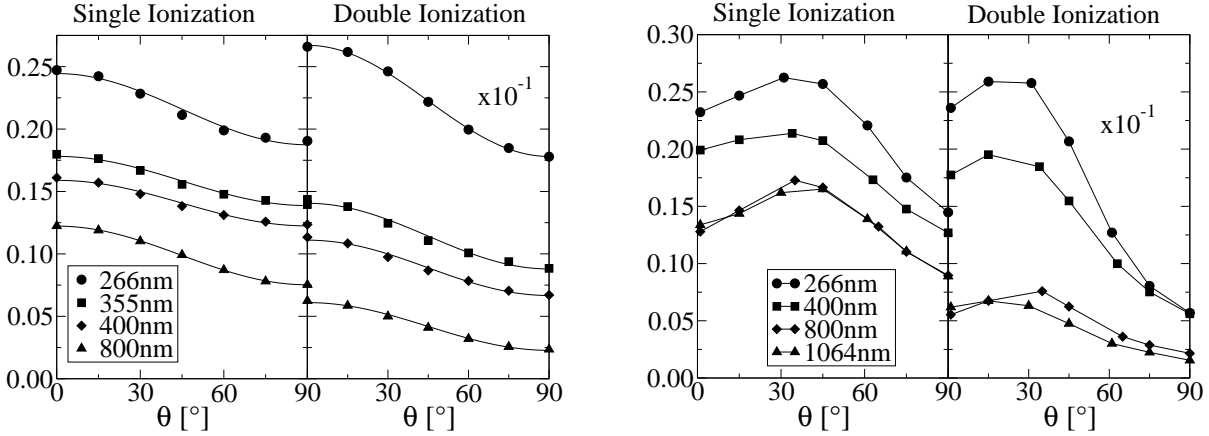


Figure 3.5: Angular dependence of the single and double ionization probability of N₂ (left) and O₂ (right) for different wavelengths. The full lines are fitted functions according to Equation 3.3 in the case of N₂.

the laser interaction. Thus the frozen core approximation for the two innermost 1s-electrons of each nitrogen atom is justified.

Only the two uppermost KS-orbitals ($1\pi_u^{(y)}$ and $3\sigma_g$) are strongly ionized and determine the ionization probability. Remarkable is the strong but contrary angular dependence of both orbitals. The outermost $3\sigma_g$ -orbital is stronger depopulated at $\theta = 0^\circ$ than at $\theta = 90^\circ$, whereas the $1\pi_u^{(y)}$ -orbital shows the opposite behaviour. In particular, the $3\sigma_g$ -orbital is more ionized than the $1\pi_u^{(y)}$ -orbital at $\theta = 0^\circ$ and the order is reversed at $\theta = 90^\circ$. This is not surprising and can be explained by the geometrical shape of the molecular orbitals: the $3\sigma_g$ -orbital/ $1\pi_u^{(y)}$ -orbital is aligned parallel/perpendicular to the molecular axis. However, the ionization of the outermost $3\sigma_g$ -orbital dominates, and therefore, the single ionization probability shows the angular dependence of the $3\sigma_g$ -orbital (Fig. 3.5). This shows that the assumption of the single-electron theories using only the HOMO, like IMST, is basically confirmed, but may be modified by many-electron effects.

For all four wavelengths the same qualitative picture of the single ionization probability is valid but there are differences in the strength of the ionization of the different orbitals. Especially the calculations with $\lambda = 800$ nm differs from the other three calculations with smaller wavelengths. In lower right of Fig. 3.6 one can see that a third orbital is important in the ionization process for $\lambda = 800$ nm. The $2\sigma_u$ -orbital is more ionized than the $1\pi_u^{(y)}$ -orbital at $\theta = 0^\circ$, but the outermost orbital $3\sigma_g$ still dominates the ionization. The angular behaviour of the $2\sigma_u$ -orbital and the $3\sigma_g$ -orbital is similar because both orbitals are aligned parallel to the molecular axis. The ionization of the $2\sigma_u$ -orbital is much weaker and nearly vanishes at $\theta = 90^\circ$. The decrease of the $1\pi_u^{(y)}$ -orbital with increasing θ is not as large as in the calculations with $\lambda = 266$ nm (Fig. 3.6). So the norms of the $1\pi_u^{(y)}$ -orbital and the $3\sigma_g$ -orbital are never changing the order for increasing θ . These differences cause the larger ratio $\frac{P_{\parallel}}{P_{\perp}}$ of $\lambda = 800$ nm compared with $\frac{P_{\parallel}}{P_{\perp}}$ of the smaller wavelengths.

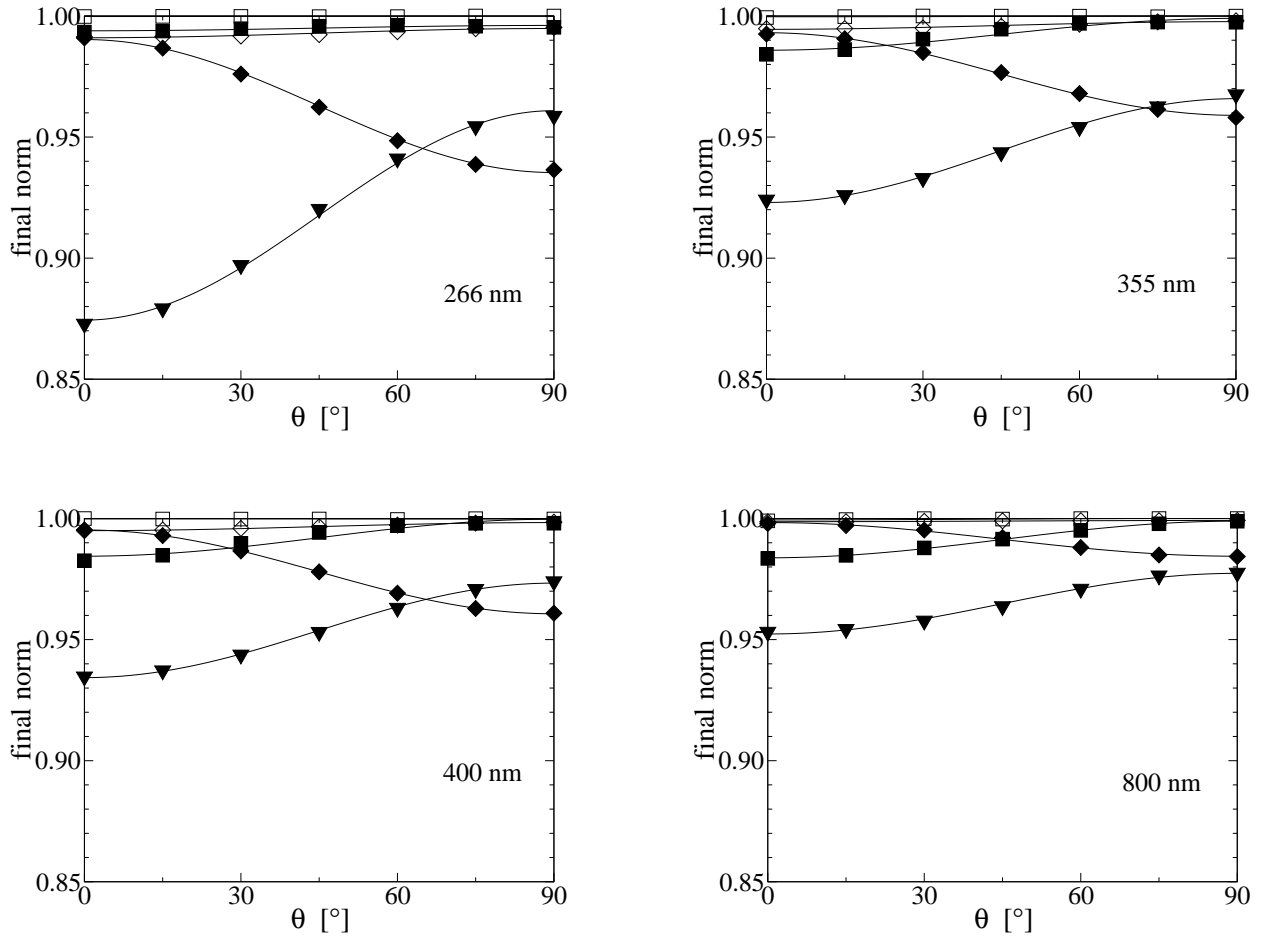


Figure 3.6: Angular dependence of the norms of the spin-up Kohn-Sham orbitals of N_2 for $\lambda = 266, 355, 400$ and 800 nm with the states $2\sigma_g$ (\square), $2\sigma_u$ (\blacksquare), $1\pi_u^{(x)}$ (\diamond), $1\pi_u^{(y)}$ (\blacklozenge) and $3\sigma_g$ (\blacktriangledown). The full lines are fitted functions according to Equation 3.3.

Oxygen

Since O_2 has another electronic structure than N_2 with an outermost π_g -orbital, the single ionization probability has a different angular dependence. For all shown wavelengths there is a maximum of the single ionization probability near $\theta = 45^\circ$ (Figure 3.5). As mentioned above, O_2 is a triplet-state with a singly occupied $1\pi_g^{(x)}$ and a singly occupied $1\pi_g^{(y)}$ -state as the highest orbitals. The maximum of the single ionization probability corresponds to the behaviour of the $1\pi_g^{(y)}$ -HOMO with a minimum of the norm at $\theta = 45^\circ$ (see the $1\pi_g^{(y)}$ state in the graphs of Fig. 3.7). As mentioned above, the geometrical shape of the orbital induces the angular dependence which favours ionization in the direction of 45° in the case of the $1\pi_g^{(y)}$ -orbital. The norm of the second HOMO, the $1\pi_g^{(x)}$ -orbital (perpendicular to the laser-molecule plane), increases for larger θ , which is the same behaviour as σ -orbitals show. This corresponds to the shape of the $1\pi_g^x$ -orbital projected on the laser-molecule plane. For $\lambda = 400$ nm it is ionized even more than the $2p\pi_g^{(y)}$ -orbital (see Fig. 3.7). However, the characteristic angular behaviour of the total ionization results from one orbital, the outermost $\pi_g^{(y)}$ -orbital, also in the case of O_2 . All other deeper bound states are more or less unaffected. An exception is the (bonding) $1\pi_u^{(y)}$ -orbital for a wavelength of 400 nm with minimal ionization for $\theta = 0^\circ$ and a maximum for $\theta = 90^\circ$. The orbital has the contrary behaviour of a σ -orbital, and differs also from the (antibonding) $\pi_g^{(y)}$ due to another shape. Since the orbital does not dominate the ionization process, the single ionization is not affected. However, it is worth to note that the bonding respectively the antibonding character of the π -orbitals changes the angular dependence of the ionization drastically. Therefore, it would be interesting to study a dimer whose highest occupied orbital has π_u symmetry. In that case, the ionization should be larger for molecules perpendicular to the laser field than for aligned molecules. Similar results for the π_u -state were found in full 3d-calculations of the 1-electron Schrödinger equation for H_2^+ [138].

The double ionization probability is one order of magnitude smaller than single ionization probability, and shows a slightly different behaviour. The maximum of double ionization probability is shifted to smaller angles with $\theta = 25^\circ$ (see Fig. 3.5). According to Equation (2.50) the double ionization is dominated by the two most ionized orbitals. Therefore, not only the angular dependence of the $\pi_g^{(y)}$ -orbital but also of the $\pi_g^{(x)}$ orbital is important. The interplay of both orbitals with an ionization maximum at $\theta = 45^\circ$ ($\pi_g^{(y)}$) and at $\theta = 0^\circ$ ($\pi_g^{(x)}$) leads to the orientation dependence of the double ionization probability.

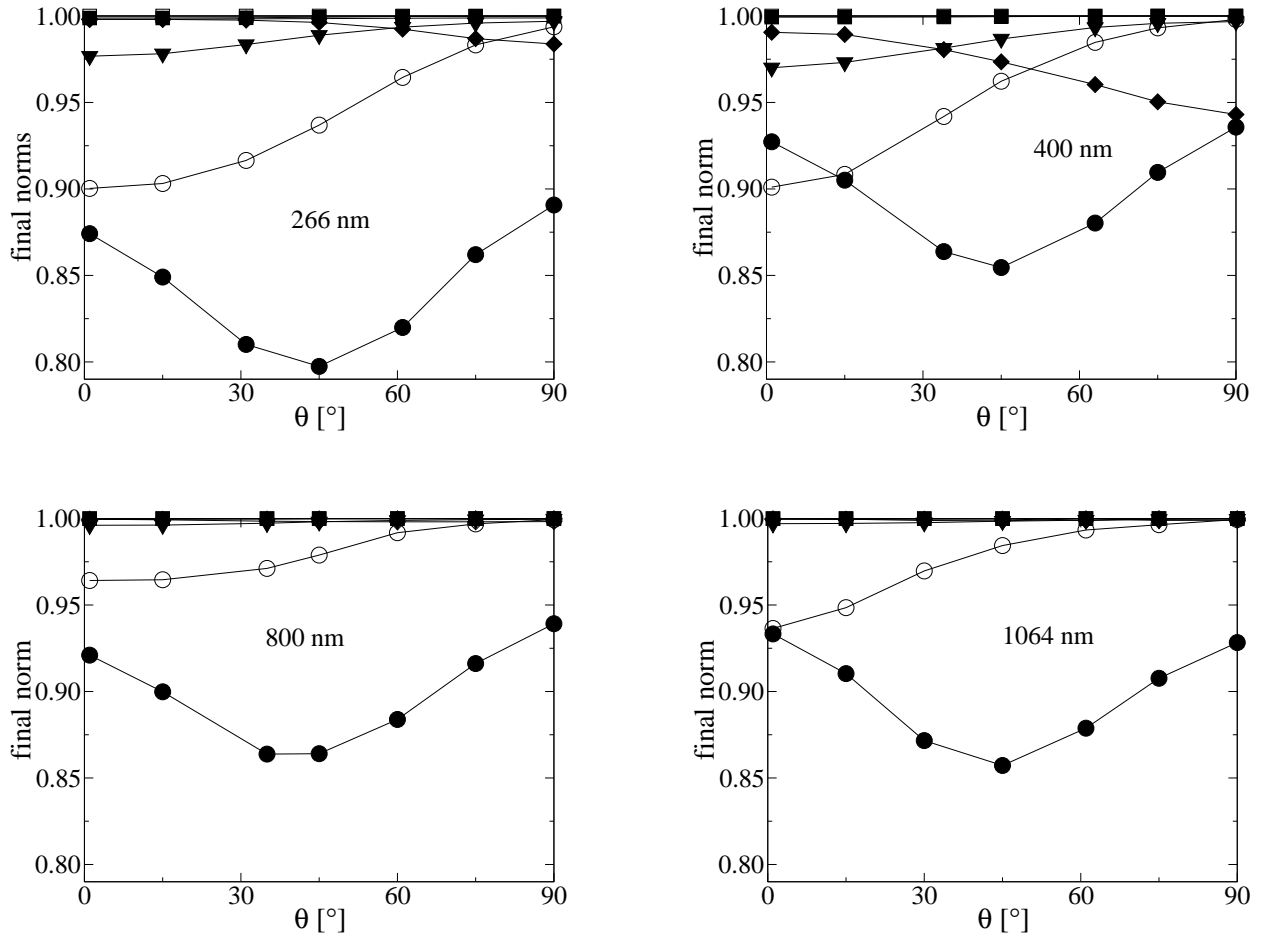


Figure 3.7: Angular dependence of the norms of the spin-up Kohn-Sham orbitals of O₂ for $\lambda = 266, 400, 800$ and 1064 nm with the states $2\sigma_g$ (\square), $2\sigma_u$ (\blacksquare), $1\pi_u^{(x)}$ (\diamond), $1\pi_u^{(y)}$ (\blacklozenge), $3\sigma_g$ (\blacktriangledown), $1\pi_g^{(x)}$ (\circ) and $1\pi_g^{(y)}$ (\bullet).

3.2 Isomerization and fragmentation of organic molecules

In this section the dynamics of diimide (N_2H_2) under excitation of femto-second laser pulses is investigated [52]. Distinct fragmentation channels are observed in particular by varying the laser frequency, and will be presented. Furthermore, we study the cis-trans isomerization on the first excited state surface S_1 taking place on a femtosecond time scale (~ 25 fs). The photoisomerization process is a genuine nonadiabatic process for two reasons: of course by the initial electronic excitation by the laser, but also by the strong coupling between the ground and the first excited state near the conical intersection (or in other cases the avoided crossing).

The laser-induced dynamics of organic molecules became a very active field of research during the last decade [139]. Today the mechanism of photoisomerization, in particular the cis-trans isomerization, plays an important role in many biological, chemical and physical processes. The first step in vision represents one prominent example [140, 141].

Experimentally, numerous studies have been performed to investigate the photoinduced dynamics of organic molecules [142–147]. Stilbene [142] and azobenzene [143] represent prototypes of systems exhibiting ultrafast cis-trans isomerization. For pyridine (a molecule of the azobenzene group) the cis-trans isomerization has been controlled in both directions using UV-vis spectroscopy with different wavelengths [144]. The photoinduced trans to cis isomerization of azobenzene and the reverse (thermal) isomerization process have been observed with NMR spectroscopy [145]. In addition, azobenzene and related molecules have been successfully used as building blocks in polymers to allow for potential applications, such as the manipulation of liquid crystals ([146] and refs. therein), the construction of holographic data storages ([143] and refs. therein) or the production of mechanical work in molecular optomechanical cycles (MOC) [147].

Theoretically, different methods have been developed to investigate the mechanism of the cis-trans isomerization [71, 148–152]. Qualitatively, the process can be understood using a two-surface model for the propagation of the nuclear wave packet including the nonadiabatic coupling but restricting the nuclear dynamics to a few (i.e. essential) degrees of freedom [148]. With such an idealization it is possible to describe systems as large as rhodopsin [149]. All nuclear degrees of freedom are included in the so-called "nonadiabatic Car-Parrinello molecular dynamics" which was used to study the isomerization of formalimine H_2CNH by treating the classical nuclear dynamics on the ground and first excited surface including a Tully hopping mechanism [71]. Alternatively, the "ab initio multiple spawning" wave function method has been applied to study the cis-trans isomerization of azobenzene [150] and ethylene (C_2H_4) [151]. Very recently, two different implementations of time-dependent density functional theory (TD-DFT) coupled with classical molecular

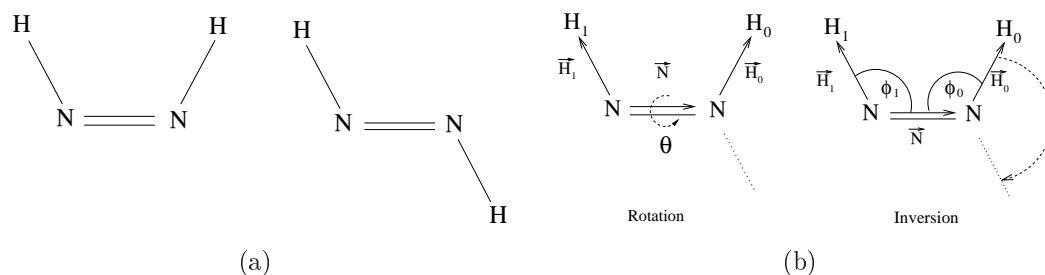


Figure 3.8: (a) Diimide isomers: cis-form with C_{2v} symmetry (left) and trans-form with C_{2h} symmetry (right). (b) Nuclear degrees of freedom of diimide. For the cis-trans isomerization two possibilities are indicated: rotation around the N=N dihedral angle θ (left), and the inversion of the angles ϕ_0 or ϕ_1 in the molecular plane (right).

dynamics (MD) have been used to investigate, amongst others, the photoinduced cis-trans isomerization of diimide [152].

In all approaches summarized above [71, 148–152], the laser field leading to the electronic excitation is not treated explicitly, i.e., the initial excitation is assumed to lift the system instantaneously to the excited state. This shortcome is overcome by the NA-QMD calculations, which were performed only for the dynamics of ethylene in fs-laser pulses as a function of the laser parameters [50], taking into account the laser field explicitly. It was found that one can selectively excite different bonds leading to distinct fragmentation or isomerization processes. The calculated time of the cis-trans isomerization is in excellent agreement with experimental data (see refs. in [50]).

Here, we are interested in the nonadiabatic dynamics of diimide under excitation of fs-laser pulses, in particular the electronically excited dynamics leading possibly to the cis-trans photoisomerization.

3.2.1 The ground state properties of the diimide molecule N_2H_2

For the diimide molecule the exchange-correlation functional is approximated again by the LDA approach, which is suited to describe the system as we will show. The basis is given by the cc-pVDZ basis set [153]. This basis comprises 14 (s,p and d-type) basis functions for each nitrogen atom and 5 (s and p-type) functions for each hydrogen atom. The two innermost electrons of nitrogen have been treated in the frozen core approximation. Since we are mainly interested in excitation processes excluding ionization, no additional basis functions and no absorber is considered, which would also slow down the calculation time. Figure 3.8(a) shows the two (most) stable planar isomers of diimide. The trans-form is slightly more stable than the cis-form.

Diimide has six nuclear degrees of freedom (see Fig. 3.8(b)), the double bond length NN ($\equiv |\vec{N}|$), the N-H bond lengths N_0H_0 ($\equiv |\vec{H}_0|$) and N_1H_1 ($\equiv |\vec{H}_1|$), the angles between the N

Isomer		LDA ^a	DFT [152]	B3LYP [161]	CI [159]	LSDA [158]	Exp. [156]
cis	NN [a_0]	2.362	2.363	2.338	2.366	2.353	-
	NH [a_0]	2.075	2.003	1.967	1.939	1.996	-
	ϕ [$^\circ$]	114.0	113	113.0	112.3	113.4	-
trans	NN [a_0]	2.381	2.363	2.340	2.368	2.364	2.366
	NH [a_0]	2.056	1.985	1.956	1.915	1.985	1.943
	ϕ [$^\circ$]	105.6	106	107.0	107.0	105.8	106.8
	ΔE_{c-t} [eV]	0.21	0.2	0.27	0.14	0.22	-
	ΔE_{INV} [eV]	2.05	-	2.04	2.52	2.00	-
	ΔE_{ROT} [eV]	3.19	-	-	-	-	-

^athis work

Table 3.4: Geometrical and ground state properties of diimide obtained with LDA (this work) and compared to different previous calculations [152,158,159,161] (see text) as well as available experimental data [156]. Here, ΔE_{c-t} is the difference in the total ground state energies between the cis and the (more stable) trans-state. The barriers for the trans→cis isomerization on the ground state surface for the inversion process in plane ΔE_{INV} (right side in Fig. 3.8(b)) and the internal rotation around the dihedral angle ΔE_{ROT} (left side in Fig. 3.8(b)) are given.

and H atoms ϕ_0 and ϕ_1 , and the dihedral angle θ . The three angles are defined to be always positive and smaller than π . The dihedral angle θ can be used to distinguish between the two isomers. Using two planes, characterized by the vectors $\vec{n} = \vec{N} \times \vec{H}_1$ and $\vec{m} = \vec{N} \times \vec{H}_0$, it is determined by

$$\cos \theta = \frac{\vec{m} \cdot \vec{n}}{|\vec{m}| \cdot |\vec{n}|}. \quad (3.4)$$

Thus, the dihedral angle is $\theta = 0$ for the cis-form and $\theta = \pi$ for the trans-form. Note that the definition (3.4) of θ becomes problematic if ϕ_0 or ϕ_1 approaches π . In the ground state one has of course $N_0H_0 = N_1H_1 \equiv NH$ and $\phi_0 = \phi_1 \equiv \phi$ for both isomers.

There exists a lot of experimental [154–156] and theoretical quantum chemical work [152, 157–161] for ground state properties and excitation energies of diimide. In Table 3.4, the calculated ground state geometry parameters NN, NH ($a_0 \equiv 1$ bohr), ϕ and the differences between the total ground state energies of the cis and the trans-state, ΔE_{c-t} , are presented, as obtained with the present LDA approach. They are compared with the results from DFT(BLYP/PBE) [152], B3LYP/6-311++G(d,p) [161], CI/6-311+G(3df,2p) [159], LSDA [158] calculations and available experimental data [156]. Evidently, the results of the LDA calculations agree well with that of the more elaborated quantum chemical investigations and are in satisfactory agreement with experimental data.

So far, different idealized reaction paths for isomerization *on* the electronic ground state

	electronic state	this work	Gaussian 98 [162]	polarization
cis-form	1B_1	3.1	3.1	perpendicular
	1B_2	5.2	5.5	N=N bond
trans-form	1B_g	-	3.04	-
	1A_g	-	6.69	-
	1B_u	6.3	6.7	in plane
	1A_u	8.3	8.5	perpendicular

Table 3.5: The lowest excitation energies of diimide (in eV) calculated according to our time-dependent procedure with δ -peak pulses [43, 50] (this work) and in linear response theory using the Gaussian 98 code [162] with LDA option. The last column gives the corresponding laser polarization axes leading to the particular transitions: perpendicular to the molecular plane (perpendicular), within the molecular plane and perpendicular to the N=N double bond (in plane) and along the nitrogen double bond (N=N bond). The dipole transitions to the 1B_g and 1A_g states are forbidden.

surface have been discussed [157–160], in particular, the inversion of the N-H bonds within the molecular plane changing ϕ_0 respectively ϕ_1 (right side in Fig. 3.8(b)), and the internal rotation of the N-H bonds around the N=N double bond, changing the dihedral angle θ (left side in Fig. 3.8(b)). For both cases, the calculated energy barriers $E_{INV} \approx 2$ eV and $E_{ROT} \approx 3$ eV, respectively, for a trans \rightarrow cis isomerization are also given in Table 3.4.

In Table 3.5, the calculated dipole excitation energies of both isomers are given. In the present work, the calculated dipole excitation energies have been calculated by using the NA-QMD formalism with a δ -peak laser pulse in the linear regime [43, 50]. They are compared with the results obtained in linear response theory using the GAUSSIAN 98 code [162] with LDA option. For completeness, the corresponding polarizations of the laser leading to the individual transitions are given in Table 3.5, too. Note that the dipole transition from the trans-form to the first two excited states are forbidden for symmetry reasons.

For the first transition (3.1 eV) we have calculated the ground state S_0 and excited state S_1 surfaces as a function of the dihedral angle θ in configuration-interaction-singles (CIS) approximation using the Gaussian 98 code (see Fig. 3.9). As expected from previous work [152, 160, 163] there are conical intersections around $\theta \approx 90^\circ$ which will dominate the dynamics of the cis-trans isomerization (see next section). Of course, the exact position of the conical intersections depends on the other five nuclear coordinates, i.e. the bond lengths and angles. With the dynamical calculations presented in the next section, one can quantitatively characterize this region of conical intersections within the six-dimensional surfaces (see below).

At this point, it should be noted that in the region of conical intersections a single deter-

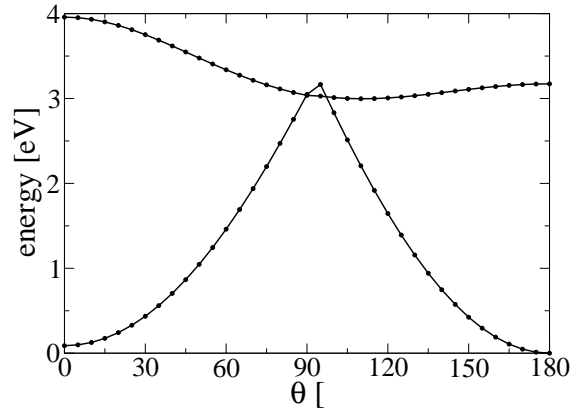


Figure 3.9: PES of the ground state S_0 and the first excited state S_1 as a function of the dihedral angle θ computed in CIS approximation with Gaussian 98 [162]. Note that the excitation energy at $\theta = 0^\circ$ is about 0.8 eV larger as compared to the LDA results (Table 3.5) in accordance with previous CI-calculations [157, 159]. The bond angles and lengths are fixed to be the values of the cis-isomer.

minant approach (like LDA in the KS-approach) is not capable of describing the ground and excited state potential surfaces properly within linear response theory. In this case, the ground state density has to be computed, which can be a problem with very distorted geometries and/or if the ground and excited states differ significantly in the electronic structures (see also the next section). In contrast, in explicit time-dependent calculations (as presented in the next section) one only needs to know the time-dependent excited KS wave functions, and no information is required concerning the ground state. Hence, no convergence problems do occur in the vicinity of conical intersections (for a more detailed discussion of this point and the error introduced by use of LDA, in particular for diimide, see [152]).

In the next section, we will characterize the main features of the dynamics of the molecule by exciting it with fs-laser pulses with central frequencies corresponding to the individual transitions given in Table 3.5, i.e. 3.1 eV, 5.2 eV (cis-isomer) and 6.3 eV, 8.3 eV (trans-isomer).

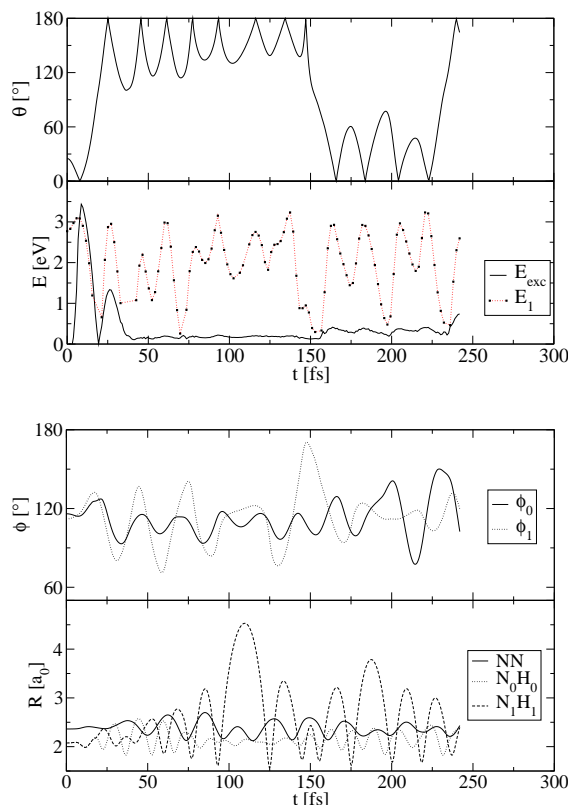


Figure 3.10: Dynamics of cis-diimide excited from the electronic ground state to the first excited state by a short laser pulse (see text). The nuclear degrees of freedom are shown as function of time: the dihedral angle $\theta(t)$ (upper graph), the angles $\phi(t)$ between the N-H bonds and the bond lengths $R(t)$ (lower graph). In addition, the electronic excitation energy $E_{exc}(t)$ and the energy of the first excited state $E_1(t)$ of the actual nuclear configuration are presented (upper graph). The initial nuclear configurations are: $\theta = 25^\circ$, and $\phi_0 = 116^\circ$, $\phi_1 = 112^\circ$ and the bond lengths are those of the electronic ground state (see Table 3.4).

3.2.2 Isomerization via the 1st excited state

In the following we will consider the *dipole excitation* of the molecule explicitly and follow the subsequent nonadiabatic nuclear and electronic dynamics as a function of time. The molecule is excited using a \sin^2 pulse defined by equation 3.1. In all calculations, the pulse duration has been chosen to be $T = 5$ fs. The central frequency corresponds to the first excitation energy given in Table 3.5, i.e. $\omega = 3.1$ eV. The field strength E_0 has been varied within the range of $E_0 = 0.0377 - 0.0924$ a.u. (corresponding to the laser intensities between $0.5 \cdot 10^{14} - 3.0 \cdot 10^{14} \frac{\text{W}}{\text{cm}^2}$).

Different nuclear initial conditions have been considered. The bond lengths have been fixed to those of the electronic ground state for both isomers. The dihedral angle $\theta = 0^\circ + \Delta\theta$ has been varied with $\Delta\theta = 5^\circ, 10^\circ, \dots, 30^\circ$. The pair of the initial bond angles has been chosen to be $(\phi_0, \phi_1) = (\phi^{gs} + \Delta\phi, \phi^{gs} - \Delta\phi)$ with $\Delta\phi = 2^\circ, 4^\circ, \dots, 8^\circ$ and $\phi^{gs} = 114^\circ$ or 105.6° ,

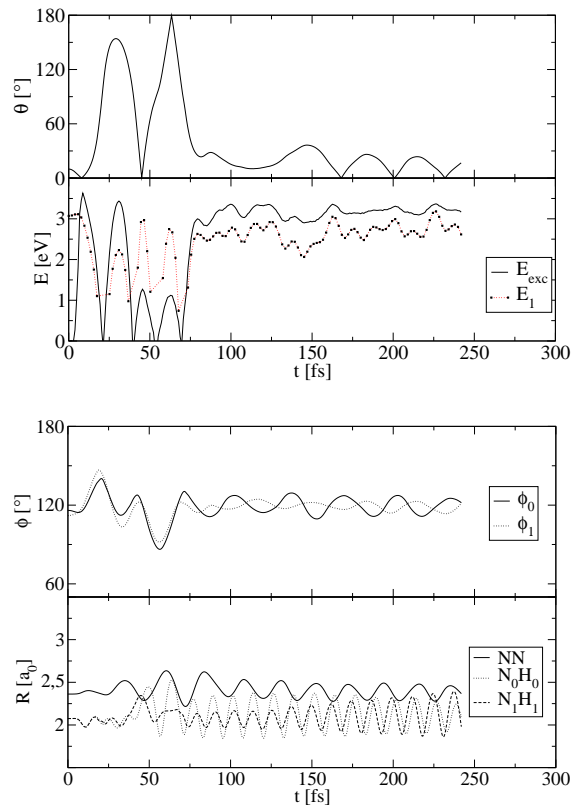


Figure 3.11: Same as in Fig. 3.10, but for an initial angle $\theta = 10^\circ$.

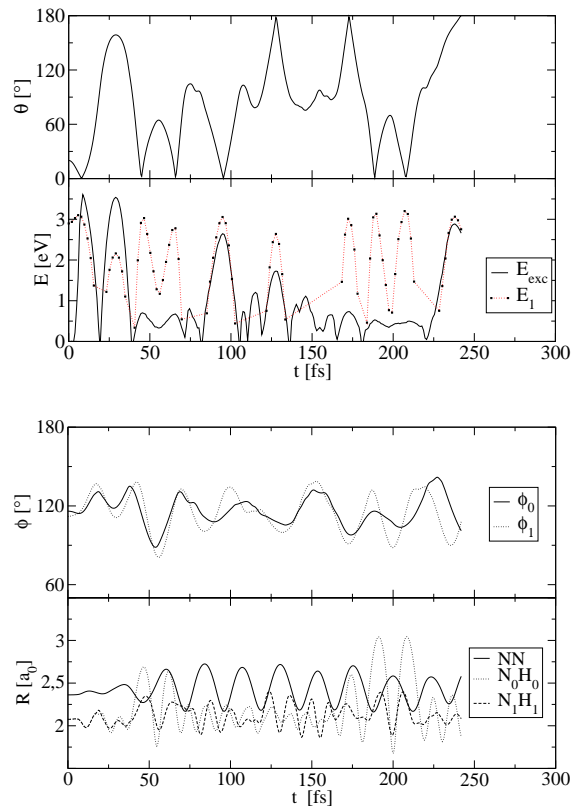


Figure 3.12: Same as in Fig. 3.10, but for an initial angle $\theta = 20^\circ$.

the angles corresponding to both ground state isomers. The initial velocities are set to zero. However, because we include the laser field explicitly, the current velocities at the time of the laser peak intensity are different in all simulations. The most important characteristic of the dynamics for the frequency $\omega = 3.1$ eV is the fact that the bond angle modes ϕ_0 , ϕ_1 and the rotational mode θ are predominantly excited. For intensities $I \leq 1 \cdot 10^{14} \frac{\text{W}}{\text{cm}^2}$ the molecule remains stable and oscillates around the equilibrium angles ϕ_0 , ϕ_1 and θ . Above an intensity of $I \approx 3 \cdot 10^{14} \frac{\text{W}}{\text{cm}^2}$, the initial motion around ϕ_0 , ϕ_1 and θ is followed immediately by fragmentation, preferentially into three products (i.e. $N_2H_2 \rightarrow N_2 + H + H$). In all examples shown below an intermediate intensity of $I = 1.5 \cdot 10^{14} \frac{\text{W}}{\text{cm}^2}$ has been used. This value guarantees that the absorbed excitation energy is approximately that of the S_1 -state (≈ 3.1 eV). The actual value, of course, depends slightly on the initial nuclear configuration. In the Figures 3.10-3.12, the dynamics of the molecule as function of time is presented for different initial conditions. All nuclear degrees of freedom are shown. Also, the actual electronic excitation energy

$$E_{exc}(t) = E_e^{td}(t) - E_e^{gs}(\mathbf{R}) \quad (3.5)$$

is plotted, with the time-dependent electronic energy $E_e^{td}(t)$ and the electronic ground state energy $E_e^{gs}(\mathbf{R})$ of the actual nuclear configuration $\mathbf{R}(t)$ (see 2.3.3, p. 24). In addition, the difference between the first excited state and the ground state energies E_1 is presented. It is calculated in linear response theory using the Gaussian 98 code [162] with LDA option for each nuclear configuration. The comparison between E_{exc} and E_1 gives insight into the electronic configuration at each time step. In particular, the case $E_{exc} = E_1 = 0$ clearly indicates that the system passes through a conical intersection⁶.

As can be seen from Figs. 3.10-3.12, in all cases, the short time behaviour ($t \lesssim 25$ fs) is nearly independent of the initial conditions. The molecule undergoes a cis-trans isomerization within a time scale of about $\tau \approx 25$ fs. The reaction path is dominated by a rotation around the dihedral angle θ (see upper part of Figs. 3.10-3.12). The first dominant motion during the excitation, however, is a significant increase of the two bond angles ϕ_0 , ϕ_1 up to a time of about 20 fs (lower part of Figs. 3.10-3.12). At the same time, the first conical intersection occurs where E_{exc} approaches zero (upper part of Figs. 3.10-3.12). This universal behaviour is in excellent agreement with the results obtained in ref. [152] for a specific trajectory. The total time of the isomerization process in [152], however, is somewhat larger as compared to our time scale which can be attributed to the additional heat bath coupled to the molecule in the calculation of ref. [152].

The long time behaviour of the electronic system can be divided into three distinct categories:

⁶As discussed in the previous section, in the linear response theory and a single determinant description (like LDA) the convergence in the calculation of E_1 is problematic at conical intersections. This is the reason, why *exactly* at the time steps, where $E_{exc}=0$ in Figs. 3.10-3.12, the corresponding calculation of E_1 is missing.

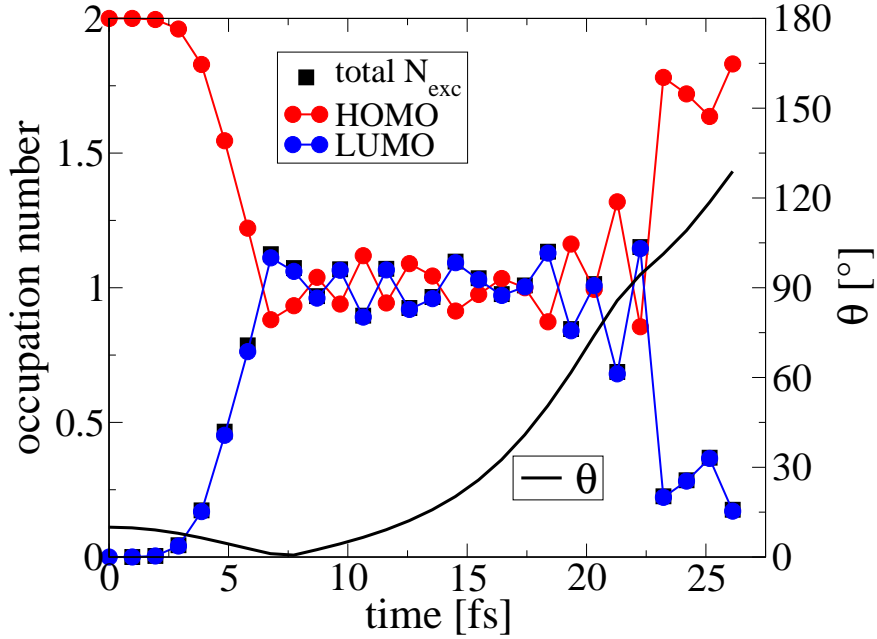


Figure 3.13: Electronic excitation of cis- N_2H_2 ($\theta \approx 0$) with a resonant (3.1eV) 5 fs pulse ($S_0 \rightarrow S_1$ transition) and the radiationless reverse reaction ($S_1 \rightarrow S_0$) at the conical intersection ($\theta \approx 90^\circ$). The total number of excited electrons, the occupation number for HOMO and LUMO states as well as the torsion angle θ is plotted as a function of time. (The laser ends at $t = 10$ fs.)

1. Ground state dynamics (Fig. 3.10)

After the excitation to the S_1 surface ($t \approx 10$ fs), the electronic system is immediately deexcited by a nonadiabatic transition around $\theta \approx 90^\circ$ passing through the intersection with $E_{exc} = 0$ at $t \approx 20$ fs. Afterwards, the molecule remains on the electronic ground state surface. Thus, the nuclear degrees of freedom are highly excited (see the large amplitude and irregular behaviour of ϕ and R in Fig. 3.10), and the molecule can even undergo adiabatic transitions between the cis- and trans-configuration on the ground state surface (see e.g. $\theta(t)$ at $t \approx 150$ fs and 225 fs). This scenario, i. e. persistence on the ground state surface, is most likely observed in our simulations. The laser excitation to the S_1 state and the deexcitation via the conical intersection is demonstrated in Fig. 3.13 by showing the occupation of the HOMO and LUMO one-particle states.

2. Excited state dynamics (Fig. 3.11)

The opposite case is shown in Fig. 3.11, where after some nonadiabatic transitions ($t \lesssim 75$ fs) the electronic system remains on the excited S_1 -state ($t \gtrsim 75$ fs) exhibiting nearly the total excitation energy. Consequently, the nuclear dynamics is almost frozen and shows nearly harmonic behaviour with small amplitudes (see $\phi(t)$ and $R(t)$ in Fig. 3.11). Evidently, the molecule is trapped within a cis-minimum on the

six-dimensional S_1 -surface (see $\theta(t)$ in Fig. 3.11).

3. Switching between ground and excited state (Fig. 3.12)

In the two previous cases, most of the excitation energy of the molecule is finally either stored into vibrational modes (see Fig. 3.10) or into electronic excitation (see Fig. 3.11). However, there are also cases where a permanent change between electronic and vibrational excitations is found. This is demonstrated in the example shown in Fig. 3.12. As can be seen clearly from the behaviour of $E(t)$, the molecule undergoes several nonadiabatic transitions between the S_0 and the S_1 state. In addition, there are several transitions between the cis- and the trans-state (see $\theta(t)$). They can occur adiabatically on one surface (e.g. at $t \approx 175$ fs) or nonadiabatically changing the electronic state (e.g. at $t \approx 225$ fs).

From the altogether 14 nonadiabatic transitions between the S_0 - and S_1 -surfaces in the examples shown in Figs. 3.10-3.12 (i.e. $E_1 \approx E_{exc} = 0$), one may quantitatively characterize the location of the intersection funnel in the six-dimensional system. By averaging over the 14 events, we obtain a mean value of the dihedral angle of $\bar{\theta} = 93.6^\circ$ with a standard deviation of 4° . The mean values of the bond angles are approximately the same $\bar{\phi}_0 \approx \bar{\phi}_1 = 120^\circ$ with a standard deviation of $\approx 13^\circ$. The mean bond lengths are basically the same as those of the ground state with a standard deviation of about 0.15 a.u.

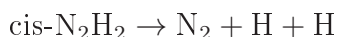
3.2.3 Selective fragmentation via higher excited states

We have also investigated the dynamics of the cis-isomer respectively the trans-isomer for other laser frequencies given by the higher resonant excitation energies in Table 3.5, i.e. 5.2, 6.3 eV and $\omega = 8.3$ eV. Also, the laser polarization has been chosen according to the directions given in the table. The field strength E_0 has again been varied within the range of $E_0 = 0.0377 - 0.0924$ a.u. (corresponding to the laser intensities between $0.5 \cdot 10^{14} - 3.0 \cdot 10^{14} \frac{\text{W}}{\text{cm}^2}$).

We find different vibrational excitation channels, which lead to different fragmentation reactions for higher laser intensities. Qualitatively, the results can be summarized as follows:

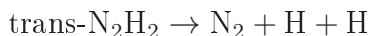
1. excitation of the cis-isomer with $\omega = 5.2$ eV

The $\overline{\text{NH}}$ -bonds are preferentially excited. The molecule remains stable up to an intensity of $I = 1.0 \cdot 10^{14} \frac{\text{W}}{\text{cm}^2}$ and dissociates to neutral N_2 and two H atoms for higher intensities.



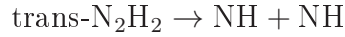
2. excitation of the trans-isomer with $\omega = 6.3$ eV

Again the $\overline{\text{NH}}$ -bonds are initially activated inducing multifragmentation for intensities larger than $1.0 \cdot 10^{14} \frac{\text{W}}{\text{cm}^2}$.



3. excitation of the trans-isomer with $\omega = 8.3$ eV

For this frequency, the activation of $\overline{\text{NN}}$ bond length mode is dominating. The nitrogen double bond breaks for intensities $I \geq 1.0 \cdot 10^{14} \frac{\text{W}}{\text{cm}^2}$ leading to fragmentation into two neutral NH dimers .



In all three cases, the rotational dihedral mode θ is practically unaffected by the excitation which is in stark contrast to the lowest frequency. Therefore, isomerization via rotation is blocked for the higher electronic resonances. That means, the cis-trans photoisomerization is only possible via the $S_0 \rightarrow S_1$ transition ($\omega = 3.1$ eV). A second point is the fact, that the back reaction, the isomerization from trans-diimide to cis-diimide, is not accessible via electronic excitation. The S_1 -state ($\omega = 3.1$ eV) is a dark state for the trans-isomer, and excitation of higher excited states ($\omega = 6.3$ eV or 8.3 eV) does not lead to isomerization. Therefore, the time scale of a possible molecular switch (*cis* \rightarrow *trans* and *trans* \rightarrow *cis*) is dominated by the thermal back reaction, which has a much larger time scale than the *cis* \rightarrow *trans* photoreaction (25 fs).

3.3 Giant collective vibrational excitation in fullerenes

In this section a much larger system will be investigated – the Buckminster Fullerene C_{60} . Fullerenes have been the subject of many dynamical studies in molecular physics since their discovery in 1985 [164]. The rather lately discovered new chemical group of fullerenes forming closed shell carbon structures are on the edge between molecules and clusters showing molecular as well as solid state properties. They are fascinating due to their highly symmetric structures and their high stability making them interesting for practical reasons in material science as well as for pure research [165]. The large size with many electronic and vibrational degrees of freedom gives rise to many effects unknown in atoms and also small molecules.

One example is the existence of plasmon excitations in C_{60} [166], which can be understood as a collective motion of the electron cloud relative to the nuclear backbone, and is already known from metal clusters and solids. The plasmon excitation in C_{60} has been widely studied in theoretical works, in particular using jellium models [167–170]. Another phenomenon, the suppression of ionization leading to unexpectedly high saturation intensities [171], has been explained either by multielectron effects [172, 173] or by multislit interference effects due to the finite cage size [174] known also from diatomics [123]. Furthermore, it has been found in experiments that the ionization process and the subsequent fragmentation depends on the laser duration going from direct multiphoton absorption for short fs laser pulses with pronounced ATI peaks in the photoelectron spectrum to statistical electron evaporation for longer pulses [175].

Experimentally the laser-induced ionization and fragmentation of fullerenes have been studied extensively [175, 176]. In two color pump probe experiments also the influence of Rydberg excitations for efficient energy absorption has been investigated [177].

Concerning the vibrational degrees of freedom of highly excited C_{60} , it has been found that fragmentation occurs mainly by the emission of carbon dimers [178], which can be understood as a thermal statistical process of a relaxed vibrational hot C_{60} cage. While the electronic relaxation leading to the statistical electron evaporation takes place on a timescale of tens of femtoseconds [175], the timescale for vibrational energy relaxation via vibrational coupling is much larger leading to fragmentation on the order of picoseconds [179, 180].

On a much shorter timescale than the fragmentation time, the laser can induce distinct vibrational modes. Using near-infrared laser pulses stable highly charged C_{60}^{z+} ions with a charge up to $z=12$ can be produced [172, 181, 182]. Furthermore, the excitation of the $H_g(1)$ vibrational mode has been proposed by using a metal sphere model [172] resp. a time-dependent adiabatic MCSCF method [183]. Theoretically, the vibrational dynamics of C_{60} induced by a laser field with visible or near-visible frequencies has been studied mainly using tight-binding methods [184–188] resp. density-functional-based tight-binding electron dynamics (DFTED) [189]. For small laser intensities several vibration regimes depending

on the laser parameters could be found with the excitation of the $A_g(1)$, $A_g(2)$ [190] resp. of the H_g modes [188]. However, for higher intensities the breathing mode $A_g(1)$ dominates in the semiempirical calculations [188, 189] in agreement with experiments for metal-doped C_{60} [191].

In this section we will study the laser-induced dynamics of the electronically highly excited C_{60} molecule taking explicitly into account all 240 valence electrons as well as all 180 nuclear degrees of freedom. Our ab-initio calculations will support the emergence of the breathing mode excitation but with a period larger than in the electronic groundstate. The breathing mode motion can be probed with a second laser pulse which has been confirmed in two-colour pump-probe experiments [53].

3.3.1 The ground state properties of C_{60}

The C_{60} molecule has the highest symmetry that can be found in a molecular system – the I_h -symmetry. It has the geometrical shape of a truncated icosahedron and consists of 20 hexagons and 12 pentagons with a carbon atom on each vertex (see Fig. 3.14). According to Euler’s theorem the pentagons are necessary to form a curved shell which would be impossible using only a hexagonal structure, i.e. graphene sheet ⁷. All pentagons are isolated from each other which reduces the local curvature respectively the local strain on the ball. This is the so-called isolated pentagon rule which says that fullerenes with isolated pentagons are energetically favoured. The smallest possible fullerene according to Euler’s theorem is C_{20} , which is much more unlikely to be produced than C_{60} due to the violation of the rule.

The structure of the buckyball is determined by only two parameters: the single C-C bond length a_5 and the double C=C bond length a_6 . The 60 single C-C bonds are the bonds forming the pentagons. The 30 double C=C bonds are located at the edge between two hexagons. Although the structure of the C_{60} molecule is not a regular truncated icosahedron (with only equal bond lengths), the I_h -symmetry is not destroyed. Alternatively, it is sufficient to know the radius R of the buckyball and the ratio $\frac{a_5}{a_6}$. The radius R is defined as the distance between the center of the buckyball and the carbon atoms.

In the time-dependent calculations the symmetry is broken, and a mean radius is defined as $R = \frac{1}{60} \sum_{i=1}^{60} R_i$ with R_i the distance of the i th atom to the center of mass of the C_{60} -cage. As a measurement of the asymmetric deformation the standard deviation of the mean radius R is used.

⁷Euler’s theorem for polyhedra is given by $f + v = e + 2$ with f the number of faces (hexagons and pentagons), v the number of vertices and e the number of edges. For a polyhedron formed by h hexagonal and p pentagonal faces the following condition can be derived: $6(f + v - e) = p = 12$. One consequence is that all fullerenes have exactly 12 pentagonal faces.

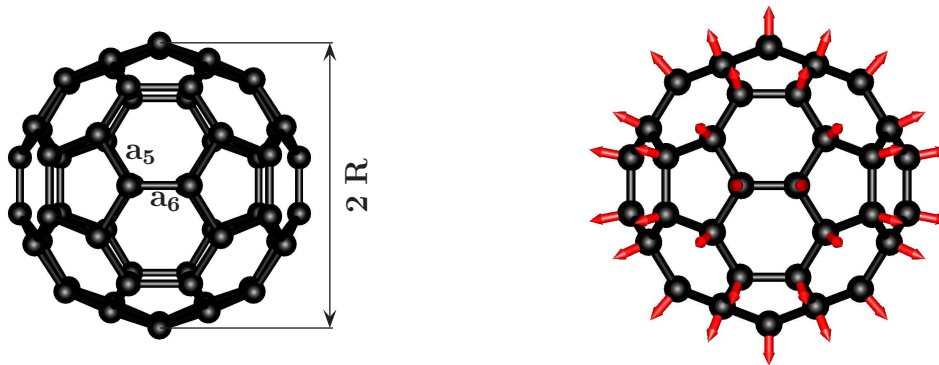


Figure 3.14: Left) The structure of C_{60} with the pentagon-hexagon single bond a_5 , the hexagon-hexagon double bond a_6 and the radius R . Right) The vibrational normal mode vector of the breathing mode $a_g(1)$ which changes only the C_{60} radius R .

The basis set

The C_{60} molecule consists of 60 carbon atoms and 360 electrons which makes molecular dynamics simulations computationally very demanding. Due to the many degrees of freedom it is necessary to restrict the basis set for the expansion of the Kohn-Sham orbitals to a few basis functions. So, we use a minimal basis set, i.e. a set of atomic basis functions (LCAO-ansatz). The atomic basis functions were calculated from an atomic carbon ground state calculation with the LDA option and are expanded itself in an auxiliary Gaussian basis. The auxiliary basis⁸ and the expansion coefficients of the atomic basis functions are given in Table 3.6.

The two 1s-core electrons of each carbon atom will be treated in the frozen core approximation using the 1s atomic orbital specified in Table 3.6. The approximation is reasonable for the deeply bound core-electrons which will not be affected by the interaction with the laser. Therefore, the basis set contains the atomic functions of the valence shell ($2s$, $2p_x$, $2p_y$, $2p_z$ orbitals) which gives in total $60 \cdot 4 = 240$ basis functions.

Additionally, a basis set for the electronic density is given in Table 3.7. It consists of two s-type functions. With the frozen core approximation for the 1s-core electrons, $4 \cdot 60 = 240$ electrons (4 valence electrons of each carbon atom) will be propagated explicitly. The electronic ground state of C_{60} is a singlet state with 120 spin-up and 120 spin-down (valence) electrons. In the following calculations, the local density approximation (LDA) for the exchange-correlation functional will be used. Only 120 Kohn-Sham orbitals have to be propagated explicitly since each Kohn-Sham orbital is occupied by a spin-up and a spin-down electron.

⁸The auxiliary basis consists of nine s-type Gaussians ($l = 0$) and 4 p-type Gaussians ($l = 1$). The Gaussians' widths are taken from the cc-pVDZ basis set [153].

		coefficients		
l	σ [a.u.]	1s	2s	2p
0	0.01224897993	0.00067804119	0.00016717639	0
	0.03162277660	0.00528347887	0.00130453647	0
	0.06622661785	0.0270546901	0.00676278672	0
	0.12431235677	0.10014582304	0.02583862261	0
	0.21790681682	0.27192731036	0.07729813618	0
	0.36527014869	0.43279188844	0.15614811959	0
	0.59793471268	0.30469266021	0.16452982688	0
	1.38475468647	0.02199811802	-0.7232367479	0
	2.50313087161	-0.0056986628	-0.4186044404	0
1	0.32548951782	0	0	-0.0489838064
	0.70675349274	0	0	-0.2404070848
	1.35382590268	0	0	-0.6470820518
	2.56748082982	0	0	-0.2675650093

Table 3.6: Gaussian basis used for the description of the atomic orbitals of carbon. Note, that there are three degenerated p-orbitals with different orientations ($2p_x$, $2p_y$, $2p_z$).

		coefficients	
l	σ [a.u.]	1	2
0	0.00094745241	-1.338322e-05	0
	0.02996107589	0.00631269766	0
	0.06696495302	0.04138988548	0
	0.13396595554	0.60029975582	0
	0.26822089039	1.31337139344	0
	0.47673129462	-0.2808334476	0
	1.07211253484	3.31699333167	0
	1.76776695297	1.00247976672	1

Table 3.7: The two basis functions used for the description of the density.

	$\omega_{A_g(1)}$ [cm ⁻¹]	$T_{A_g(1)}$ [fs]	a_5 [a.u.]	a_6 [a.u.]	R_0 [a.u.]
exp.	497 [192, 193]	67	2.74 [194]	2.64	6.72 [195]
this work	521	64	2.73	2.616	6.66
Brenner 1	358	93	2.74	2.68	6.73

Table 3.8: Groundstate properties of C₆₀.

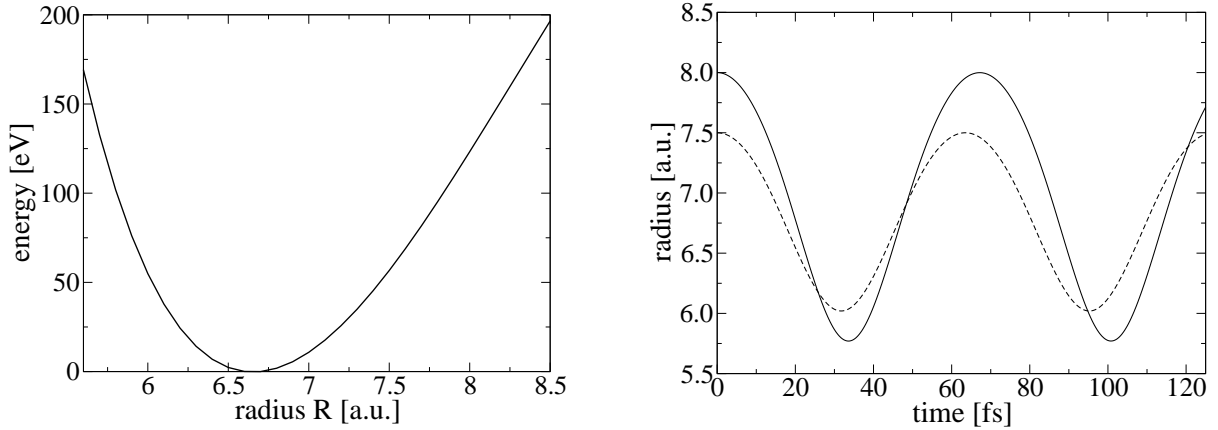


Figure 3.15: (left) The groundstate energy surface of C₆₀ as a function of the C₆₀ radius R (for a fixed ratio $\frac{a_5}{a_6} = 1.044$). (right) The breathing mode $A_g(1)$ for different initial values of the C₆₀ radius.

Geometrical conformation and breathing mode

The optimization of the geometrical groundstate configuration is done as mentioned in Section 2.3.4. Due to the symmetry restriction only two parameters, the radius R and the ratio $\frac{a_5}{a_6}$, have to be varied. We find an equilibrium radius $R_0 = 6.66$ a.u. and a ratio $\frac{a_5}{a_6} = 1.044$. In Table 3.8 the geometrical groundstate properties are listed and compared with experimental values [192–195] and an empirical model using 3-body potentials for carbon structures [97,98]. We find a good agreement with the experimental data, although the bond lengths are slightly underestimated by up to 1 %. Furthermore, the frequency $\omega_{A_g(1)}$ respectively the period $T_{A_g(1)}$ of the radial symmetric breathing mode $A_g(1)$ is listed. The vibrational mode $A_g(1)$ changes only the C₆₀ radius R and is displayed on the right hand side of Fig. 3.14. The mode will play a big role in the laser-excitation scheme.

The calculated period of 64 fs is near the experimental value of 67 fs. The groundstate energy surface as a function of the radius R is displayed in Fig. 3.15. The potential becomes anharmonic for large amplitudes R which enhances also the period slightly (right side Fig. 3.15). This effect has to be distinguished from the effect we will see in the case of electronic excitation by a laser field (see the next sections).

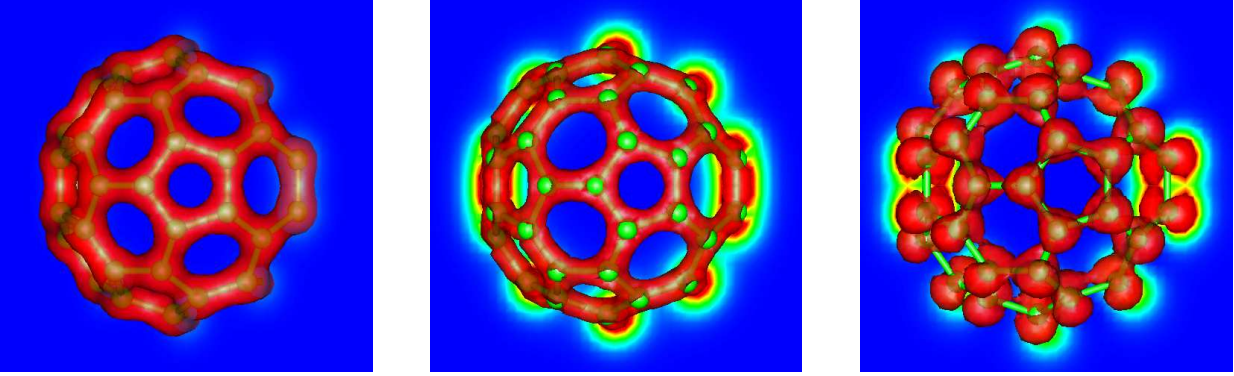


Figure 3.16: The electronic density of C_{60} of all electrons $\rho(\mathbf{r}) = \sum_{\sigma} \sum_{i=1}^{120} |\Psi^{i\sigma}(\mathbf{r})|^2$ (left), of the σ orbitals $\rho_{\sigma\text{-orbitals}} = \sum_{\sigma} \sum_{i=1}^{90} |\Psi^{i\sigma}(\mathbf{r})|^2$ (middle) and of the π orbitals $\rho_{\pi\text{-orbitals}} = \sum_{\sigma} \sum_{i=91}^{120} |\Psi^{i\sigma}(\mathbf{r})|^2$ (right). The isosurface for $\rho = 1.6$ a.u., $\rho_{\sigma\text{-orbitals}} = 1.6$ a.u. and $\rho_{\pi\text{-orbitals}} = 0.5$ a.u. is displayed in red color.

Electronic structure

In a simple picture based on Hückel calculation [196,197], the electronic ground state structure can be understood as a sp^2 -hybridized carbon system with 3 strongly binding σ orbitals and an additional π -orbital for each carbon atom giving together 180 σ electrons and 60 π electrons. The σ -orbitals are deeper bound than the π -orbitals giving the first 90 levels (180/2 due to the shared orbital for spin-up and spin-down electrons) in the Kohn-Sham energy spectrum calculated in the LDA approach and displayed in Fig. 3.17. The π -orbitals have Kohn-Sham energies above the σ -levels close to the Fermi level. Therefore, they play a more active role in the electron dynamics. The energy width of all occupied energy levels is nearly 20 eV which has been found also in other DFT calculations [165].

The character of the two different types of orbitals can be visualized by the electron density formed from the particular orbitals. In Figure. 3.16 the isosurface of the electron density is displayed for the total density ρ , the density of the σ -orbitals ρ_{σ} and of the π -orbitals ρ_{π} . Obviously, the simple picture of sp^2 -hybridized carbon atoms is supported by the shape of the densities. A clear difference can be found between ρ_{σ} which is mostly located between the atoms, and ρ_{π} which shows a strong π -character normal to the molecular surface. The total density ρ shows more the character of the σ -symmetry since the majority of the electrons occupy σ -orbitals.

In Figure 3.17 also the energy level of the highest occupied molecular orbital (HOMO) is indicated with its symmetry label h_u^{10} . It is fivefold degenerate and is completely filled with 10 electrons (5 spin-up and spin-down electrons). A complete overview of the electronic structure and the symmetry considerations can be found in [165].

The closed-shell electronic configuration, i.e. the singlet electronic groundstate S_0 , allows us to describe the C_{60} molecule with the (restricted) local density approximation (LDA) as mentioned above. Due to this limitation we cannot describe any triplet excited states in the

time-dependent calculations.

3.3.2 Resonant and nonresonant laser excitation

The C_{60} molecule can be excited resonantly or nonresonantly by a laser field. Resonant excitation allows to excite the electronic system much easier with moderate laser intensities. In particular, we are interested in the first electronic resonance whose frequency is also accessible with standard laser techniques. Furthermore, it has been found that the excitation via the first electronic resonance can be seen in general as a bottleneck for photophysical energy deposition into C_{60} , e.g. for the population of high-lying Rydberg states [177].

Electronic spectrum

In the Kohn-Sham spectrum (Fig. 3.17) all energy levels are plotted with energies up to 20 eV for the uppermost unoccupied orbitals. The first dipole allowed transition from the *ungerade* HOMO to the *gerade* LUMO+1 is indicated by an arrow. However, in density functional theory the excitation energies are not simply given by the difference of the Kohn-Sham energies which would give only a crude estimation. One possibility to find the optical spectrum is the excitation of the molecule with a very short laser pulse (δ -pulse) for fixed nuclei. In the NA-QMD calculations the δ -pulse was mimicked by a \sin^2 -pulse with a period of $T = 0.1$ a.u. (see eq. (3.1)). The system was propagated for a time $t = 20000$ a.u. (484 fs). The Fourier transform $\mathbf{d}(\omega)$ of the electronic dipole moment $\mathbf{d}(t) = \sum_{\sigma} \sum_{i=1}^{N_e^{\sigma}} \langle \Psi^{i\sigma} | \mathbf{r} | \Psi^{i\sigma} \rangle$ gives the electronic excitation energy spectrum.

The spectrum is plotted in Fig. 3.17. The weak peak at $\omega = 3.37$ eV is the first excitation energy and is related to the $HOMO \rightarrow LUMO + 1$ transition. The energy of 3.37 eV is somewhat larger than the experimental values of 3 eV [167, 198, 199].

Strong resonances occur at much higher frequencies. It is known that a giant plasmon excitation at 22 eV (surface plasmon) [167] and at 40 eV (volume plasmon) [169] exist. The plasmon excitation can be explained as a collective excitation of the delocalized electron cloud which oscillates relative to the nuclear backbone. In the NA-QMD calculations the spectrum is ambiguous with high peaks between 15 eV and 25 eV whereas no strong resonances near 40 eV can be seen.⁹ For this reason we cannot assign with certainty a specific structure to the first plasmon. However, the absence of strong resonances near the position of the second plasmon (40 eV) is possibly caused by the limitations of the minimal basis set.

⁹Since there is no averaging over vibrational motion, the calculated spectrum is not smeared out like in the experimental results for the plasmon peaks.

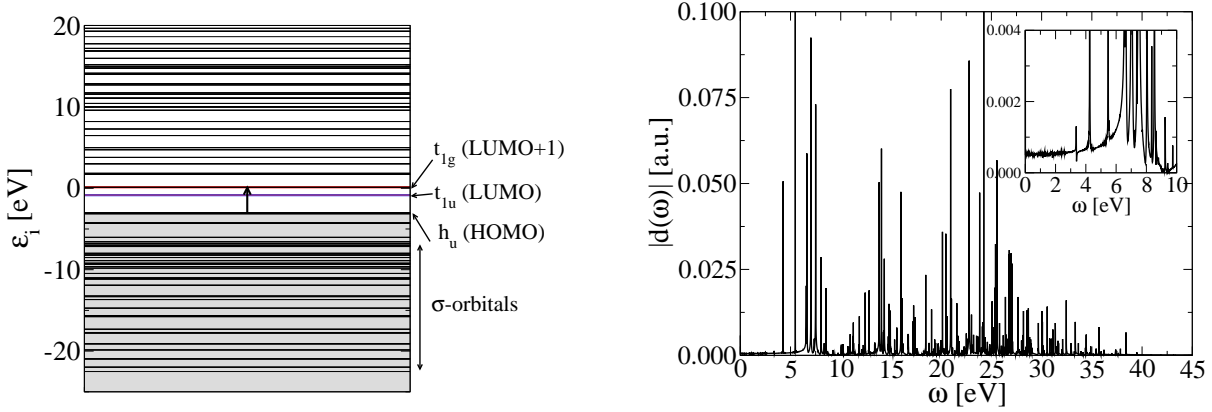


Figure 3.17: (Left) The Kohn-Sham energies ϵ_i of C_{60} for the 120 occupied and the 120 unoccupied orbitals. The HOMO, LUMO and LUMO+1 are labeled. Also the first allowed dipole transition $HOMO \rightarrow LUMO + 1$ is indicated by an arrow. (Right) The electronic spectrum of C_{60} ($|d(\omega)|$). The inset shows the area for small excitation energies ω .

Dependence on laser polarization

The Buckminster Fullerene is highly symmetric which is obvious from the physical properties. Therefore, we have tested the dependence of the absorbed energy on the laser polarization for a resonant and a nonresonant laser frequency. The laser polarization was varied in the xy-plane which is defined on the left side in Fig. 3.18. The nuclei were taken as fixed for the short laser pulse ($T = 5$ fs) since they do not affect the absorption process. With the chosen laser intensities the C_{60} will be highly electronically excited with absorbed energies around 300 eV resp. 150 eV for the nonresonant resp. for the resonant pulse (see right side of Fig. 3.18). As expected, the absorbed energy depends only marginally on the polarization of the laser field with deviations from the mean value of a few percent. Therefore, it is justified to consider only a specific laser polarization without loss of generality. In the following calculations the laser polarization is set to $\vec{E} \parallel C_5$ symmetry-axis which is perpendicular to a pentagonal face of C_{60} and corresponds to an angle $\alpha = \arctan\left(\frac{\sqrt{3-\sqrt{5}}}{\sqrt{2}}\right) \approx 31.7^\circ$ as defined in Fig. 3.18. In that case the icosahedral symmetry I_h is not fully broken in the time-dependent problem, $C_{60} + \text{laser}$, but rather reduced to the C_{5v} -symmetry. This requires a lower computational effort in the time-dependent calculations.

Dependence on laser intensity

The energy deposition due to a laser pulse depends strongly on the laser intensity. On the left side of Fig. 3.19 the absorbed energy as a function of the laser intensity is plotted for a resonant (370 nm) and a nonresonant (800 nm) laser with a pulse length of $T = 27$ fs. The absorption process is of electronic nature although for the nonresonant laser

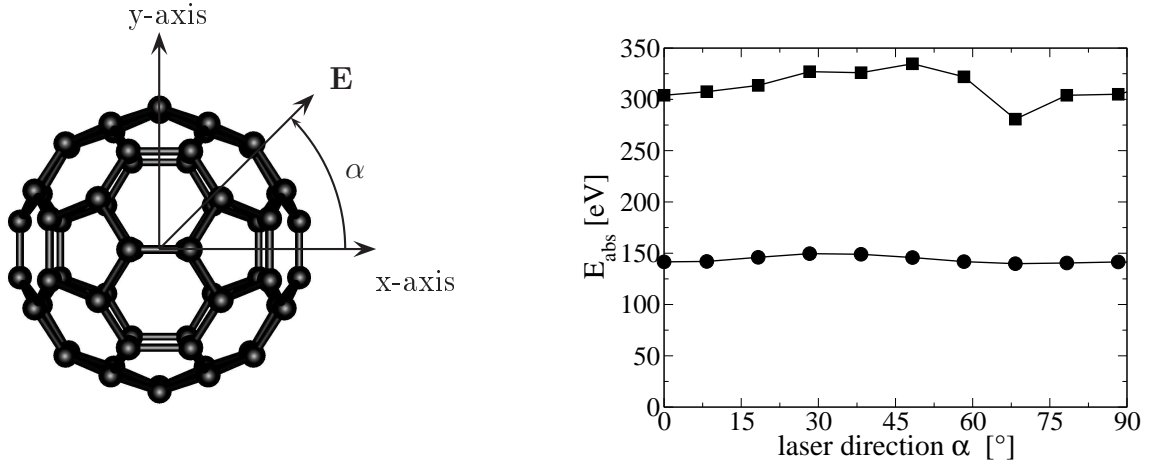


Figure 3.18: (Left) The definition of the orientation angle α in the x-y plane. The x-axis ($\alpha = 0$) as well as the y-axis ($\alpha = 90^\circ$) corresponds to a C_2 -symmetry axis of the C_{60} cage. (Right) The absorbed energy after exciting the C_{60} molecule as a function of the orientation angle α for a resonant laser ($\omega = 3.37$ eV, $T = 5$ fs, $1.6 \cdot 10^{14} \frac{\text{W}}{\text{cm}^2}$) (●) and a nonresonant laser ($\omega = 1.5$ eV, $T = 5$ fs, $1.6 \cdot 10^{15} \frac{\text{W}}{\text{cm}^2}$) (■).

frequency, high absorption energies up to several hundreds eV occur. The response for the nonresonant excitation is an order of magnitude smaller than for the resonant case. However, in both cases the energy absorption increases nonlinearly with increasing laser intensity. Additionally, we find some oscillations at an intensity of $2.8 \cdot 10^{13} \frac{\text{W}}{\text{cm}^2}$ (resonant) resp. $5.8 \cdot 10^{14} \frac{\text{W}}{\text{cm}^2}$ (nonresonant). In the time domain we see a deexcitation process. However, it is not clear if the increase of the absorbed energy is an artefact of our calculations due to the limited basis.

On the right side of Fig. 3.19 the number of excited electrons N_{exc} is displayed. As one can see, the laser excitation is a multielectron phenomenon for large laser intensities and cannot be described with a single electron model. We find up to 40 excited electrons for the largest laser intensities. The number of excited electrons correlates well with the absorbed energy.

3.3.3 Laser excited breathing mode

In the following, the response of the C_{60} molecule to the laser excitation will be investigated including the vibrational motion. The electronically stored energy is transferred via electronic-vibrational coupling to the different vibrational normal modes.

The C_{60} molecule has 174 vibrational normal modes (inner degrees of freedom: $3 \cdot 60$ minus 6 (translation+rotation)). How to calculate the eigenmodes and eigenfrequencies is explained in Appendix B.1. A variety of normal modes with different symmetries exist with vibrational periods in the range from 20 fs (with more tangential nuclear displacements) up to 120 fs (with radial motion) (see section B.2). The fully symmetric breathing mode $A_g(1)$ with a period of 64 fs (exp.: 67 fs) lies in between. A selection of the eigenmodes is depicted

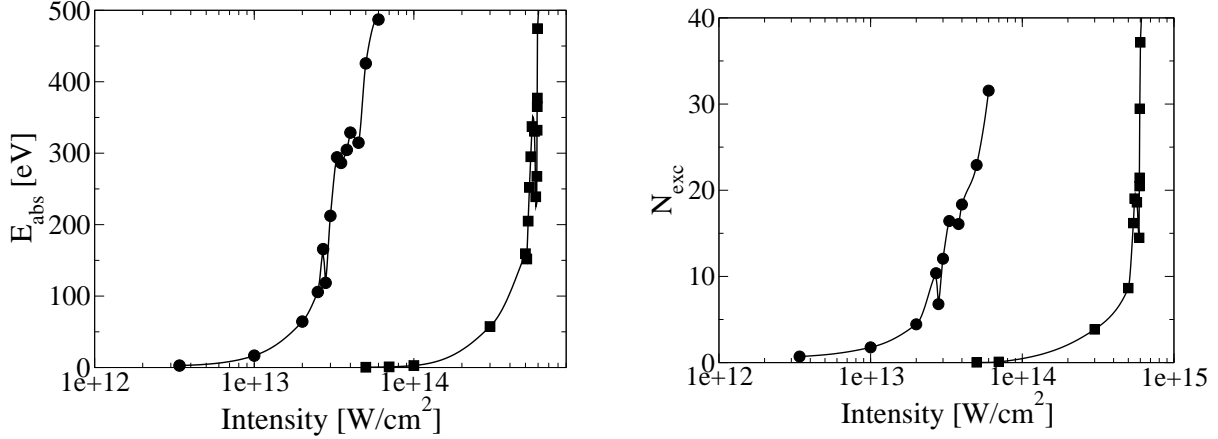


Figure 3.19: The absorbed energy (left) and the number of excited electrons N_{exc} (right) as a function of the laser intensity for resonant (●) and nonresonant (■) laser excitation ($T = 27$ fs).

in Fig. B.2.

In the dynamical calculations the normal mode eigenvectors will be used to decompose the kinetic energy (see appendix B.1):

$$E_{vib} = \sum_{mode=1}^{174} E_{vib}^{mode} \quad (3.6)$$

making it possible to observe the vibrational excitation of each mode E_{vib}^{mode} ¹⁰.

For small laser intensities $3.3 \cdot 10^{10} - 3.3 \cdot 10^{12} \frac{\text{W}}{\text{cm}^2}$ Zhang and coworkers [187, 188, 200], using a tight-binding model, have found that different vibrational modes will be excited depending on the laser parameters. In particular, depending on the laser length T , the modes with H_g -symmetry ($T > 40$ fs) and the breathing mode $A_g(1)$ respectively the pentagonal pinching mode $A_g(2)$ ($T < 40$ fs) dominate the vibrational motion explaining discrepancies in experiments [171, 201, 202].

For much higher laser intensities resp. absorbed energies, i.e. in the multielectron excitation regime, we find a different picture. In this case the breathing mode $A_g(1)$ dominates. This is consistent with the tight-binding calculations for a nonresonant laser with $T = 12$ fs, $\omega = 2$ eV and $I \geq 2.1 \cdot 10^{12} \frac{\text{W}}{\text{cm}^2}$ [187].

An example of the dynamics of C_{60} is shown in Fig. 3.20 left side for a resonant 27 fs-laser ($\omega = 3.37$ eV, $I = 3.3 \cdot 10^{13} \frac{\text{W}}{\text{cm}^2}$). For the first 54 fs, while the laser is switched on, the molecule absorbs nearly 300 eV (upper part). The almost homogeneously distributed excited electron cloud couples to the radially symmetric $A_g(1)$ breathing mode (lower part). On a time scale of femtoseconds the radial motion will be strongly excited. Nearly all vibrational kinetic energy is stored in the breathing mode. For a time of 240 fs no damping of the radial

¹⁰The potential energy cannot be used due to the anharmonic deformation.

oscillation is taking place. This shows that the coupling between the $A_g(1)$ mode and other modes takes place at longer time scales, in the range of picoseconds¹¹. Furthermore, we find that the period of the radial oscillation is larger than the ground state period $T_{A_g(1)} = 64$ fs (Fig. 3.20 right side).

In general, by increasing the laser intensity, and therefore the absorbed energy, the breathing mode period $T_{A_g(1)}$ grows as well (Fig. 3.21). The explanation is that due to the electronic excitation the potential has been changed towards much weaker carbon-carbon bonds than in the electronic ground state. This, in turn, enlarges the equilibrium radius R_{eq} and the breathing mode period $T_{A_g(1)}$. The effect is only significant for high absorption energies in the range of few tens eV or more. At the highest laser intensity (5×10^{13} W/cm²) more than 30 valence electrons are strongly excited resulting in an impulsive force that expands the molecule dramatically up to $R = 8.9$ a.u. which is 130% of the C₆₀ radius, orders of magnitude larger than expected for any standard harmonic oscillation.

The dominant excitation of the breathing mode can also be found for smaller laser durations, e.g. for $T = 9$ fs, if the laser intensity is high enough to excite the molecule strongly. The statement also holds in the case of nonresonant laser excitation ($\omega = 800$ nm) but much stronger laser intensities are needed to excite the molecule significantly (see Fig. 3.19).

The dynamics of the electronic system can also be visualized, which is shown in Fig. A.6 (Appendix A.2). In the figure, snapshots of the electron dynamics are displayed using the electron localization function (ELF) as well as the electron density. Comparing the bond structure before and after the laser excitation we find a significant change for the ELF which indicates bond breaking, especially of the double bonds. Looking at the electron density we see that the density between the nuclei will be decreased, supporting the idea of the bond weakening. The change in the bond structure is distributed over the whole cage which is in agreement with the observed excitation of the symmetric breathing mode.

3.3.4 Pump-probe scenario

In summary, two interesting points have been found in our calculations:

- By exciting C₆₀ with strong femtosecond laser pulses, multielectron excitation takes place with absorbed energies up to 300 eV depending on the laser intensity. Due to the multielectron excitation and subsequent electron-vibration coupling, the breathing mode $A_g(1)$ will be excited with large amplitudes.
- The period of the excited breathing mode depends strongly on the amount of absorbed energy respectively the laser intensity. For higher excitation energies the period increases significantly.

¹¹In the td-DFT scheme calculations in the range of picoseconds are beyond our computational capacity.

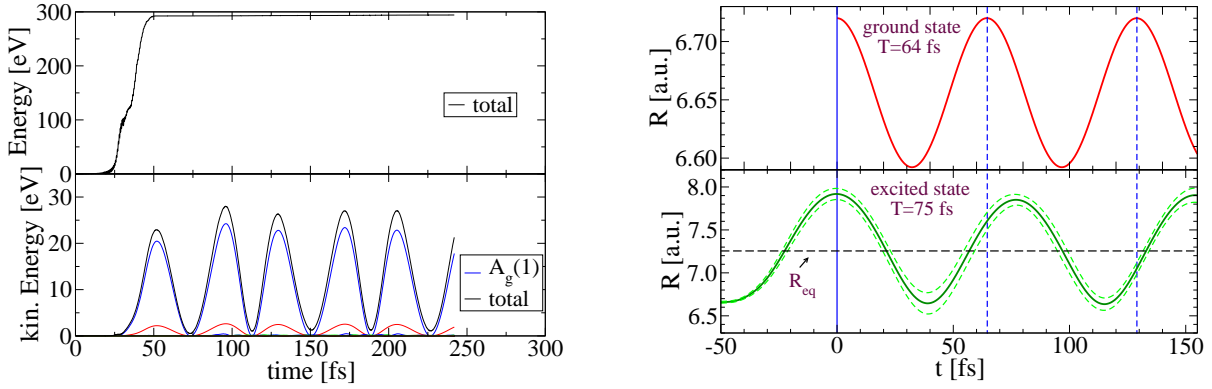


Figure 3.20: (Left) The absorbed energy (top) and the vibrational kinetic energy of the vibrational normal modes (down) as a function of time. (Right) The radial oscillation of C_{60} in the electronic ground state (top) and for a laser excited molecule. The laser starts at time $t = -50$ fs ($\omega = 3.37$ eV, $T = 27$ fs, $I = 3.3 \cdot 10^{13} \frac{\text{W}}{\text{cm}^2}$). The dashed lines indicate the standard deviation environment around the mean radius R (solid line).

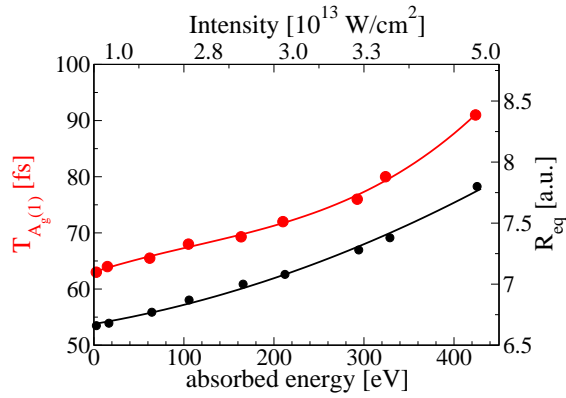


Figure 3.21: Resonant laser excitation of C_{60} ($\omega = 3.37$ eV, $T = 27$ fs) with different laser intensities. The period of the breathing mode $T_{A_g(1)}$ (red) and the equilibrium radius R_{eq} (black) as a function of the absorbed energy (lower axis) resp. the laser intensity (upper axis).

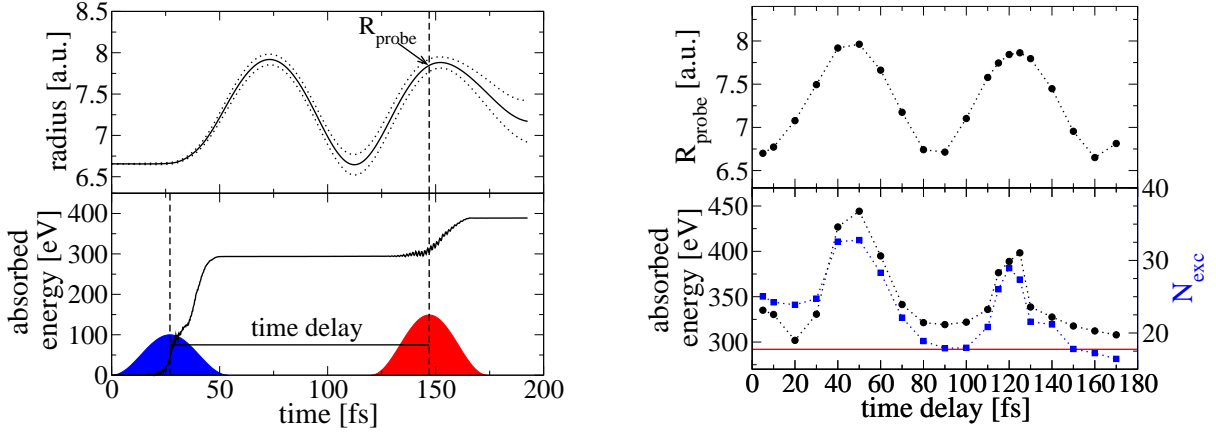


Figure 3.22: Pump-probe scenario with with a blue pump pulse ($\omega = 3.37$ eV, $T = 27$ fs, $I = 3.3 \cdot 10^{13} \frac{\text{W}}{\text{cm}^2}$) and a red probe pulse ($\omega = 1.5$ eV, $T = 27$ fs, $I = 7.3 \cdot 10^{13} \frac{\text{W}}{\text{cm}^2}$). (Left) The radius R (top) and the absorbed energy (down) as a function of time for a pump-probe scenario with a time delay of 120 fs. The dotted lines are defined in the same manner as in Fig. 3.20. (Right) (top) C_{60} radius at the maximum of the probe pulse R_{probe} as a function of the delay time. (down) Absorbed energy (circles) and number of excited electrons (squares) of C_{60} after excitation with the pump and probe pulse as a function of the time delay. The horizontal line indicates the absorbed energy after the pump pulse alone (292 eV).

In a next step the response of a highly excited molecule to a second laser pulse will be investigated.

Femtosecond pump-probe experiments are a well known tool to examine vibrational motion in molecular systems. In particular, the technique was successfully applied to the dynamics of diatomic molecules [203] where it is possible to follow the only relevant nuclear degree of freedom, the internal distance. A similar situation occurs in the laser excitation of the C_{60} molecule where the electronic excitation induces primarily a one-dimensional motion of the radius.

Using a resonant pump pulse as shown above ($\omega = 3.37$ eV, $T = 27$ fs, $I = 3.3 \cdot 10^{13} \frac{\text{W}}{\text{cm}^2}$) the induced breathing mode will be probed by a second nonresonant laser pulse ($\omega = 1.5$ eV, $T = 27$ fs, $I = 7.3 \cdot 10^{13} \frac{\text{W}}{\text{cm}^2}$) for different time delays between the pump and probe pulse. Due to the pump pulse an energy of nearly 290 eV will be absorbed, and the radius of the molecule starts to oscillate with a period of 75 fs and a large amplitude ($R_{max} = 7.9$ a.u.). As one can see in Fig. 3.19 the nonresonant probe pulse is very weak, and cannot excite the C_{60} molecule, initially in the electronic ground state, significantly. However, the situation is changed in the pump-probe scenario.

On the left side of Fig. 3.22 the dynamics is plotted for a time delay of 120 fs. The time delay is defined as the time between the maxima of the pump and the probe pulse, and the actual radius R_{probe} as the radius at the time of the maximum of the probe pulse. The maximum

of the probe pulse coincides in time with a maximum of the radius R , where an additional amount of energy is absorbed (~ 100 eV). Probing the molecule also for other time delays we find that the total absorbed energy after the probe pulse is strongly correlated with the actual radius of the "breathing" molecule (Fig. 3.22), i.e. with large amplitude oscillations of the $A_g(1)$ mode. The additional energy absorption due to the probe pulse is significant and lies between zero for the minimal radius and nearly 150 eV for the maximal radius. For the opposite case (not shown in here), i.e. negative time delays (at first the nonresonant red pump pulse and then the resonant blue probe pulse), no oscillation of the absorbed energy can be found due to the fact that the nonresonant pump pulse is too weak to excite the breathing mode.

For the photoabsorption as a function of the time delays a signature in the signals of the fragmentation products should be found. The relaxation of the highly excited C_{60} molecules leads to a thermally hot molecule. The subsequent evaporation of C_2 fragments is a statistical process on a μs to ms timescale which cannot be investigated within the NA-QMD approach.

However, the theoretical observations have been confirmed in two-colour pump-probe studies [53]. The experiments show a periodicity of 80 fs in the ion signal of the C_{60} fragmentation products as a function of the time delay. The experiments were performed with similar laser parameters using a resonant 400 nm pump pulse ($T = 25$ fs, $I = 1.7 \cdot 10^{13} \frac{W}{cm^2}$) and a nonresonant 800 nm probe pulse ($T = 27$ fs, $7.3 \times 10^{13} W/cm^2$). The pump pulse differs somewhat from the laser used in the calculation due to the fact that the experimentally obtained first optical resonance at a wavelength of 400 nm does not match exactly the theoretical value of 370 nm within the LDA-approximation.

Figure 3.23 (b) shows the metastable C_{48}^{3+} ion signal as a function of the time-delay between the 400 nm pump and the 800 nm probe-pulse. C_{48}^{3+} is most abundant and metastable fragmentation (on a μs -ms timescale) is a particularly sensitive probe of the equilibrated absorbed energy (temperature) of C_{60}^{q+} generated in the initial photoabsorption process [176]¹². At negative time delays, when the red pulse leads, almost no signal from C_{48}^{3+} is observed. Once pump and probe pulse overlap, the ion yield increases strongly and a maximum fragment signal is found at a delay of $\simeq 50$ fs. Closer inspection of the pump-probe transient reveals a weak modulation on top of the C_{48}^{3+} ion signal. By fitting a pulse width convoluted single exponential decay to the ion signal and subtracting it from the measured signal this modulation - albeit small - is found in all pump-probe data from multiply charged large fragments with a periodicity of 80 ± 6 fs. This is shown in Fig. 3.23 (b) and can be understood due to the NA-QMD calculations¹³.

¹²As mentioned before, the relaxation process takes place on a timescale of picoseconds or longer, and cannot be considered in the NA-QMD calculations.

¹³The exponential decay of the probe signal (excitation energy) cannot be seen in the LDA calculations on the same time scale may be due to the lack of electron-electron correlation effects

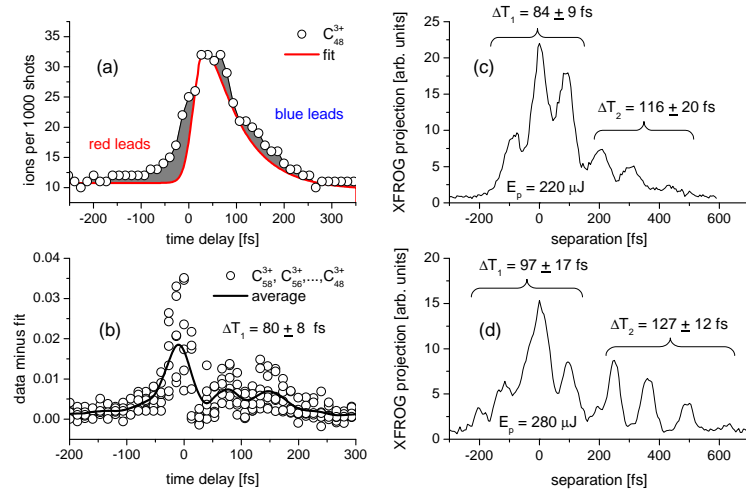


Figure 3.23: Pump-probe (left) and optimal control (right) experiment (taken from ref. [53]). (a) Metastable C_{48}^{3+} ion signal as a function of time delay between blue pump and red probe pulse. An exponential decay is fitted to the data. (b) A modulation is found for all large fragments C_{60-2m}^{3+} by subtracting the fits from the measured transients. (c) Optimized temporal shape with 220 μJ laser pulses and (d) 280 μJ pulses.

Besides the pump-probe experiments, additional, optimal control experiments have been performed. The optimized pulse shapes also show periodic behaviour (Fig. 3.23 (c),(d)) which may be explained by vibrational excitation. However, the periodicity lies in the range of 84 till 127 fs. The value of 84 fs is consistent with the breathing mode of a highly excited C_{60} molecule (see Fig. 3.21), but the maximal value of 127 fs is not reproduced by the theory, possibly due to the lack of ionization, since the breathing mode period of ionized C_{60} is increased in comparison with the neutral molecule.

4 Collision-induced fullerene dynamics

The collision dynamics of C_{60} and other fullerenes with ions or fullerenes has been investigated since the nineties of the last century [204]. Depending on the impact energy different competing reaction channels occur: scattering, fusion, (multi-)fragmentation [205], charge transfer [205, 206] and ionization [207, 208]. In the high energy regime (multi-)fragmentation [104, 105] is the dominant reaction, whereas for impact energies of 60 eV-500 eV (center of mass) fusion resp. inelastic scattering takes place in $C_{60} + C_{60}$ collisions [209, 210]. Considerable efforts were made to obtain the fusion cross section and especially the fusion threshold [210, 211]. For impact energies below the fusion threshold inelastic scattering is the only reaction channel.

To investigate the collision dynamics theoretically, classical molecular dynamics simulations [212] as well as QMD simulations have been performed [103, 105, 209].

In this chapter the NA-QMD approach will be applied to the dynamics of fullerene+fullerene collisions. In the first part the low energy limit (impact energies $E_{\text{cm}} < 150$ eV) will be reinvestigated in particular in the context of the normal mode analysis. We will find that in particular the oblate-prolate mode $H_g(1)$ dominates the collision dynamics. A simple 2-dimensional model will be introduced which allows us to understand the reaction processes which occur in this energy regime, i.e. fusion and inelastic scattering.

In the second part the dynamics of high-energy fullerene-fullerene collisions ($E_{\text{cm}} \sim$ keV-MeV) is shown. In this impact energy range a competition between electronic and vibrational excitation occurs which leads to different fragmentation regimes. The results will be discussed with respect to ion-fullerene collisions, which have been investigated in the past [32].

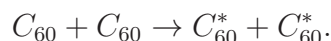
4.1 Adiabatic dynamics

Several years ago, fullerene-fullerene collisions at impact energies around 100 eV have been studied in detail experimentally [209, 213] as well as theoretically [103]. The results of these extensive studies can be summarized as follows (for a review see e.g. [94]):

- i) There are two reaction channels which do occur in this range of impact energies, namely, complete fusion



and deep inelastic scattering



Fragmentation into three or more fragments does not occur¹.

- ii) Fusion occurs only above a certain impact threshold energy, the fusion barrier V_B . For all target-projectile fullerene-fullerene combinations with C_{60} and C_{70} , the fusion barriers are surprisingly large ($V_B \approx 60 - 80$ eV) [209] as compared to a typical bond energy (≈ 10 eV) in the system.
- iii) The absolute values of the fusion cross sections as function of the bombarding energy are orders of magnitude smaller as compared to the geometrical cross section [213], which is rather unusual for fusion of complex systems like nuclei, droplets or clusters [214].

Although microscopic QMD calculations do reproduce all experimental details [94, 103], there is up to now, no physical explanation of the underlying mechanism leading to the unexpected and surprising observations summarized above. So, the simple questions, why only two reaction channels do occur, why large fusion barriers and small fusion cross sections are observed, represent a long-standing fundamental problem in the field.

We reanalyze the reaction mechanism of $C_{60}+C_{60}$ collision with special emphasis on the normal mode analysis which has not been performed in our earlier studies [94].

4.1.1 $C_{60} + C_{60}$: Fusion versus scattering

Initial conditions

The initial state will be characterized by the impact parameter b and the impact energy (in the center of mass system)

$$E_{\text{cm}} = \frac{\mu}{2}v^2$$

with the relative mass of both fullerenes $\mu = \frac{M_1 M_2}{M_1 + M_2}$ ($M_{1/2}$: masses of the fullerenes) and the relative initial velocity v (see Fig. 4.1).

In particular, we have only performed calculations for direct collisions ($b = 0$) for the purpose of simplicity. The reaction channel is very sensitive to the geometrical orientation of the two buckyballs which can be varied by rotating each C_{60} .

The initial distance R between the centers of masses of each cluster ² has been chosen to be 20 a.u. which is necessary to ensure two initially "isolated" molecules in the electronic ground state.

¹We do not consider secondary evaporation processes (of mainly dimers) which proceed on time scales of μs [213].

²In the following, the variable R denotes always the distance between the clusters, and not the C_{60} radius.

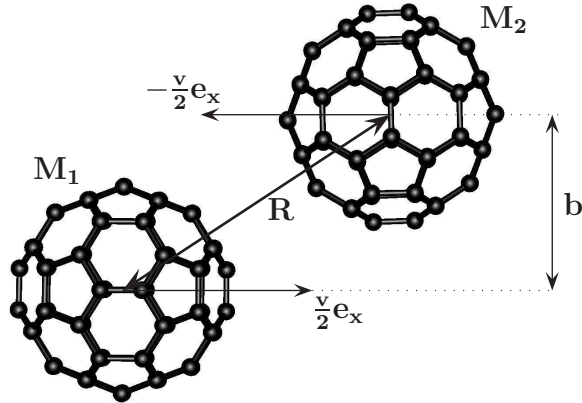


Figure 4.1: The initial geometry of a $C_{60} + C_{60}$ collision with the impact parameter b , the distance R between both molecules, and the impact velocity v parallel to the x -axis. The total mass of each C_{60} is given by $M_{1/2} = 60 \cdot m_C = 1321920$ a.u.

Reaction channels

We have investigated the $C_{60} + C_{60}$ collision for three impact energies: 40, 60 and 104 eV. For each of these, different initial conditions have been considered by varying the initial orientation of the buckyballs randomly for 17 events. In Figure 4.2 the typical reactions of the two competing channels, fusion and inelastic scattering, are displayed for an initial impact energy of 104 eV.

The typical fusion product is a vibrationally highly excited peanut-shaped C_{120} molecule [215, 216] which is expected to have relatively low binding energies of a few eV [217]. It may relax to form a more strongly bound and compact isomer with the form of a "cigar" or "sphere" [217] on a timescale of picoseconds, if no thermal evaporation of single C_2 units takes place.

In the case of inelastic scattering the two buckyball system decays into two highly excited and deformed products which may also evaporate C_2 dimers on a longer timescale.

In Figure 4.3 the distance R , the kinetic energy of the projectiles

$$E_{\text{cm}} = \frac{\mu}{2} \dot{R}^2 \quad (4.1)$$

and the total vibrational (kinetic) energy E_{vib} (see Eq. (3.6)) of both molecules are displayed for the different initial orientations. As one can see from the distance and the kinetic energy, the most events are inelastic scattering processes. The point of closest approach is reached at a time near 100 fs, where the deformation is maximal (see Fig. 4.2). For the impact energies of 40 and 60 eV no fusion events occur, and only at an impact energy of 104 eV

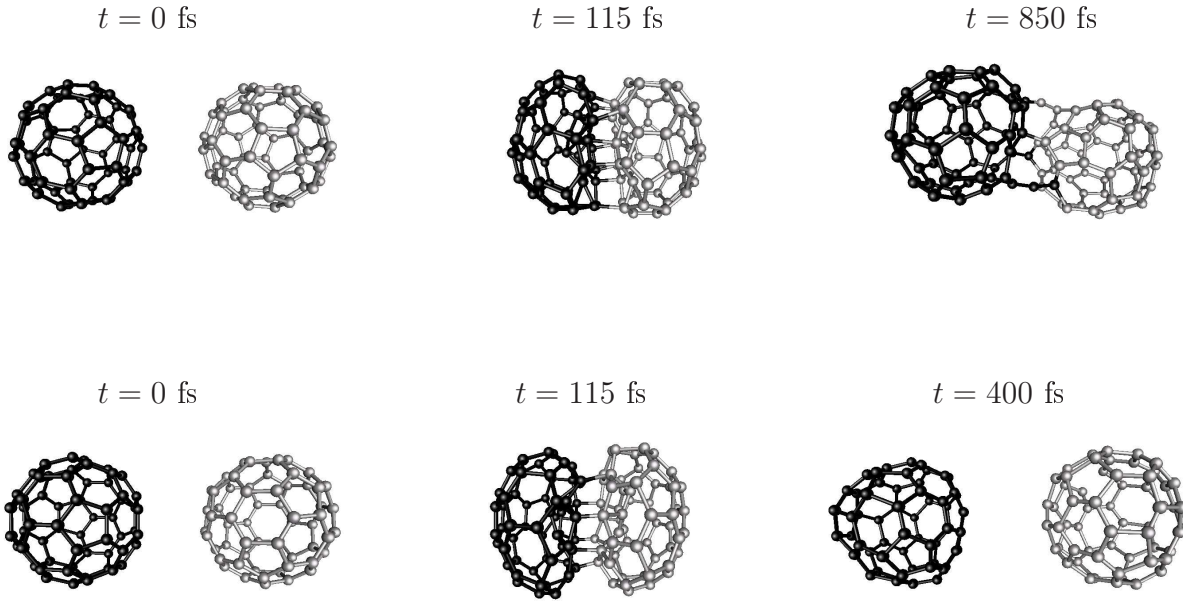


Figure 4.2: Reaction channels of C₆₀+C₆₀ collisions at an impact energy of 104 eV. Snapshots of a fusion event (top) and an inelastic scattering event (down).

fusion events can be found in agreement with former QMD results which show a fusion barrier of 80 eV [213].

The vibrational energy E_{vib} shows a characteristic structure during the collision reaction. At the beginning of the entrance channel a strong enhancement of the vibrational motion can be seen due to the deformation process. At the point of closest approach a minimum can be found which is caused by the storage of vibrational (kinetic) energy into deformation energy. In the exit channel the repulsion leads to a further dissipation of energy into the vibrational modes with a maximum final vibrational energy per atom of more than 0.3 eV which corresponds to a temperature of more than 2500 K for the vibrationally relaxed system.

In the exit channel the final relative kinetic energy after the collision differs for the various initial orientations. However, by averaging over the inelastic scattering events we find that the averaged relative kinetic energy of the scattered fullerenes is nearly independent on the c.m. bombarding energy $E_{c.m.}$ (see Fig. 4.4). Therefore, the total amount of dissipated energy $E_d(\infty)$ into all vibrational modes after the collision is simply given by

$$E_d(\infty) = E_{c.m.} - \Delta E \quad (4.2)$$

with $\Delta E \approx 17$ eV.

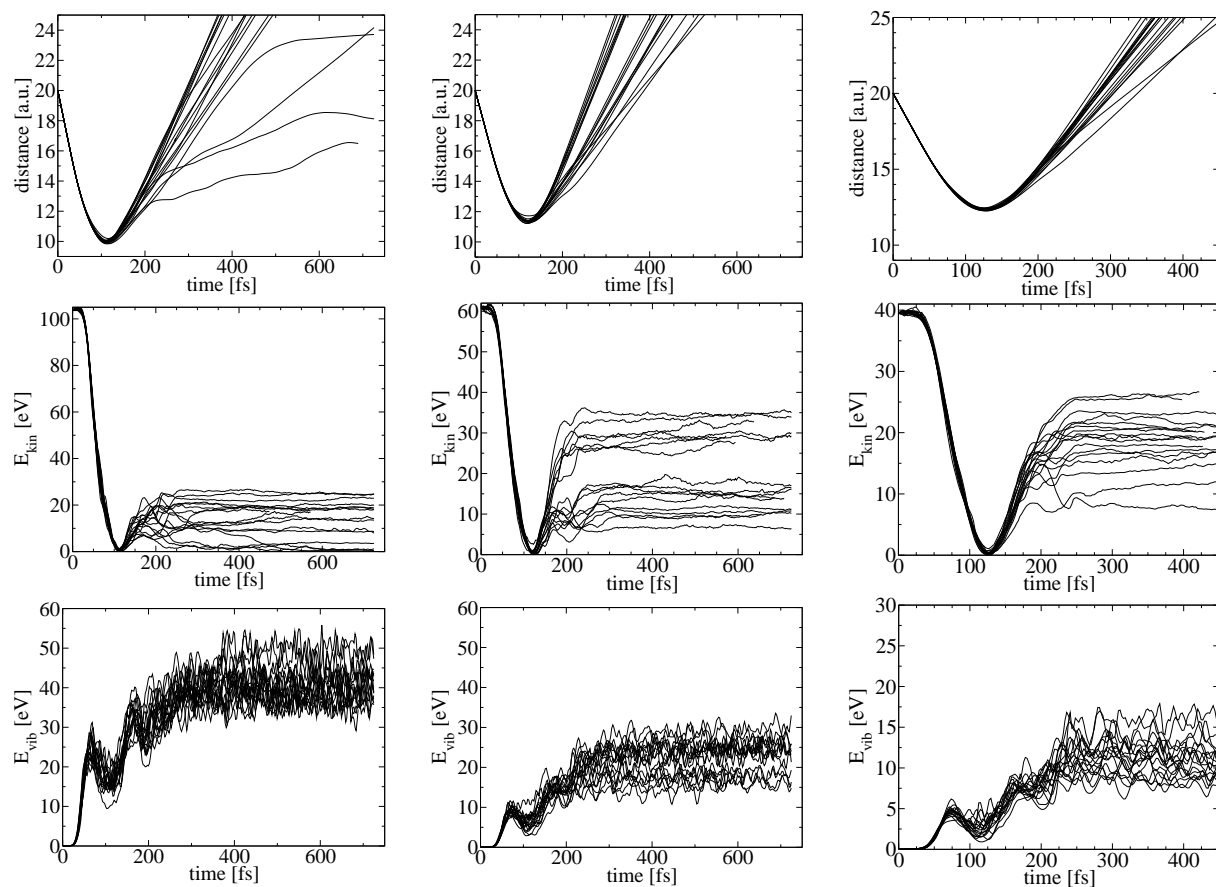


Figure 4.3: Collision dynamics for an impact energy of 104 eV (left), 60 eV (middle) and 40 eV (right) for $T=0$ K. The C_{60} - C_{60} distance R (top), the kinetic energy E_{kin} (middle) and the total vibrational energy E_{vib} (bottom) are displayed as a function of time for the different collision events.

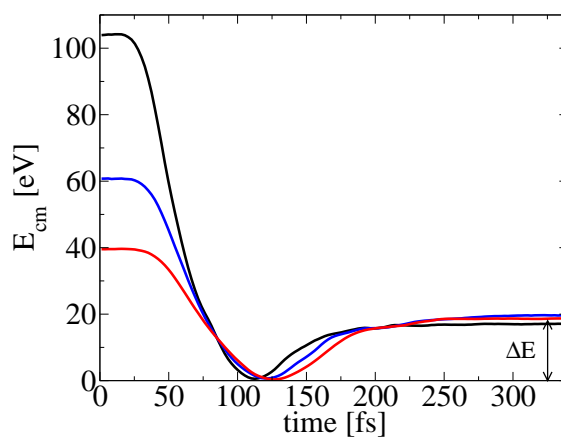


Figure 4.4: The kinetic energy E_{kin} averaged over the initial orientations for the impact energies of 104 eV, 60 eV and 40 eV as a function of time. The final energy release ΔE is indicated.

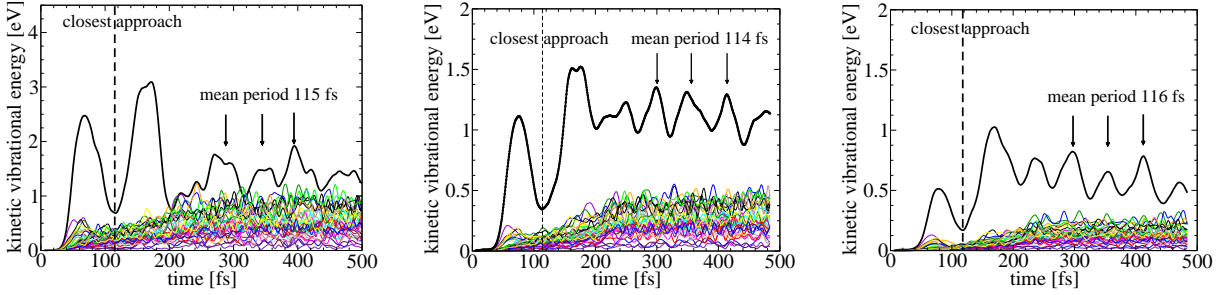


Figure 4.5: Normal mode analysis of $C_{60} + C_{60}$ collision for an impact energy of 104 eV (left), 60 eV (middle) and 40 eV (right). The vibrational energy of all 174 vibrational normal modes as a function of time. The oblate-prolate mode $H_g(1)$ is indicated by the black (thick) line.

The normal mode analysis - The oblate-prolate mode $H_g(1)$

To gain an insight into the vibrational dynamics of the collision a normal mode analysis will be performed. Therefore, the vibrational energy E_{vib} of each C_{60} fullerene will be decomposed using the eigenvectors of the vibrational normal modes (see appendix B.1). In Figure 4.5 the vibrational energy of the normal modes of both C_{60} molecules is plotted as a function of time for all three impact energies. Due to the fact that the results for single collision events are very similar, we show only the result averaged over all events leading to inelastic scattering. The normal mode analysis shows the following features: In the entrance channel, i.e. during the approach phase, the $H_g(1)$ mode (sum over all five degenerated eigenmodes) dominates the internal vibrational excitation mechanism. At the distance of closest approach, the dominant part of the bombarding energy is stored into potential (or deformation) energy of the vibrational modes (see distinct minimum of the kinetic vibrational energies E_{vib}^{mode} at $t \approx 120$ fs). Obviously, the largest contribution to this deformation energy originates from the prolate-oblate mode. This dominant excitation of the prolate-oblate $H_g(1)$ mode is observed for all relative initial orientations of the fullerenes, all impact energies ($E_{c.m.} \approx 40 \dots 150$ eV) and all relevant impact parameters. The long time behaviour shows that due to vibrational relaxation, more and more of the 174 normal modes do contribute.

Obviously, the dominant excitation of the quadrupole mode during the approach phase represents the key point in the understanding of the basic reaction mechanisms of these collisions. On the one hand, it prevents fragmentation into three or more channels due to its symmetry which avoids any shearing forces. On the other hand, it acts as doorway state for fusion. In an idealized picture, the energy stored into this mode at the distance of closest approach must exceed a critical value of about $\Delta E \approx 17$ eV. This implies that fusion can occur only at impact energies considerably larger than ΔE which explains the large fusion barriers V_B . In the vicinity of $E_{c.m.} \geq V_B$, this critical amount of energy can only be stored into the $H_g(1)$ mode if their five (degenerated) principle axes coincide with

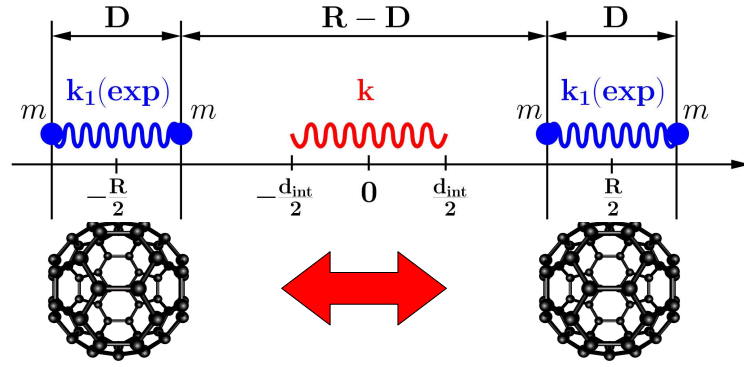


Figure 4.6: Sketch of the two-spring model for the C_{60} - C_{60} collision.

the collision axis. Because this is realized only very rarely, the absolute cross sections for fusion are much smaller than the geometrical cross section.

4.1.2 A two-dimensional classical trajectory model

The simplicity of the single oblate-prolate mode excitation together with the microscopic findings (see above) allows for the formulation of a simple two-dimensional and *analytical* trajectory model of fullerene-fullerene collisions ("spring-model") which describes *quantitatively* the basic features predicted by the fully microscopic, 360-dimensional QMD calculations.³

A sketch of the model is given in Fig. 4.6 and consists of two interacting springs. Each spring $i = 1, 2$, which represents one molecule, is defined by the two coupled masses $\frac{M_i}{2}$ (M_i : here mass of C_{60}), the force constant k_i (here from the $H_g(1)$ mode) and the equilibrium distance D_i^0 (here diameter of C_{60}). Introducing the c.m. distance between the two reaction partners R and the spring coordinates D_1, D_2 the Hamilton function has the following form (with the relative masses $\mu = \frac{M_1 M_2}{M_1 + M_2}$, $\mu_i = \frac{M_i}{4}$):

$$H = \frac{P_R^2}{2\mu} + \sum_{i=1,2} \left\{ \frac{p_{D_i}^2}{2\mu_i} + V_i(D_i) \right\} + U\left(R - \frac{1}{2}(D_1 + D_2)\right) \quad (4.3)$$

with the potential $V_i(D_i)$ for the inner (vibrational) mode of spring i

$$V_i(D_i) = \frac{k_i}{2}(D_i - D_i^0)^2 \quad (4.4)$$

and an external interaction potential U which depends on the 'contact distance' between the two springs $x = R - \frac{1}{2}(D_1 + D_2)$.

³This mode dominates the vibration of C_{60} during the collision also in collisions with impact parameters $b > 0$.

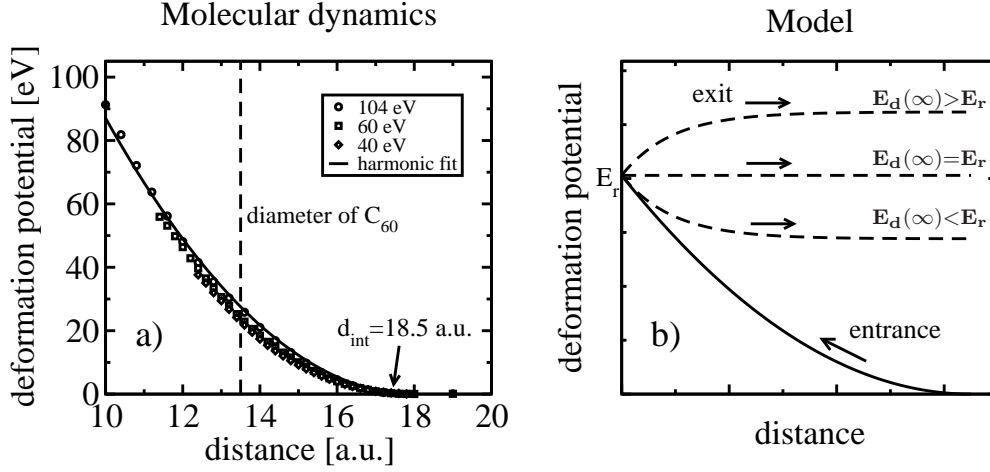


Figure 4.7: a) The deformation potential of the C₆₀ + C₆₀ collision for three impact energies and the averaged harmonic fit for the entrance channel. b) Sketch of the interaction potential U as a function of the distance in the model for the entrance and exit channel for the case of inelastic scattering and fusion.

The potential U mimics the response of all other vibrational degrees of freedom of the molecules. The Newton equations are determined using the Hamilton equations with (4.3):

$$\mu \ddot{R} = - \left. \frac{\partial U(x)}{\partial x} \right|_{x=R-\frac{1}{2}(D_1+D_2)} \quad (4.5)$$

$$\mu_i \ddot{D}_i = - \frac{\partial V_i}{\partial D_i} + \frac{1}{2} \left. \frac{\partial U(x)}{\partial x} \right|_{x=R-\frac{1}{2}(D_1+D_2)} \quad (4.6)$$

In the following we consider only the case of identical springs, suited to the C₆₀ + C₆₀ collision. The number of variables is reduced to

$$D_1 = D_2 \equiv D$$

$$k_1 = k_2$$

$$\mu_1 = \mu_2.$$

Then the simplified Newton equations are given by ($V_i \rightarrow V$):

$$\mu \ddot{R} = - \left. \frac{\partial U(x)}{\partial x} \right|_{x=R-D} \quad (4.7)$$

$$\mu_1 \ddot{D} = - \frac{\partial V}{\partial D} + \frac{1}{2} \left. \frac{\partial U(x)}{\partial x} \right|_{x=R-D}. \quad (4.8)$$

Entrance channel ($\dot{\mathbf{R}} < \mathbf{0}$)

In the entrance channel the interaction potential U can also be written as a harmonic potential:

$$U(x) = \frac{k}{2}(x - d_{int})^2 \theta(d_{int} - x), \quad (4.9)$$

where the interaction distance d_{int} and the force constant k is determined by the averaged microscopic $C_{60} + C_{60}$ calculations. In Fig. 4.7a the result is plotted for all three impact energies which show the harmonic behaviour of the potential. The deformation potential is equivalent to the potential energy difference between the initial and the final geometrical configuration.

A nice property is that the harmonic potential allows to solve the equations of motion (4.8) analytically.

Exit channel ($\dot{\mathbf{R}} > \mathbf{0}$)

So far, no dissipative forces are included, which would prevent fusion events due to the repulsive character of the interaction potential U (see Eq. (4.9)). To describe the energy dissipation which leads to the inelastic behaviour resp. fusion, a method will be used which has been developed in nuclear physics, in particular for deeply inelastic heavy-ion collisions [218]. To do so, an additional deformation potential $E_d(x)$ will be introduced in the exit channel

$$U(x) \rightarrow W(x) = U(x) + E_d(x)$$

with

$$E_d(x) = \begin{cases} (E_r - E_d(\infty))e^{-\frac{x-x_{ret}}{\Delta}} + E_d(\infty) - U(x) & \text{for } x > x_{ret} \\ 0 & \text{for } x < x_{ret} \end{cases}$$

The potential $E_d(x)$ depends on the returning point $x_{ret} = x(t_r)$ and on the potential energy at the returning point

$$E_r \equiv U(x_{ret}) \text{ with } \dot{R}(t_r) = 0. \quad (4.10)$$

The final deformation energy $E_d(\infty) = \lim_{x \rightarrow \infty} E_d(x)$ after the collision is the only free parameter, which determines the reaction process (see Fig. 4.7b):

1. For $E_d(\infty) < E_r$ the potential W is repulsive implying *inelastic scattering*.
2. For $E_d(\infty) > E_r$ the potential becomes attractive which may lead to *fusion*.

In the next part these relations will be used to find an analytical formula for the fusion barrier.

The width $\Delta = \left| \frac{x_{ret} - d_{int}}{2} \left(1 - \frac{E_d(\infty)}{E_r} \right) \right|$ is fully determined by the other parameters and chosen in such a way, that the force at the returning point $-\frac{\partial W}{\partial x} \Big|_{x=x_{ret}}$ is continuous for scattering ($E_d(\infty) < E_r$) respectively changes sign for $E_d(\infty) > E_r$.

Analytical solution for the fusion barrier V_B

In general the EOM's of the model system cannot be solved analytically because of the complicated form of the dissipation potential $E_d(x)$ in the exit channel. However, the dynamics of the system for the entrance channel can be calculated analytically by solving the two coupled linear ordinary differential equations:

$$\ddot{R} = -\omega^2(R - D - d_{int}) \quad (4.11)$$

$$\ddot{D} = -\omega_1^2(D - D^0) + \omega^2(R - D - d_{int}) \quad (4.12)$$

with the frequencies

$$\omega^2 = \frac{k}{\mu}, \quad \omega_1^2 = \frac{k_1}{\mu_1}. \quad (4.13)$$

The solution in the entrance channel and the knowledge of the final deformation energy $E_d(\infty)$ are sufficient to find an analytical expression for the fusion barrier V_B which will be shown in the following.

Here, we shortly present the solution of the EOMs (4.11),(4.12). For a more detailed derivation look in appendix C where also the more general case of two different springs is discussed. The solution for the distance $R(t)$ and the vibronic coordinate $D(t)$ with the initial conditions

$$R(0) = D^0 + d_{int}, \quad \dot{R}(0) = v \quad (4.14)$$

$$D(0) = D^0, \quad \dot{D}(0) = 0 \quad (4.15)$$

is given by

$$R(t) = \frac{v}{\omega} \sum_{i=1}^2 a_i \sin(\Omega_i t) + (D^0 + d_{int}), \quad (4.16)$$

$$D(t) = \frac{v}{\omega} \sum_{i=1}^2 b_i \sin(\Omega_i t) + D^0 \quad (4.17)$$

with the fundamental eigenfrequencies

$$\Omega_{1/2} = \omega \underbrace{\sqrt{\kappa + 1 \pm \sqrt{\kappa^2 + 1}}}_{f_{1/2}(\kappa)} \quad (4.18)$$

and the amplitudes

$$a_{1/2} = \frac{1}{2 f_{1/2}(\kappa)} \left(1 \mp \frac{\kappa}{\sqrt{\kappa^2 + 1}}\right) \quad (4.19a)$$

$$b_{1/2} = \mp \frac{1}{2 f_{1/2}(\kappa)} \frac{1}{\sqrt{\kappa^2 + 1}}, \quad (4.19b)$$

where the ratio κ is defined as

$$\kappa = \frac{k_1}{k} = \frac{\omega_1^2}{2\omega^2}. \quad (4.20)$$

To calculate the fusion threshold, we need to determine the potential energy

$$E_r = \frac{\mu\omega^2}{2} (R(t) - D(t) - d_{int})^2 \Big|_{t=t_r}$$

at the returning time t_r with $\dot{R}(t_r) = 0$. Using (4.16) we arrive at

$$a_1\Omega_1 \cos(\Omega_1 t_r) + a_2\Omega_2 \cos(\Omega_2 t_r) \stackrel{!}{=} 0. \quad (4.21)$$

This equation cannot be solved analytically but the returning time can be approximated by

$$t_r \approx \frac{\pi}{2\Omega_2}$$

due to the fact that the second term in Eq. (4.21) dominates ($\frac{a_1}{a_2} \ll 1$ in the relevant range of the parameter κ). Then the potential energy E_r can be written as

$$E_r = \alpha(\kappa) E_{c.m.} \quad (4.22)$$

with the impact energy $E_{c.m.} = \frac{\mu}{2} v^2$ and the coefficient

$$\alpha(\kappa) = \left[(a_1(\kappa) - b_1(\kappa)) \sin\left(\frac{\pi f_1(\kappa)}{2 f_2(\kappa)}\right) + a_2(\kappa) - b_2(\kappa) \right]^2 \quad (4.23)$$

or inserting Eq. (4.19a), (4.19b)

$$\alpha(\kappa) = \frac{1}{4(\kappa^2 + 1)} \left[\left(\frac{\kappa - 1 - \sqrt{\kappa^2 + 1}}{\sqrt{\kappa + 1} + \sqrt{\kappa^2 + 1}} \right) \sin\left(\frac{\pi \kappa + 1 + \sqrt{\kappa^2 + 1}}{2\sqrt{2\kappa}}\right) - \frac{\kappa - 1 + \sqrt{\kappa^2 + 1}}{\sqrt{\kappa + 1} - \sqrt{\kappa^2 + 1}} \right]^2. \quad (4.24)$$

Comparing the potential energy E_r with the final deformation energy $E_d(\infty) = E_{cm} - \Delta E$, we can estimate the fusion threshold. As mentioned above, we find that ΔE , averaged over the initial orientation, is nearly 17 eV for the microscopic calculations of $C_{60} + C_{60}$ scattering events independent of the initial impact energy in the investigated energy range 40 eV – 104 eV (see Fig. 4.4). If E_r is smaller than the final deformation energy $E_d(\infty)$, the potential W in the exit channel is attractive, hence opening the channel for fusion (see Fig. 4.6). Setting $E_r \stackrel{!}{=} E_d(\infty)$, we find for the fusion threshold ($V_B = E_{c.m.}$)

$$V_B = \frac{\Delta E}{1 - \alpha(\kappa)}. \quad (4.25)$$

Of course, the relation (4.25) is only a lower limit, since the reversible energy transfer (vibrational energy to c.m. energy) during the recoil is neglected. In Fig. 4.8 the fusion

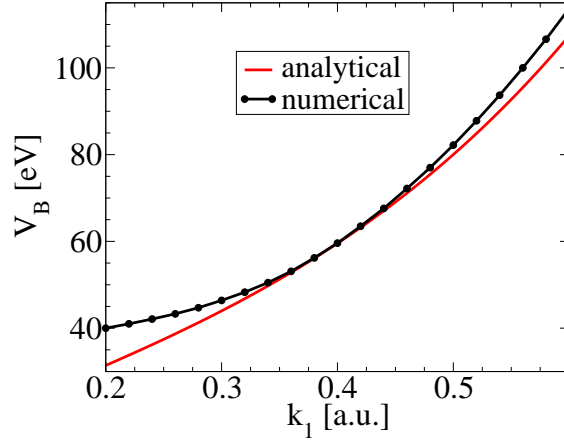


Figure 4.8: The fusion barrier V_B as a function of the force constant k_1 with the analytical (solid line) and the numerical result (dashed line) for $k = 0.12$ a.u. and $\Delta E = 20$ eV.

threshold is displayed as a function of the vibrational spring constant k_1 using the analytical formula (4.25). Additionally the numerical result is shown which has been calculated by solving the Newton-equations (4.8) for various impact energies with a Runge-Kutta method. The numerical fusion threshold is always slightly larger than the analytical value due to the reversible energy transfer in the exit channel (bouncing effect). However, this effect is not very large, so the analytical formula gives a satisfactory result.

Comparison with QMD results

Taking the results from the microscopic $C_{60} + C_{60}$ calculations, we can make a comparison of the model predictions and the full QMD results. The vibrational spring force constant $k_1 = 0.51$ a.u. corresponds to the $H_g(1)$ mode of C_{60} ($T_{exp} = 124$ fs) and has been evaluated using Eq. (4.13) with the corresponding relative masses for C_{60} . The interaction force constant $k = 0.12$ a.u. is obtained from the QMD results of the deformation potential (see Fig. 4.7a). Finally the energy release is given by $\Delta E = 17$ eV (see Fig. 4.4). Inserting the values in Eq. (4.24) we get a fusion threshold V_B of 82 eV (see Fig. 4.8). The numerical model calculations show a slightly higher fusion threshold of 85 eV due to the reversible energy transfer in the exit channel as mentioned above.

Snapshots of the $C_{60} + C_{60}$ and spring + spring collision dynamics are displayed in Fig. 4.9 illustrating the two reaction types, inelastic scattering resp. fusion. Furthermore, the dynamics for different impact energies is plotted in Fig. 4.10 comparing the model and the microscopic $C_{60} + C_{60}$ QMD results qualitatively. In particular the vibrational energy E_{vib} , the kinetic energy E_{kin} and the distance R are plotted as a function of time. The first two examples for $E_{cm} = 40$ and 60 eV show inelastic scattering, whereas the last collision for $E_{cm} = 150$ eV is a fusion event. A good agreement between the model and the microscopic calculations can be found. In the entrance channel the dynamics is nearly identical, also the

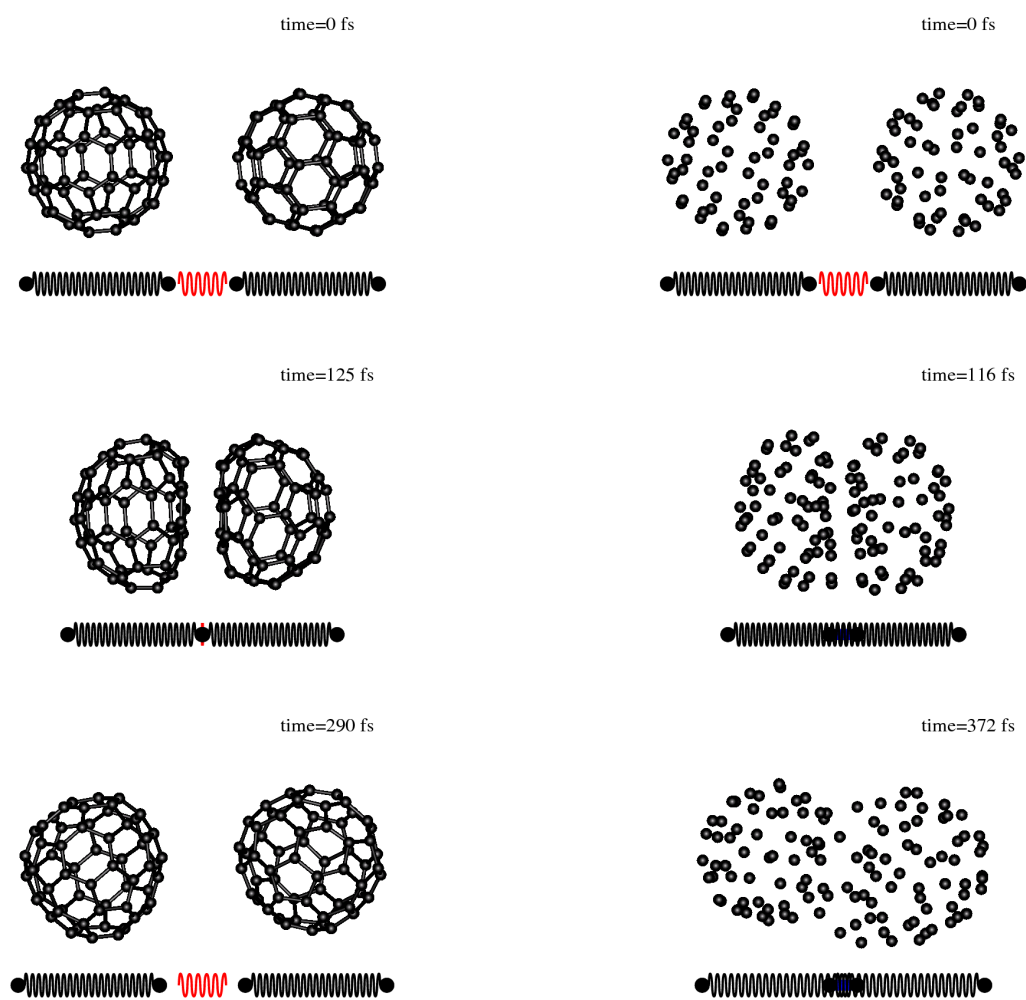


Figure 4.9: Snapshots of the full microscopic $C_{60} + C_{60}$ collision and the spring model for inelastic scattering (left) and fusion (right) for an impact energy of 40 eV resp. 104 eV.

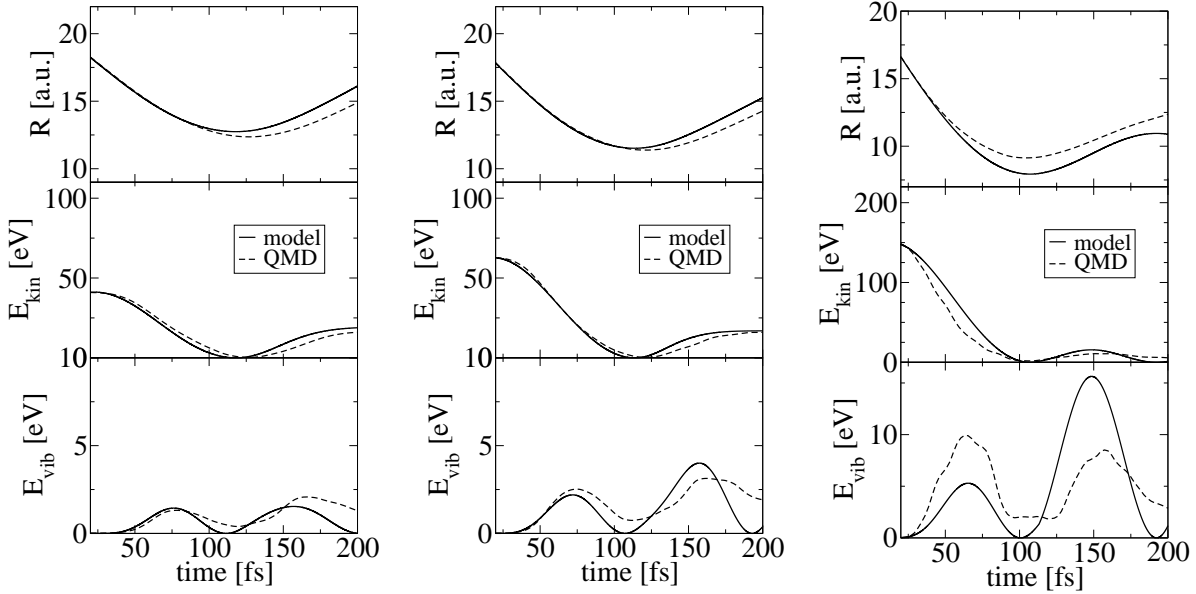


Figure 4.10: Comparison of the model calculation with the microscopic $C_{60} + C_{60}$ results for impact energies of 40, 60 and 150 eV. The distance R , the kinetic energy E_{kin} and the vibrational energy E_{vib} are shown as a function of time.

final kinetic energy matches. The characteristic double hump structure of the vibrational energy is reproduced very well.

The model predictions can also be extended to other fullerene collisions or collision conditions. In Table 4.1 the experimental fusion barriers for different kinds of fullerene collisions are shown. They will be compared with former QMD and the simple model results. In experiments, where hot C_{60} molecules ($T=2000$ K) have been used, decreased fusion barriers were found [213]. Scaling the force constant of the spring mode k_1 with a factor 0.85 we find a good agreement with the experimental result. This means by softening the oblate-prolate mode the fusion barrier can be lowered. Furthermore, for collisions with C_{70} an enhanced spring mode constant $k_i = 0.55$ a.u. gives satisfactory results with an increased fusion barrier.

In the following sections, a justification and physical interpretation will be given for the scaling of the vibrational constant k_1 ($H_g(1)$ mode) for $T=2000$ K, and for the increased spring constant k_1 of the collisions with the C_{70} fullerene.

	QMD [213] $T = 0$ K	Model k_i^{exp}	QMD [213] $T = 2000$ K	Model $k_i^{exp} \cdot 0.85$	Experiment [213]
$C_{60} + C_{60}$	80	82	60	65	60 ± 1
$C_{60} + C_{70}$	94	87	70	69	70 ± 6.5
$C_{70} + C_{70}$	104	93	75	73	76 ± 4

Table 4.1: The fusion barriers V_B in eV. The values of the model are obtained with Eq. (4.24) using the parameters $k_1^{exp}(C_{60}) = 0.51$ a.u. resp. $k_2^{exp}(C_{70}) = 0.55$ a.u. (resp. the scaled values), $k = 0.12$ a.u. and $\Delta E = 17$ eV.

4.1.3 $C_{60} + C_{60}$: Fusion versus scattering for finite temperatures

Up to now, only calculations of fullerene reactions without considering any temperature has been presented. Of course, in most cases experiments has been done at finite temperatures. For room temperature the effect should be small since only a vibrational energy of 2 eV is stored, but for higher temperatures the effect is notable.

An example is the $C_{60} + C_{60}$ fusion barrier, which was investigated in the experiments at $T = 2000$ K. For such a setup a much lower fusion barrier of 60 eV has been found, than expected from ab-initio molecular dynamics simulations at zero temperature. In the analytical trajectory model the fusion barrier could be lowered by choosing a softer vibrational $H_g(1)$ -mode. To check the assumption of a softer oblate-prolate mode and other aspects of the collision dynamics, calculations at $T = 2000$ K will be presented in this chapter.

Preparation of the initial state for finite temperatures

Due to the unknown analytical structure of the high-dimensional energy surface depending on 174 coordinates, it is impossible to find an equilibrated initial state explicitly. To prepare a hot C_{60} with a given temperature T , simulations were initiated with only *kinetic* vibrational energy of

$$E_{vib} = \frac{f}{2} kT$$

with $f=174$ the number of degrees of freedom for C_{60} ⁴. For a temperature $T = 2000$ K ($k = 8.61735 \cdot 10^{-5} \frac{\text{eV}}{\text{K}}$ [219]) the vibrational energy is given in total by 15 eV. The vibrational energy E_{vib} was equally distributed among all 174 normal modes for the initial time $t = 0$. In Figure 4.11 the relaxation process is displayed. The kinetic energy drops within 25 fs to half of the initial value (indicated by the red line). This is understandable since the kinetic energy is converted into potential energy. Due to the virial theorem, the kinetic energy is equal to the potential energy for a system of harmonic oscillators (\equiv normal modes) in the

⁴In particular, the translational and rotational degrees of freedom were excluded to ensure nearly the same collision geometries in the following collision scenarios compared to the $T = 0$ calculations.

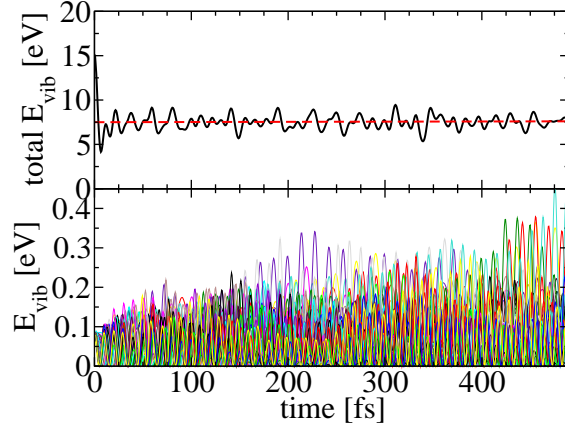


Figure 4.11: Energy relaxation of C_{60} (equilibrium geometry) with an initial kinetic vibrational energy of 15 eV. Upper part) The total kinetic energy as a function of time. Lower part) The kinetic energy of each normal mode as a function of time.

equilibrium. The virial theorem is only valid for the time averaged energies, so fluctuations around the theoretical value occur. The dynamics of the normal modes are much more complicated. It shows a strong coupling between the normal modes leading to an energy transfer between the modes (lower part of Fig. 4.11).

The oblate-prolate mode at $T = 2000$ K

To show how the period $T_{H_g(1)}$ of the $H_g(1)$ mode changes for a vibrationally hot C_{60} , calculations have been performed with a nonzero initial amplitude of the oblate-prolate mode and some initial kinetic vibrational energy for all normal modes as mentioned above. In Figure 4.12 the kinetic energies of the normal modes are displayed for two excitation energies of the $H_g(1)$ mode. One can see the dominating oblate-prolate mode oscillation which is not fully harmonic due to the interaction with other modes. We found that the period $T_{H_g(1)}$ increases with increasing temperature. For a cold molecule $T_{H_g(1)}$ is 115 fs whereas it is increased to 121 fs for $T = 2000$ K (left side in Fig. 4.12). The softening of the $H_g(1)$ mode can be explained by a stronger coupling to the other normal modes due to the anharmonic parts of the potential energy surface.

Dynamics of $C_{60} + C_{60}$ collisions

For the collision dynamics we started with an initial state taken from the calculation above (see Fig. 4.11), i.e. the two molecules were initialized to the states obtained at the arbitrarily selected times $t = 375$ fs resp. $t = 605$ fs. In principle, averaging over far more different initial vibrational hot states would be desirable to simulate the temperature. That, however, is a very time-consuming task. But for our purpose, it is sufficient to consider only one initial configuration and to study the effect of the vibrational excitation. To compare the collision

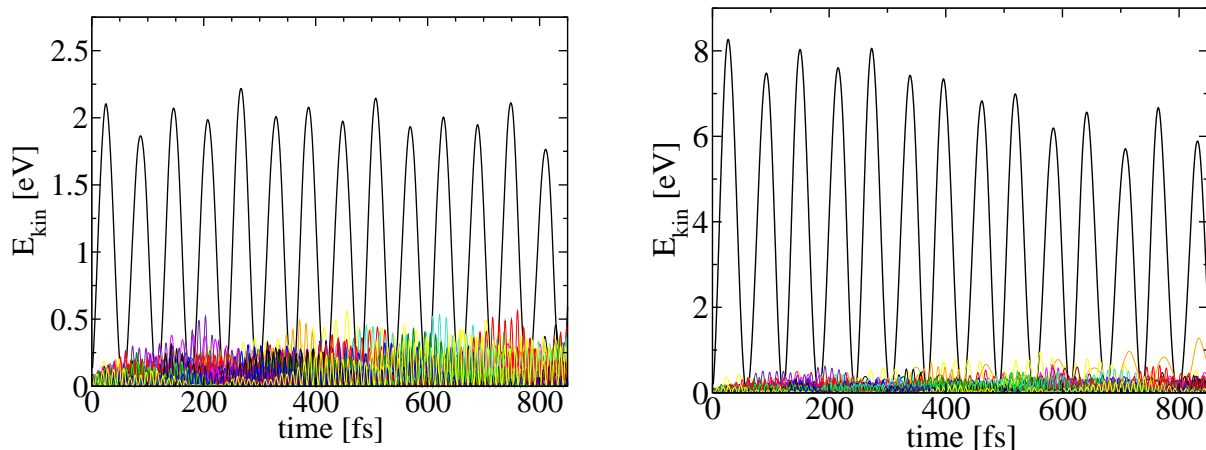


Figure 4.12: The kinetic energies of all normal modes as a function of time for C_{60} with an initial prolate geometry ($T = 2000$ K). The dominating black line indicates the oblate-prolate mode ($H_g(1)$) for an initial excitation energy of 2 eV (left) respectively 8 eV (right).

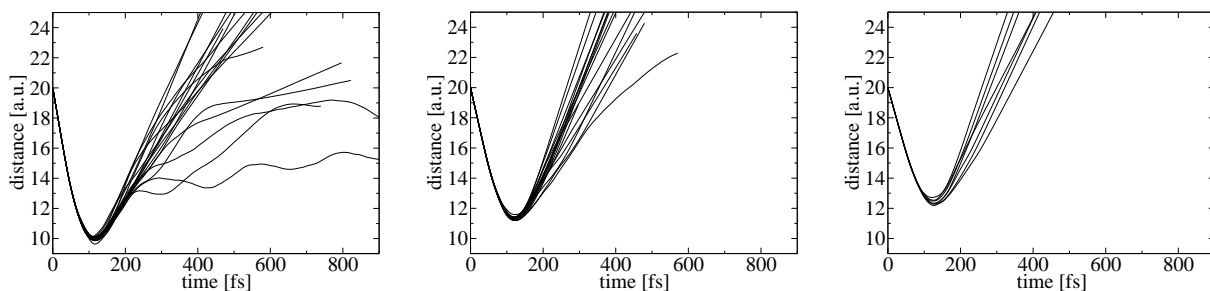


Figure 4.13: Collision dynamics for an impact energy of 104 eV (left), 60 eV (middle) and 40 eV (right) for $T=2000$ K. The C_{60} - C_{60} distance R is displayed as a function of time for the different collision events.

dynamics for $T = 2000$ K with the former calculations for $T = 0$ in Chapter 4.1.1, the same initial rotation angles have been used. Only the cold molecules were replaced by the hot C_{60} s (see above). For the impact energies of 40, 60 and 104 eV the trajectories of the different collision events are plotted in Fig. 4.13. In general, collisions at $T = 2000$ K are more inelastic than for cold molecules, as expected. Where only two fusion events can be found for $T = 0$, three fusion events occur for $T = 2000$ K.

In Figure 4.14 the averaged deformation energy $U(R)$ for the three impact energies is compared with the $T = 0$ calculation. Besides small oscillations due to the thermic vibrational motion for $T = 2000$ K, no major difference can be found between cold and hot molecules. Also the averaged return distance R_{ret} does not change significantly (Table 4.2).

$E_{c.m.}$ [eV]	R_{ret} [a.u.]	
	$T = 2000$ K	$T = 0$
104	9.98	10.0
60	11.34	11.4
40	12.4	12.4

Table 4.2: Comparison of the return distance R_{ret} averaged over 17 events for a temperature $T = 2000$ K (15 eV) and $T = 0$ of the $C_{60} + C_{60}$ collision.

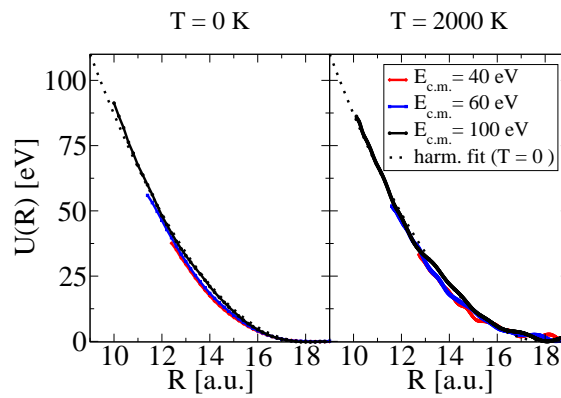


Figure 4.14: Comparison of the deformation energy U as function of the distance R for $T = 0$ (left) and $T = 2000$ K (right).

Comparison with the trajectory model

The ratio $\frac{k_1(2000K)}{k_1(0K)} = \left(\frac{T_{H_g(1)}(0K)}{T_{H_g(1)}(2000K)} \right)^2 = 0.9$ is very similar to the scaling factor 0.85 obtained from the experimental values ($T = 2000$ K) and the analytical trajectory model results for $T = 0$ (see Table 4.1). Furthermore we find that the deformation potential for $T = 0$ K is identical with that of 2000 K indicating no change in the interaction force constant k . In conclusion, the trajectory model predictions are consistent with the experimental results at $T = 2000$ K.

4.1.4 $C_{70} + C_{70}$: Fusion versus scattering

In this section some results for $C_{70} + C_{70}$ collisions at $T = 0$ will be presented with special focus on the trajectory model predictions for the fusion barrier. In particular, it is known that the fusion barrier for $C_{70} + C_{70}$ is higher than for $C_{60} + C_{60}$ collisions [213]. Therefore, we take a closer look to the normal mode analysis of the collision dynamics which provides insights into the fusion mechanism.

The C_{70} molecule

The C_{70} molecule is the next higher fullerene to C_{60} whose much lower symmetry is D_{5h} . It is shaped like an ellipsoid and can be constructed by splitting C_{60} into two halves perpendicular to the C_5 -axis and adding a ring of ten carbon atoms in between. Corresponding to this symmetry, the molecule has 8 different bond lengths. The geometrical properties have been calculated using the LDA functional and the same basis set as for C_{60} . They are displayed in Table 4.3. The results are compared to other theoretical and to experimental work and shows a good agreement ⁵.

The vibrational spectrum

The spectrum of C_{70} is not as well understood as in the case of C_{60} . 122 distinct eigenfrequencies, either one- or twofold, exist, due to the much lower symmetry compared to C_{60} . The more complex spectrum makes it more difficult to relate measured frequencies to theoretical values. Experimentally the spectrum was investigated with Raman [223] and infrared spectroscopy [224] in the nineties. Phenomenological models as well as first principle approaches [220, 225, 226] have been performed showing frequencies in the range of 230 to 1600 cm^{-1} . We have calculated the vibrational spectrum in the same way as for C_{60} . The calculated modes with the lowest frequencies are a doublet E'_2 at 237 cm^{-1} , a doublet

⁵More literature can be found in the book by Dresselhaus [165].

	present (LDA)	LDA ([220])	experimental ([221])
d ₁₁	1.443	1.442	1.46
d ₁₂	1.382	1.392	1.37
d ₂₃	1.440	1.439	1.47
d ₃₃	1.376	1.387	1.37
d ₃₄	1.440	1.439	1.46
d ₄₄	1.424	1.431	1.47
d ₄₅	1.410	1.415	1.39
d ₅₅	1.456	1.456	1.41
long diameter	7.90	-	7.96 ([222])
short diameter	7.08	-	7.12 ([222])

Table 4.3: Bond lengths and other ground state properties of C₇₀ in units of Å.

	present (LDA)	LDA ([220])	MD simulation([225])
E'_2	237	219	235
E''_1	264	242	250
A'_1	270	262	251

Table 4.4: Vibrational frequencies for C₇₀

E''_1 at 264 cm⁻¹, and a singlet A'_1 at 270 cm⁻¹. These five modes correspond to the lowest eigenmode $H_g(1)$ (271 cm⁻¹) mode of C₆₀, which are split due to the lower symmetry of C₇₀⁶. In Table 4.4 the values are compared with another LDA calculation [220], in which the dynamical matrix is diagonalized as in our work but using also symmetry constraints, and a Car-Parrinello molecular-dynamics simulation [225], based on an analysis of trajectories (avoiding the calculation of the dynamical matrix). The lowest three frequencies measured by Raman spectroscopy [223] are 228, 250-267 cm⁻¹ and may be related to the E'_2 doublet resp. to the $A'_1 + E''_1$ doublet.

Collision dynamics

Even for the direct collision of C₇₀+C₇₀ more geometrical configurations are possible

⁶The largest common subgroup of I_h (C₆₀) and D_{5h} (C₇₀) is the C_{5v} group. Classifying the normal modes of C₆₀ and C₇₀ only with the C_{5v} irreducible representations, a comparison between the two molecules is possible. The H_g mode is split into an A'_1 , a E''_1 , and a E'_2 mode.

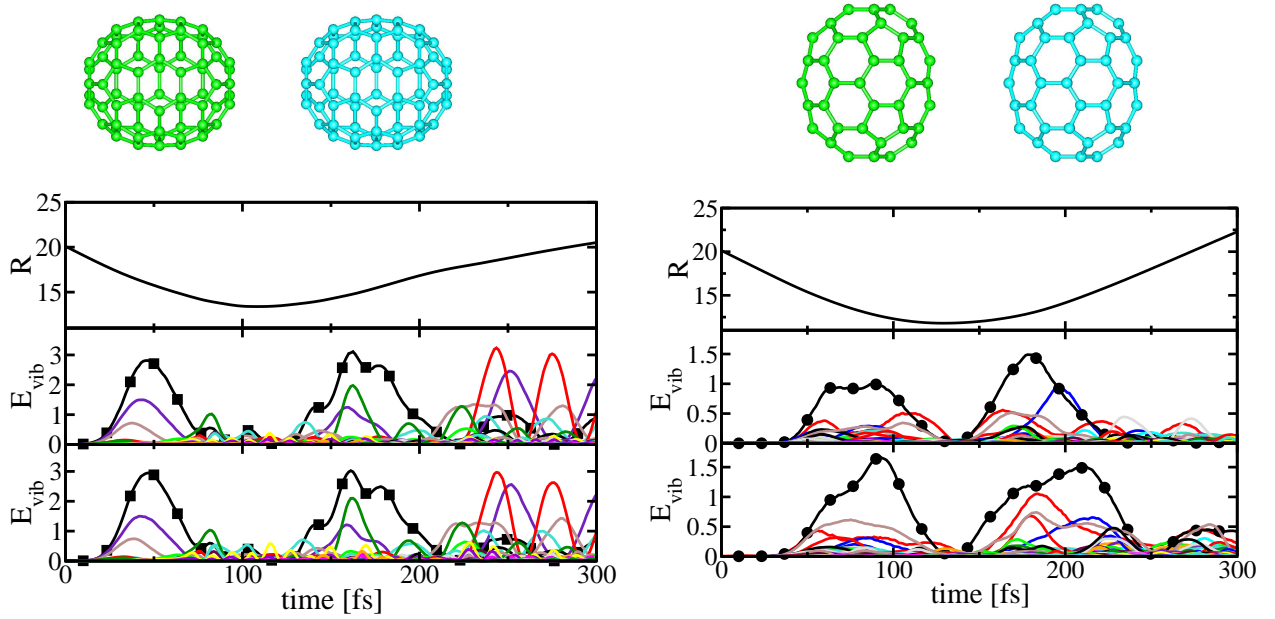


Figure 4.15: $C_{70} + C_{70}$ collisions for the two symmetric initial conditions (top). The distance R (in a.u.) and the vibrational mode energies E_{vib} (in eV) for the left (middle) and for the right collision partner (down) with the vibrational modes A'_1 (■) and E''_1 (●) are plotted as a function of time.

than for C_{60} , since the system has two principle axes. We will show inelastic scattering events for four different orientations at an impact energy of 60 eV. For the two symmetric initial orientations a strong excitation of the A'_1 (270 cm^{-1}) mode (collision direction parallel to the long principle axis) resp. of the E''_1 (264 cm^{-1}) mode (collision direction parallel to the short principle axis) occur (Fig. 4.15). In the case of asymmetric initial orientations a mixture of both modes, the A'_1 and the E''_1 mode, is excited (Fig. 4.16). Thus the situation is more complex than for $C_{60} + C_{60}$ collisions. However, the main feature, the characteristic double hump structure of the dominant modes during the collision, can be seen. For the asymmetric initial orientations also rotational excitation occurs. In all cases the dominant vibrational modes, A'_1 and/or E''_1 , relax very quickly after the collision process due to vibrational coupling to the other modes.

Consequences for the trajectory model

Now, we can adapt the trajectory model for $C_{70} + C_{70}$ collisions. In particular, we see two dominant modes, A'_1 and E''_1 , which are splittings of the $H_g(1)$ mode in C_{60} due the lower symmetry⁷. Using the relation $\omega_i^2 = \frac{k_i}{\mu_i}$ with ω_i the vibrational frequency of the modes

⁷Surprisingly, the third mode E'_2 of the $H_g(1)$ splitting is not significantly involved in the collision dynamics.

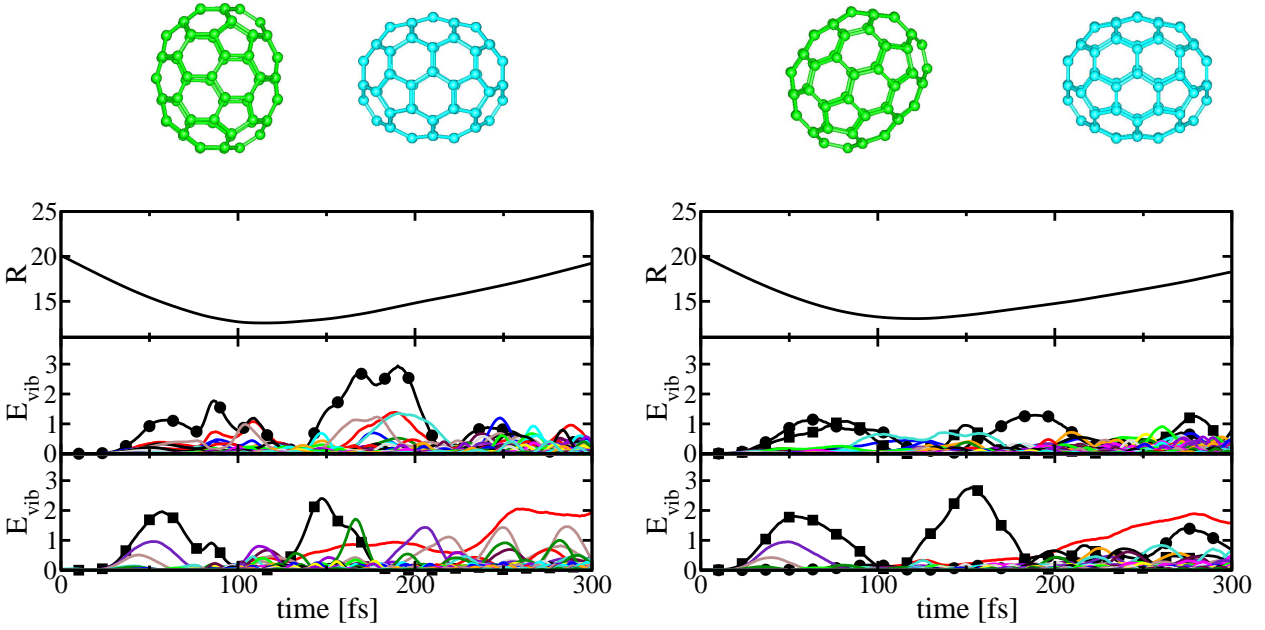


Figure 4.16: $C_{70} + C_{70}$ collisions for two asymmetric initial orientations (top) with the same properties as in Fig. 4.15.

and $\mu_i = \frac{M_{C_{70}}}{4}$ the relative mass of C_{70} , the vibrational force constant k_i can be calculated (see Fig. 4.17). As mentioned above the LDA calculation overestimates the vibrational frequencies compared with the experimental values.

For a symmetric collision shown above the same mode is excited in each fullerene making it possible to use the formula for symmetric springs (4.25). Experimentally it is not clear which frequency belongs to a certain mode (A'_1 or E''_1). For a first estimate we take the experimental vibrational frequency of 267cm^{-1} [223] which may be related to the A'_1 resp. E''_1 . This leads to a force constant $k_1 = 0.55$ a.u. Under the assumption that the other model parameters from the $C_{60} + C_{60}$ collisions do not change, Equation (4.25) gives a fusion barrier V_B of 93 eV which is higher than the $C_{60} + C_{60}$ value and agrees well with the experiments. For asymmetric collisions more than one mode is excited (see Fig. 4.15). In this case, the trajectory model for non identical springs (spring constants $k_1 \neq k_2$) can be applied (see Appendix C) where a similar equation for the fusion barrier $V_B(k_1, k_2, k)$ as Eq. (4.23) can be derived. However, if the spring constants k_1 and k_2 do not deviate very much from the mean value $\bar{k} = \frac{1}{2}(k_1 + k_2)$: the exact result $V_B(k_1, k_2, k)$ for non identical springs does not differ significantly from $V_B(\bar{k}, k)$ obtained with Eq. (4.24). This leads to similar fusion barriers for the asymmetric $C_{70} + C_{70}$ collisions since the A'_1 and E''_1 have very similar frequencies.

Another asymmetric collision is the $C_{60} + C_{70}$ reaction. Like shown in section 4.1.1 the oblate-prolate mode $H_g(1)$ mode will be excited during the $C_{60} + C_{60}$ collision. Calculating the fusion barrier $V_B(\frac{1}{2}(k_1 + k_2), k)$ for the $C_{60} + C_{70}$ collision with $k_1 = 0.51$ a.u. (C_{60}) and

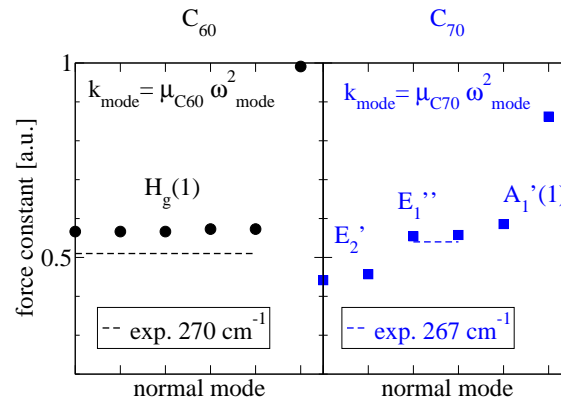


Figure 4.17: The spring constants k of the $H_g(1)$ mode in C_{60} and the splitting in C_{70} . The circles resp. squares indicate the theoretical values obtained with LDA, and the dashed lines the experimental result for the $H_g(1)$ in C_{60} resp. E_1'' mode in C_{70} .

$k_2 = 0.55$ a.u. (C_{70}) a value of 87 eV is obtained, which is in between the $C_{60} + C_{60}$ and $C_{70} + C_{60}$ collisions as expected.

4.2 Nonadiabatic dynamics of fullerene-fullerene collisions

The collision dynamics of C_{60} - C_{60} systems in the (c.m.) energy range up to 500 eV have been investigated in the past [104]. Different reaction channels were observed. Depending on the collision energy scattering, fusion or multifragmentation occurs. All these calculations were done in the adiabatic framework, e.g. no electronic excitation was included.

In this chapter we will show computational results of collisions up to energies of 1.8 MeV where electronic excitation dominates, i.e. a genuine nonadiabatic process. We will find different excitation regimes from vibrational to highly electronic excitation, leading to multifragmentation up to complete atomization of the fullerene cages.

The initial state of the molecules is the ground state (diameter of C_{60} : 13.5 a.u.) with a given impact parameter b and the impact velocity v in the center of mass system ($v < 0.45$ a.u.). During the inelastic collision the system dissipates translational energy into internal energy of the molecules. The total energy loss ΔE is defined as the difference of the translational energy of both molecules $E_{kin} = \frac{\mu}{2}v^2$ (shortly) after and before the collision. The energy is converted into excitation energy of the molecules which consists of two parts:

$$\Delta E = \Delta E_{vib} + \Delta E_{el}$$

with the vibrational energy $\Delta E_{vib} = E_{def} + \Delta E_{vib}^{kin}$ and the electronic excitation energy ΔE_{el} . The deformation energy E_{def} is obtained by calculating the electronic groundstate energy difference between the initial and the final geometrical configuration.

4.2.1 Fragmentation regimes in $C_{60} + C_{60}$ collisions

Varying the initial velocity, different collision regimes can be distinguished: adiabatic collisions (< 500 eV) with scattering, fusion as shown in the last section as well as fragmentation processes, and nonadiabatic collisions (> 500 eV) with fragmentation. In Figure 4.18 (left) one can see that the vibrational excitation dominates for low collision energies and the electronic excitation for high collision energies. We find a maximum of the vibrational excitation and also of the total energy loss ΔE at an impact energy $E_{c.m.} = 50$ keV. For impact energies higher than 400 keV a plateau of ΔE can be observed which is dominated by the electronic excitation energy. A similar behaviour can be found for $C^+ - C_{60}$ collisions [32], which will be shown later. At the very high impact energies (electronic excitation !), the scattering angle θ defined by the change of the c.m. momenta of the collision partners, is nearly zero, only for lower impact energies (vibrational excitation !) the momentum transfer, i.e. the scattering angle, is much larger (see Fig. 4.18 (right)). We find also that the scattering angle is always smaller as compared with the collision of elastic rigid spheres (billiard model)

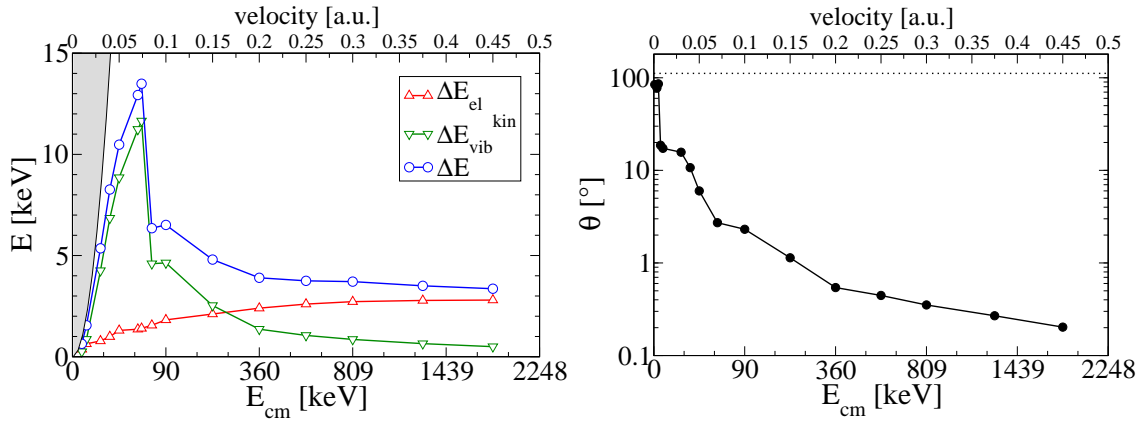


Figure 4.18: Energy absorption (left) and the scattering angle θ (right) as a function of the impact energy for a fixed impact parameter $b = 7.5$ a.u. The grey area (left) indicates the energetically forbidden area. The dotted horizontal line in the right figure indicates the scattering angle $\theta = 111.5^\circ$ for the hard sphere model (billiard model: $\cos \theta = 2 \left(\frac{b}{D_{C60}} \right)^2 - 1$).

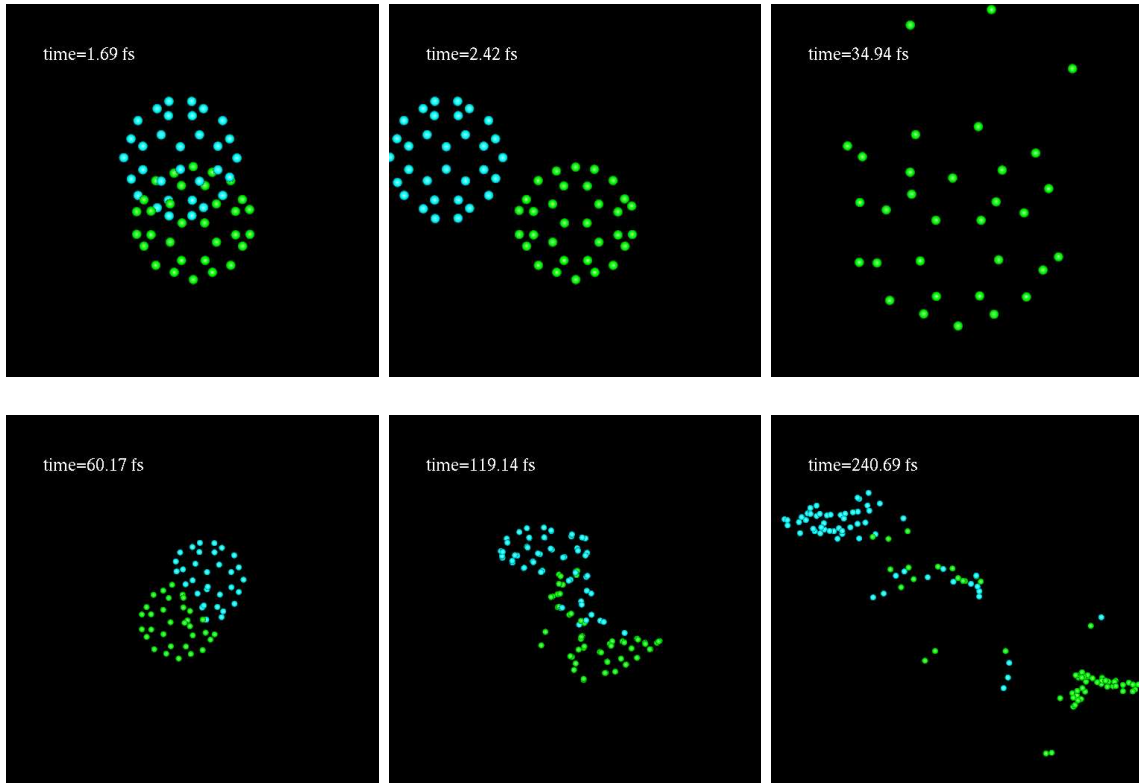


Figure 4.19: Snapshots of the collision in the rest frame of one C₆₀ for $v = 0.45$ a.u. (1.8 MeV) (Upper part) and $v = 0.01$ a.u. (900 eV) (Lower part) ($b = 7.5$ a.u.)

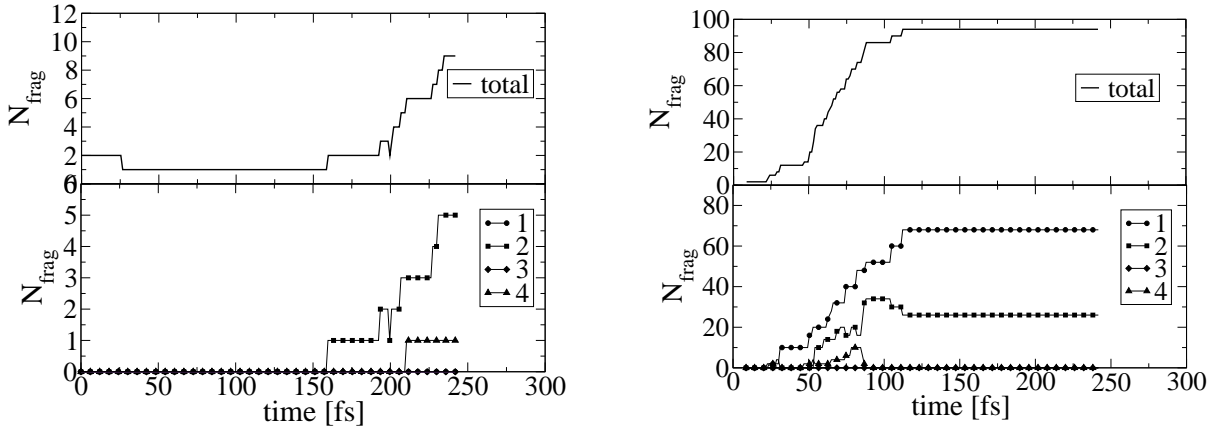


Figure 4.20: The total number of fragments and the number of monomers (1), dimers (2) etc. as a function of time for an initial velocity $v = 0.01$ a.u. (900 eV) (left), and $v = 0.45$ a.u. (1.8 MeV) (right) and an impact parameter of 7.5 a.u.

within the investigated energy range from 40 eV to 1.8 MeV since the collisions are more or less inelastic in all cases.

In Figure 4.19 some snapshots of the collision dynamics is shown for two different impact velocities. For the highest impact velocity $v = 0.45$ a.u. (1.8 MeV) the interaction time between the nuclei is very short, so the vibrational excitation is only small. Instead the electronic excitation dominates, since the electron dynamics is much faster. The molecules are not destroyed during the interaction time. Only few atoms in the upper part of the cage have got some kinetic energy. But due to the high electronic excitation the cages will start to expand and fragment isotropically into monomers and dimers (see Fig. 4.20). In the lower part of Fig. 4.19 one can see an example for an initial velocity $v = 0.01$ a.u. (900 eV). The collision dynamics is much slower, so the vibrational excitation dominates and the electronic excitation is small. We see a collective flow effect which has been proposed in QMD calculations for an impact energy of 500 eV and has been studied in nuclear physics (see ref. [104] and refs. therein). The cages form a superdense state during the approach phase. For later times we find multifragmentation with collision products of monomers, dimers up to much larger fragments (see Fig. 4.20). The larger collision products fragment under a certain angle in opposite directions ("side splash").

4.2.2 Dependence on the impact parameter

The results shown before were obtained for an impact parameter $b = 7.5$ a.u. and different impact energies. The energy loss ΔE depends strongly on the impact parameter b . As an example, the absorbed energy as a function of b is plotted in Fig. 4.21 for an impact velocity of 0.45 a.u. where the electronic excitation dominates. For a central collision ($b = 0$) the fullerenes interact very strongly and the maximum amount of energy will be lost. The energy

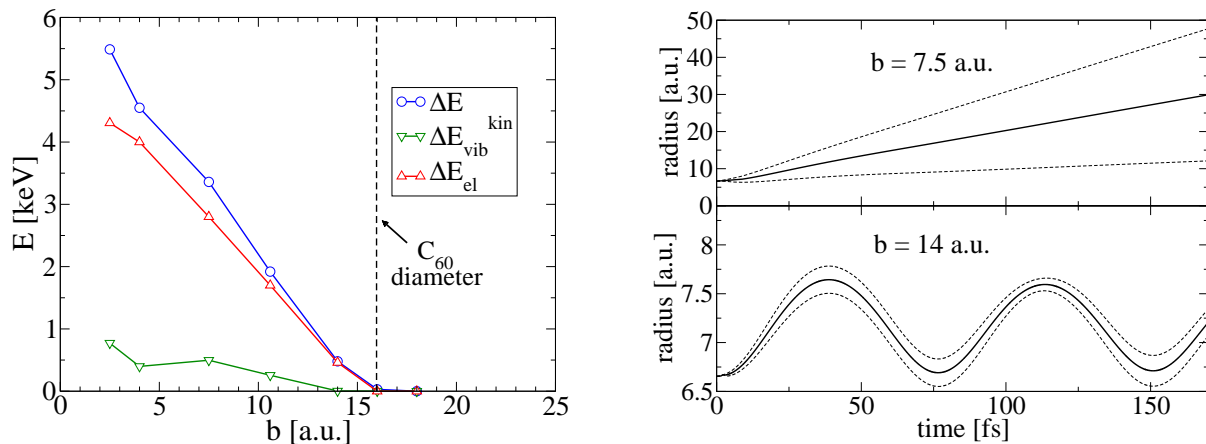


Figure 4.21: C_{60} - C_{60} collision for an impact velocity $v = 0.45$ a.u. (Left) Energy loss as a function of the impact parameter b . (Right) The mean radius of one collision partner, i.e. a single C_{60} , as a function of time for an impact parameter $b = 7.5$ a.u. (top) and $b = 14$ a.u. (bottom). The dashed lines indicates the upper and lower limit by means of the standard deviation.

loss decreases with increasing impact parameter b and vanishes for an impact parameter bigger than the diameter of C_{60} . The excitation scheme found for $b = 7.5$ a.u. does not change for the other impact parameters. The (almost exclusively electronic) excitation energy lies in the range of several keV leading to fragmentation into monomers and dimers. There were always some faster atoms which are knocked out of the molecule due to a more or less direct nucleus-nucleus collision. For smaller impact parameters the probability for such direct "knock outs" is large.

Note, that the interaction range is larger than the geometrical diameter due to the electron density distribution. For near grazing collisions ($b = 14$ a.u.) the molecules will be highly electronically excited ($\Delta E = 240$ eV) leading not directly to fragmentation but to vibrational excitation, in particular of the breathing mode $A_g(1)$ with a period of $T_{A_g(1)} = 75$ fs (see Fig. 4.21). The breathing mode period is in good agreement with the result for laser excited C_{60} (see Fig. 3.21 in Chapter 3.3.3). This shows that the excitation of the breathing mode is rather insensitive to the particular electronic excitation mechanism.

4.2.3 Comparison with Ion-Fullerene collisions

For different impact velocities simulations of ion-fullerene collisions (H^+ , C^+ , Ar^+) have been investigated before in the same velocity range using the NA-QMD approach [32].

The impact energy scale is much different due to the different relative masses in the collision, e.g. the scaling factor is $\frac{\mu_{C_{60}+C_{60}}}{\mu_{Ar^++C_{60}}} = 20.5$ for the heaviest ion Ar^+ . As a consequence also the energy loss differs on the same scale with $\Delta E \sim \text{keV}$ for $C_{60} + C_{60}$ and $\Delta E \sim 10^{-1}$ keV

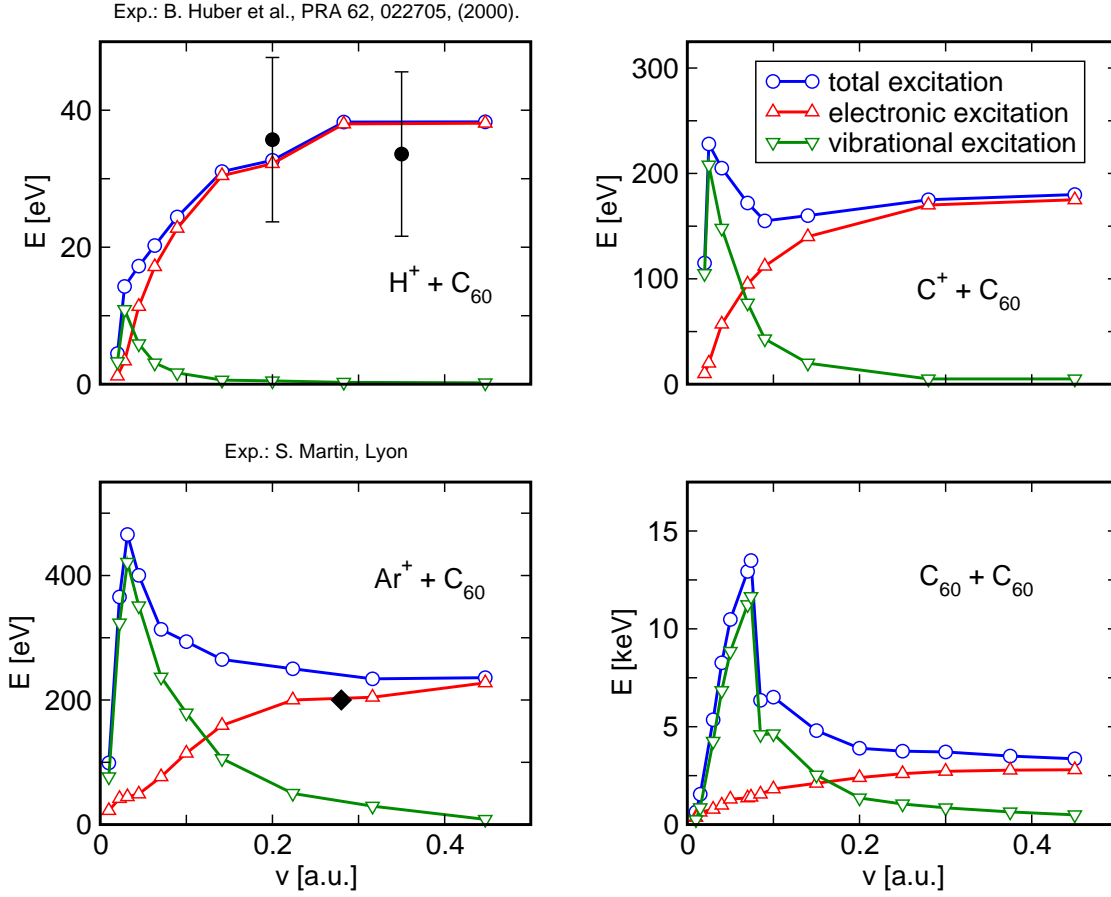


Figure 4.22: Energy absorption as a function of the impact energy for ion+C₆₀ collisions ($b = 2.0$ a.u.) (taken from ref. [32]) and C₆₀+C₆₀ collision ($b = 7.5$ a.u.) for a fixed geometry.

for the ion+C₆₀ collisions. However, the impact energy dependence of the energy loss is very similar for the heavier ions (C⁺, Ar⁺) and C₆₀+C₆₀ collisions (Fig. 4.22). We find a maximum of the energy loss at moderate velocities and a plateau for higher impact energies. The maximum is related to a strong excitation of vibrational energy whereas the electronic excitation is very small. In the high-energy regime the electronic excitation dominates. A clear tendency can be found in the energy characteristics going from the light to the heavier ions and the C₆₀ collision partners: The heavier the collision partners are, the more pronounced is the energy loss maximum. For hydrogen the effect is hidden by the dominating electronic excitation. Furthermore, the maximum is shifted to higher impact velocities for the C₆₀+C₆₀ collisions (from $v = 0.03$ a.u. to $v = 0.07$ a.u.).

Also the knock-out of single carbon atoms by the projectile can be seen in the ion-fullerene collisions for high velocities. They have been observed in Ar⁺-C₆₀ collision experiments with impact energies up to 20 keV [227]. However, in C₆₀+C₆₀ there should be far more such events due to the higher probability of direct atom-atom collisions.

5 Outlook

In this thesis, we have first of all demonstrated the universality of the ab-initio **NA-QMD** theory by applying it successfully to a broad class of very different **non-adiabatic** phenomena in finite atomic many-body systems (molecules, clusters), in particular in laser-induced as well as in collision-induced processes. In addition, long-standing questions in the physics of low-energy, i.e. **adiabatic** fullerene-fullerene collisions, have been clarified with the help of a astonishing simple analytical collision model, developed on the basis of fully microscopic **QMD**-results.

In Chapter 3, laser-induced processes were investigated, in particular the orientation dependence of the ionization of multielectronic diatomics (N_2 , O_2) [51], the isomerization of organic molecules (N_2H_2) [52] and the giant excitation of the breathing mode in fullerenes (C_{60}) [53]. In the first case, the orientation dependence of the ionization of multielectronic diatomics (N_2 , O_2) were studied in the LSDA approximation (Sect. 3.1). Both molecules show a characteristic orientation dependence of the ionization mainly caused by the different outermost electronic orbital (HOMO) in agreement with single active electron theories (ADK/SFA). However, also other lower-lying orbitals are involved indicating the role of many-electron effects. In the future, two improvements should be addressed for a more accurate treatment: One point is the use of other exchange-correlation functionals better suited for ionization, such as the optimized effective potentials of Krieger-Li-Iafrate (OEP/KLI) [228, 229] or the LB94 potential with gradient corrections suggested by van Leeuwen and Baerends [128, 230, 231], since it is known that the LSDA functional does not possess the proper long-range Coulombic tail ($-\frac{1}{r}$). The second point is the selection of the basis functions describing the electron continuum, and related to this, the parameters of the absorber in the energy space, where up to now no satisfactory and simple procedure has been found which guarantees convergence.

Besides the photoisomerization of organic molecules (N_2H_2) in Sect. 3.2, the (non)adiabatic dynamics of fullerenes was of special interest concerning laser-induced processes (Sect. 3.3) as well as collision-induced processes (Chapt. 4) [54]. We found that distinct vibrational modes play a dominant role, the breathing mode for the C_{60} fullerene dynamics excited by high-intensity laser pulses and the oblate-prolate mode in low-energy C_{60} - C_{60} collisions. In the case of collisions in the low-energy regime, a simple two-dimensional classical trajectory model was developed which allows surprisingly to understand (partly quantitatively !) the underlying collision mechanism for fusion and inelastic scattering.

In the future, a combination of laser- and collision-induced processes can be investigated regarding the question how the fullerene-fullerene collision process is influenced by the

laser-induced electronic excitation itself but also by the laser-induced vibrational excitation (breathing mode).

Preliminary calculations have been started showing a reduced fusion barrier (up to about 60 eV) and an enhanced fusion probability for electronically excited C_{60} - C_{60} collisions. These preliminary studies have been done with the same setup as in Chapter 4.1.1 but with an additional laser pulse during the approach phase (total laser duration: 100 fs; 800nm; 4×10^{12} W/cm²; $\mathbf{E} \parallel$ collision axis) [56]. Thereby, the $C_{60} + C_{60}$ system will be highly electronically excited (170 eV for each fullerene). Since the vibrational response to the laser excitation takes longer than the collision, the breathing mode does not influence the collision process. The reduced fusion barrier and enhanced fusion probability can be understood as a softening of the potential for the nuclei due to the electronic excitation. Hence, the oblate-prolate mode is also softened ($k_1 \downarrow$) which results in a smaller fusion barrier according to the trajectory model (see fig. 4.8). However, these phenomena must be studied in more detail, in particular with a time delay between laser excitation and collision, leading possibly to phase effects due to the excited breathing motion of the C_{60} cages.

In general, the interaction of fullerenes with laser irradiation will continue to be a topic of current and future research. For instance, recent experiments show differences in the ionization and fragmentation of C_{60} excited either by linearly or elliptically polarized laser fields which might be explained by multielectron dynamics effects [232, 233], but have not been checked theoretically, up to now. This, however, can be done with the present NA-QMD theory [234]. Another topic, opening a new field of physics, is the excitation with VUV resp. XUV femtosecond laser fields with tuneable photon energies of several electron Volts, which will be provided by the free electron lasers (FEL) [235]. Besides the structure analysis for biomolecules, the selective excitation of high lying electronic states of organic molecules or the physics in clusters can be studied, e.g. the energy absorption in atom clusters [236–239]. So far, the NA-QMD approach has been only successfully tested for the H-atom in the VUV range [240]. For multielectron systems, like metallic clusters, further advancements are necessary.

A

A.1 Number of excited electrons in TD-DFT

We shortly describe how we define the number of excited electrons N_{exc} in td-DFT. A major problem is that the many-body wavefunction is unknown within td-DFT. Therefore, we are dealing only with time-dependent density resp. the one-particle Kohn-Sham orbitals $|\psi^{j\sigma}(t)\rangle$ which are defined by the time-dependent Kohn-Sham equations (2.17). However, we will derive a formula which is easy to understand in the one-particle picture by projection to the adiabatic eigenstates.

If we consider no ionization (no absorber), the total number of electrons

$$N_e = \sum_{\sigma=\uparrow,\downarrow} N_e^\sigma \quad (\text{A.1})$$

with

$$N_e^\sigma = \sum_{j=1}^{N_e^\sigma} \langle \psi^{j\sigma}(t) | \psi^{j\sigma}(t) \rangle \quad (\text{A.2})$$

is conserved. With the time-dependent adiabatic eigenstates $|\chi_a^\sigma\rangle$ defined by Eq. (2.43) we can expand the time-dependent Kohn-Sham orbitals in the orthonormal basis $|\chi_a^\sigma(t)\rangle$:

$$|\psi^{j\sigma}(t)\rangle = \sum_{a=1}^{\infty} c_a^{j\sigma}(t) |\chi_a^\sigma(t)\rangle \quad (\text{A.3})$$

with the coefficients

$$\boxed{c_a^{j\sigma}(t) = \langle \chi_a^\sigma(t) | \psi^{j\sigma}(t) \rangle}. \quad (\text{A.4})$$

Inserting (A.3) into (A.2), the total number of electrons is determined by

$$N_e^\sigma = \sum_{j=1}^{N_e^\sigma} \sum_{a=1}^{\infty} |c_a^{j\sigma}|^2 = \sum_{a=1}^{\infty} n_a^\sigma \quad (\text{A.5})$$

with the occupation numbers

$$n_a^\sigma = \sum_{j=1}^{N_e^\sigma} |c_a^{j\sigma}|^2. \quad (\text{A.6})$$

In the ground state only the lowest orbitals $|\chi_a^\sigma(t)\rangle$ with $a = 1 \dots N_e^\sigma$ are occupied, which allows us to define the number of excited electrons as:

$$\boxed{N_{exc}^\sigma = N_e^\sigma - \sum_{a=1}^{N_e^\sigma} n_a^\sigma}. \quad (\text{A.7})$$

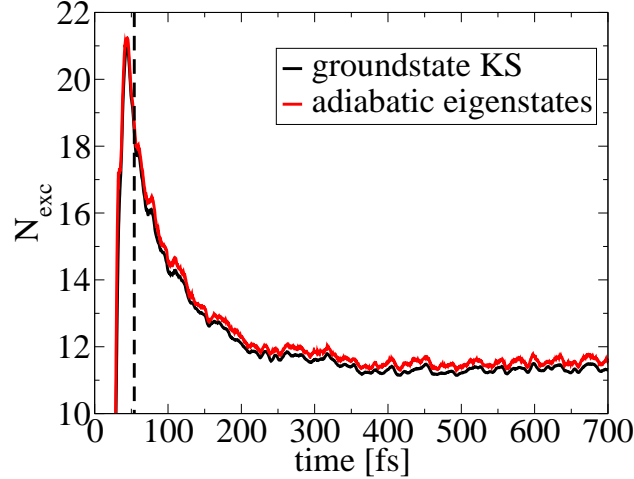


Figure A.1: Comparison of the number of excited electrons N_{exc} calculated with the groundstate Kohn-Sham functions (black) and the adiabatic eigenstates (red). The calculation is done for the excitation of C_{60} with a laser pulse ($\lambda = 370$ nm, $I = 3.3 \cdot 10^{13} \frac{W}{cm^2}$, $\tau = 27$ fs) as a function of time.

The time-dependent Kohn-Sham orbitals $|\psi^{j\sigma}(t)\rangle$ as well as the eigenstates $|\chi_a^\sigma(t)\rangle$ are expanded in a local basis set $\{\Phi_\alpha\}$ with N_b basis functions:

$$|\psi^{j\sigma}(t)\rangle = \sum_{\alpha=1}^{N_b} a_\alpha^{j\sigma}(t) |\Phi_\alpha(t)\rangle \quad (\text{A.8})$$

$$|\chi_a^\sigma(t)\rangle = \sum_{\alpha=1}^{N_b} b_\alpha^{a\sigma}(t) |\Phi_\alpha(t)\rangle. \quad (\text{A.9})$$

Inserting (A.8) and (A.9) into (A.4) the following equation for the occupation coefficients in basis expansion can be derived:

$$c_a^{j\sigma}(t) = \sum_{\alpha\beta} b_\alpha^{a\sigma*}(t) a_\beta^{j\sigma}(t) S_{\alpha\beta}(t) \quad (\text{A.10})$$

with the overlap matrix $S_{\alpha\beta}(t) = \langle \Phi_\alpha(t) | \Phi_\beta(t) \rangle$. Note, that due to the basis expansion the number of eigenstates $|\chi_a^\sigma(t)\rangle$ is also finite ($a = 1 \dots N_b$).

An alternative definition of the number of excited electrons is possible, using the ground-state Kohn-Sham functions at the current position $\mathbf{R}(t)$ (see Eq. (2.14)) rather than of the adiabatic eigenstates $|\chi_a^\sigma\rangle$. However, calculating the ground state is more time-consuming due to the iterative loop and the numerical results for N_{exc} are very similar for our purpose here. As an example, the resonant laser excitation of C_{60} is shown in Fig. A.1 (see Chapter 3.3). After the laser excitation more than 20 electrons of the 240 valence electrons are excited, but due to relaxation processes a decrease in time can be seen within 250 fs.

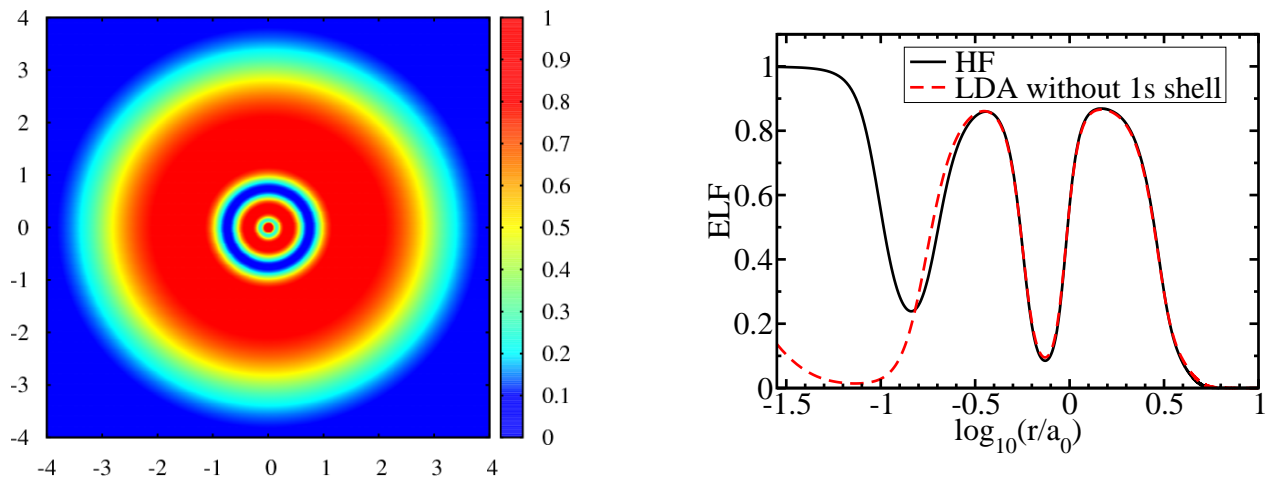


Figure A.2: (Left) Two dimensional ELF distribution of argon calculated with Hartree-Fock. The nucleus is located in the middle. (Right) Comparison of the radial ELF distribution of argon for a Hartree-Fock and a LDA calculation.

However, there is no big difference between the projection scheme using the adiabatic eigenfunctions resp. the ground state eigenfunctions.

A.2 Visualization of the electron dynamics

A.2.1 The electron localization function (ELF)

In physical chemistry different intuitive concepts emerged, i.e. the atomic shell structure or chemical bonding. In most cases the electron orbital picture will be used to describe the concepts. However, the orbitals are not uniquely defined and can be changed by any unitary transformation. The density itself provides no clue to the characteristics of the bonds in most cases. To distinguish covalent bonding types like single or double bond, the purpose is to find a suitable physical property, invariant against a unitary transformation of the orbitals. For example, the Laplacian of the density was successfully used to display the atomic shells in light atoms, but failed for heavier atoms beyond the period row with many more shells (see in ref. [57]). A basic concept in chemistry is the electron pairing of electrons with opposite spin and was introduced by Lewis in 1916. However, the electron density itself does not show any features of such bonding. For atoms/molecules in the ground state a electron localization function was suggested by Becke [57]. A time-dependent version was proposed in [241, 242] with an additional term depending on the current density. To define the electron localization function, a formula was derived for the probability to find an electron with equal spin near a reference electron sitting at position \mathbf{r} and time t :

$$D_{\sigma}(\mathbf{r}, t) = \sum_{i=1}^{N_{\sigma}^e} |\nabla \phi_{i\sigma}(\mathbf{r}, t)|^2 - \frac{1}{4} \frac{(\nabla \rho_{\sigma}(\mathbf{r}, t))^2}{\rho_{\sigma}(\mathbf{r}, t)} - \frac{j_{\sigma}^2(\mathbf{r}, t)}{\rho_{\sigma}(\mathbf{r}, t)} \quad (\text{A.11})$$

with the spin density ρ_σ and the spin current density

$$\mathbf{j}_\sigma(\mathbf{r}, t) = \frac{1}{2i} \sum_{i=1}^{N_e^\sigma} [\phi_{i\sigma}^*(\mathbf{r}, t) \nabla \phi_{i\sigma}(\mathbf{r}, t) - \phi_{i\sigma}(\mathbf{r}, t) \nabla \phi_{i\sigma}^*(\mathbf{r}, t)]. \quad (\text{A.12})$$

The electron localization function is defined by an inverse transformation as

$$f_{ELF}(\mathbf{r}, t) = \frac{1}{1 + \left(\frac{D_\sigma(\mathbf{r}, t)}{D_\sigma^0(\mathbf{r}, t)} \right)^2} \quad (\text{A.13})$$

with kinetic energy density of a homogeneous electron gas

$$D_\sigma^0(\mathbf{r}, t) = \frac{3}{5} (6\pi)^{\frac{2}{3}} \rho_\sigma^{\frac{5}{3}} \quad (\text{A.14})$$

as the reference system. According to the definition the dimensionless electron localization function is restricted to values $0 \leq f_{ELF}(\mathbf{r}, t) \leq 1$. The upper limit $f_{ELF}(\mathbf{r}, t) = 1$ corresponds to perfect localization, whereas $f_{ELF}(\mathbf{r}, t) = \frac{1}{2}$ corresponds to the electron-gas-like pair probability.

We have tested the ELF implementation with the noble gas argon. The results, depicted in Fig. A.2, are in good agreement with the values in the literature [57]. The 3 shells ($ELF \approx 1$) can be identified easily (red color in the 2D plot). The Hartree-Fock and the LDA calculation do not show big differences as expected since it is known that the influence of the chosen method is small. Only the first shell can not be displayed in the LDA result, because we have used the frozen core approximation for the 1s electrons and excluded these electrons from the ELF calculation.

A.2.2 The dimers N_2 and O_2

For the molecules the structure of the ELF is more complicated, resulting in a more difficult interpretation. However, arguments have been developed to distinguish bonding types based on the topological analysis of the ELF in 3D [58, 243]. The gradient field and the scalar ELF itself are used to find different types of attractors, f-localization domains, core resp. valence basins as well as basin populations. All these are used to define bonding types. As a first example we show some results for the dimer nitrogen N_2 . The triple bond in nitrogen is characterized by the maximum of the ELF between the nuclei (Fig. A.3). As one can see on the right part, the density does not show such a pronounced increase. The ELF distribution of oxygen (O_2) is plotted in Fig. A.4. It differs remarkably from the nitrogen dimer, since the electronic structure is a triplet state with the highest occupied orbital related to π symmetry.

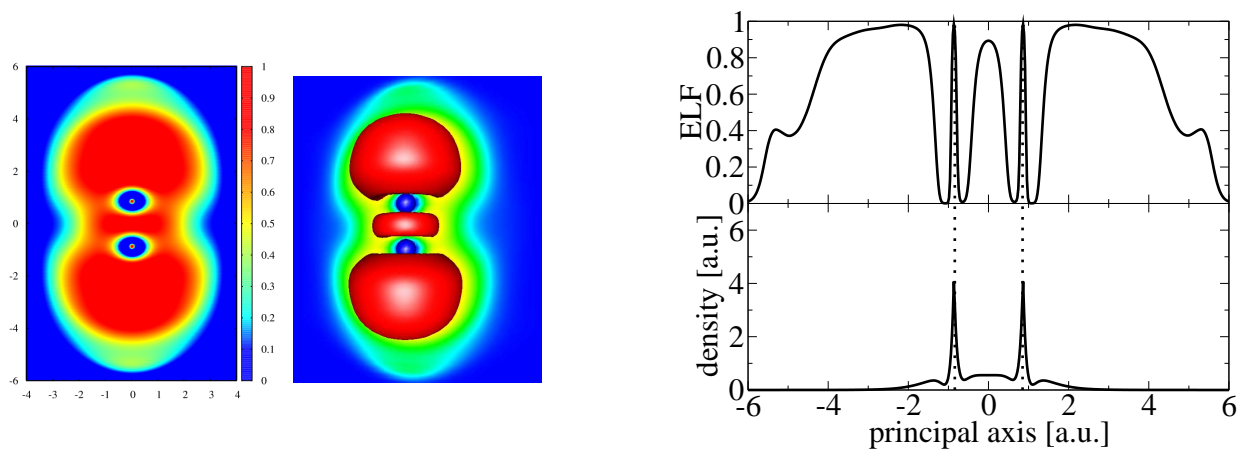


Figure A.3: (Left) Two dimensional ELF distribution of N₂ and the isosurface for $f_{ELF} = 0.75$ (colored in red) calculated with LDA. The vertical axis is the principal axis of the dimer and the origin (0,0) is the bond midpoint. (Right) Cut of the ELF and the density along the principal axis. The dashed lines indicate the position of the nuclei.

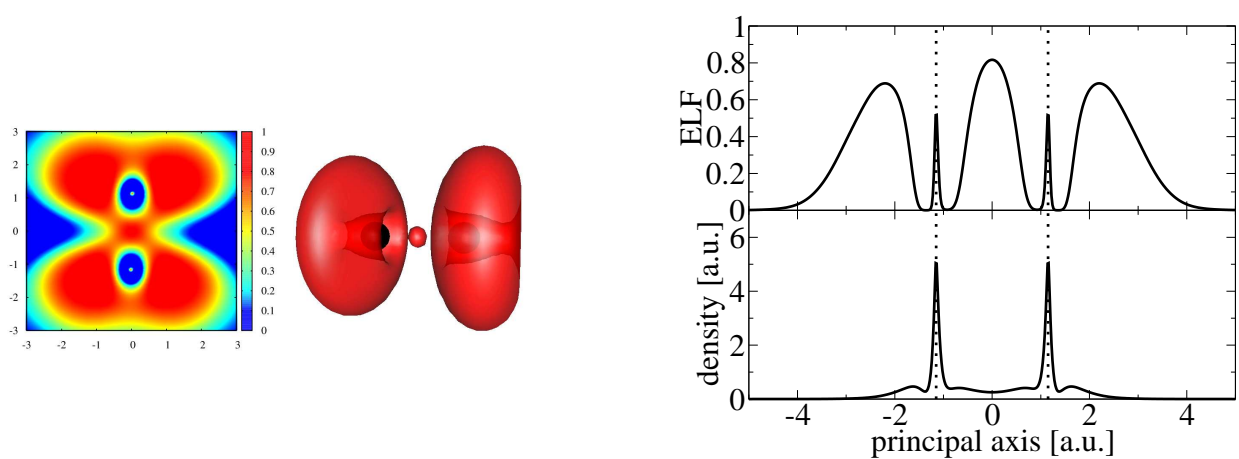


Figure A.4: (Left) The same as in Figure A.3 for O₂

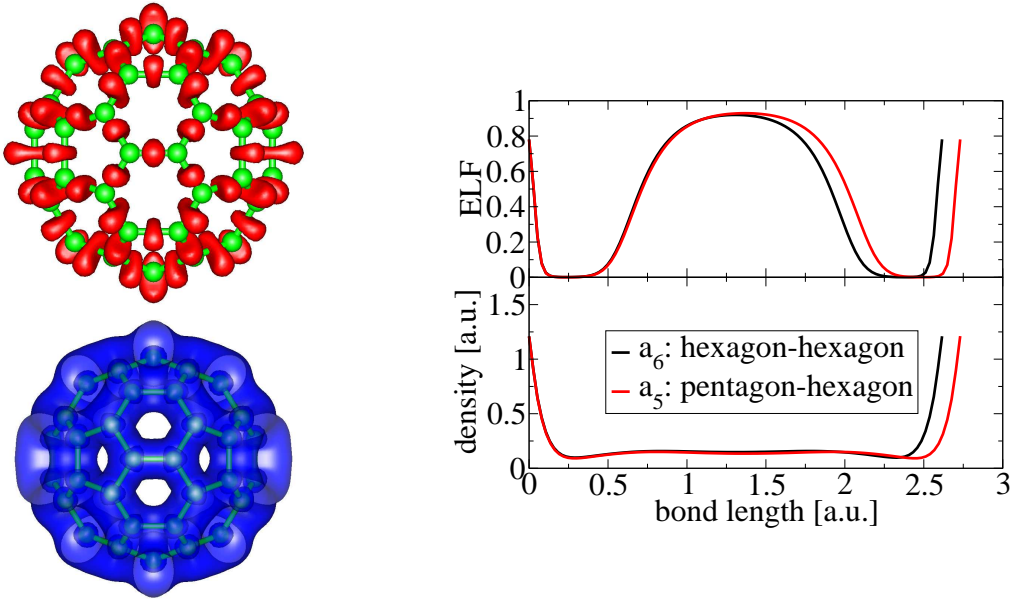


Figure A.5: (Left) The isosurfaces of C_{60} for $f_{ELF} = 0.8$ (red) and $f_{ELF} = 0.5$ (blue) (C_{60} -cage in green). (Right) Cut of the ELF and of the density between two carbon atoms for the a_5 and a_6 bond.

A.2.3 The C_{60} molecule

C_{60} is a non-aromatic molecule with 180 σ and 60 π electrons. In C_{60} two different bonds exist: 30 pentagonal edge bonds a_5 (double bonds) and 60 hexagon-hexagon edge bonds a_6 (single bonds) with different bond length. In Figure A.5 the isosurface for $f_{ELF} = 0.8$ is displayed. The highest electron localization is concentrated between the carbon atoms as expected. Furthermore, it is elongated in radial direction. The ELF isosurface for both bonds is very similar but with some smaller volume for the pentagonal edge bond. In the 1D plot of Fig. A.5 also no remarkable differences of the electron localization respectively of the density can be seen between the two bonding types. This has also been found in other calculations using a grid-based implementation for the td-DFT method [242].

So far, only examples of the electronic ground state have been presented. Now, we show a time-dependent example of the laser-induced dynamics of the electrons with moving nuclei. The laser parameters correspond to a resonant excitation as used in Chapter 3.3.3 and excite the breathing mode. As one can see, the electron structure will be changed due to the laser excitation (Fig. A.6). Finally (snapshot at $t = 56$ fs) the electron localization is also concentrated outside the cage above the carbon atoms, indicating the weakened or totally broken double bonds.

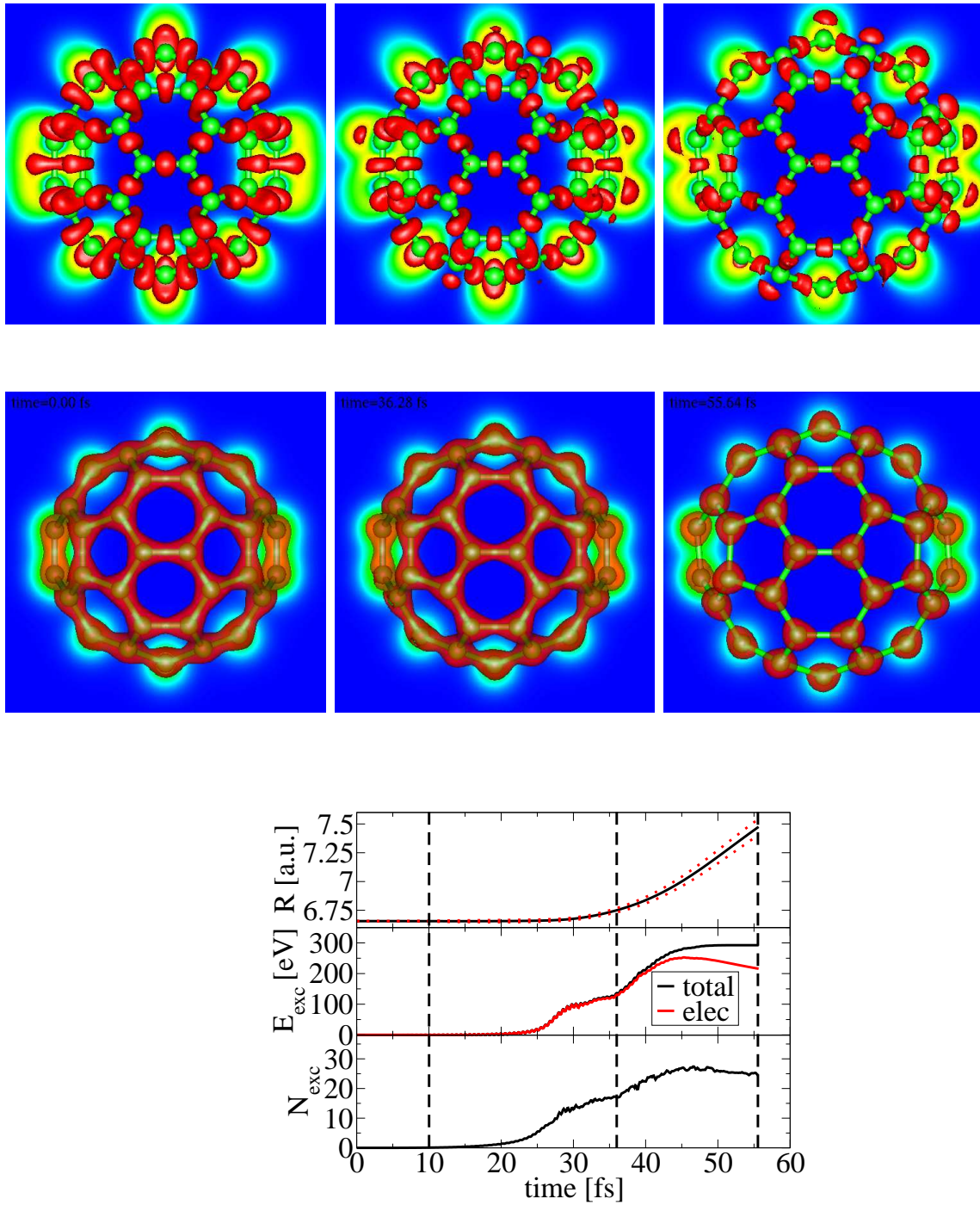


Figure A.6: Electronic excitation of C₆₀ with a blue, resonant laser ($T = 27$ fs). The laser polarization direction is from lower left to upper right. Snapshots of the distribution in a plane resp. isosurface for the ELF ($f_{ELF} = 0.8$) (first row), and of the electron density (second row) for a time $t = 0$ fs (left), $t = 36$ fs (middle) and $t = 56$ fs (right). (Bottom) Radius, total and electronic excitation energy and number of excited electrons as a function of time. The broken lines indicate the time of the snapshots.

B

B.1 Normal mode analysis

Definition of the normal modes

Suppose, we have a molecular system with the total energy

$$E = E_{kin} + V(\vec{x}) \quad (\text{B.1})$$

with the kinetic energy of the nuclei

$$E_{kin} = \sum_{i=1}^{3N} \frac{m_i}{2} \dot{x}_i^2 \quad (\text{B.2})$$

and the electronic ground state potential V depending on the nuclear positions $\vec{x} = (x_1, \dots, x_{3N})$ of N nuclei. For small displacements, $\vec{x} = \vec{x}_0 + \vec{y}$, near the energetical minimum configuration (\vec{x}_0) the potential V can be approximated by a Taylor series truncated at the second order term

$$V(\vec{x}_0 + \vec{y}) \approx V(\vec{x}_0) + \sum_{ij} \frac{\partial^2 V(\vec{x})}{\partial x_i \partial x_j} \Big|_{\vec{x}=\vec{x}_0} y_i y_j. \quad (\text{B.3})$$

By scaling the positions $\tilde{y}_i = \sqrt{m_i} y_i$ the masses m_i vanish in the kinetic energy term. Then, by solving the eigenvalue problem

$$\sum_j \mathcal{V}_{ij} \xi_{nj} = \omega_n^2 \xi_{ni} \quad (\text{B.4})$$

with $\mathcal{V}_{ij} = \frac{\partial^2 V(\vec{x})}{\partial x_i \partial x_j} \Big|_{\vec{x}_0} \frac{1}{\sqrt{m_i m_j}}$ we get the vibrational eigenmodes $\vec{\xi}_n$ with the eigenfrequencies ω_n ($n = 1 \dots 3N$). The most time-consuming task is the calculation of the symmetric Hessian matrix \mathcal{V}_{ij} . It needs the ground state energies for at least $4 \frac{3N(3N+1)}{2}$ positions if we use the simple four point algorithm for the (mixed) second partial derivative:

$$\frac{\partial^2 V(\vec{x})}{\partial x_i \partial x_j} \approx \frac{V(x_i + h, x_j + h) + V(x_i - h, x_j - h) - V(x_i + h, x_j - h) - V(x_i - h, x_j + h)}{4h} \quad (\text{B.5})$$

In principle, a further reduction of the number of matrix elements is possible if additional molecular symmetries would be taken into account. This means for C_{60} with 180 degrees of freedom that more than 65000 ground state energies had to be computed.

For a nonlinear molecule the first six eigenmodes with the lowest eigenfrequencies near zero are related to the translation and the rotation of the entire system. The remaining $3N - 6$ eigenmodes are the inner vibrational modes which we are interested in.

Decomposition of the kinetic energy

To investigate the vibrational excitation of a molecule a criterion must be chosen to quantify the strength of the distinct eigenmodes. Therefore, we switch from the cartesian coordinates x_i to the eigenmode coordinates η_n . The transformation

$$\eta_n = \sum_i U_{in} \sqrt{m_i} (x_i - x_{i0}) \quad (\text{B.6})$$

is performed by virtue of the unitary matrix U ($U^+ = U^{-1}$) composed of the eigenmode vectors $\vec{\xi}_n$, defined in (B.4):

$$U = \left(\vec{\xi}_1 \dots \vec{\xi}_{3N} \right). \quad (\text{B.7})$$

The elements of $\vec{\eta}$ are the amplitudes of the different eigenmodes with respect to the equilibrium position.

The potential energy itself is only a suitable quantity for small displacements from the equilibrium position. In that case we can distinguish the potential energy for each eigenmode V_n and the total potential energy is given by

$$V(\vec{\eta}) = V(\vec{\eta}_0) + \sum_n V_n = V(\vec{\eta}_0) + \sum_n \frac{\omega_n^2}{2} \eta_n^2 \quad (\text{B.8})$$

But the potential energy cannot be decomposed into the normal modes for larger amplitudes, where the harmonic approximation fails and coupling between the normal modes occurs due to higher order terms (Eq. (B.3)). In contrast, due to the quadratic velocity dependence, the kinetic energy of the nuclei E_{kin} can always be expanded as a sum over the normal modes

$$E_{kin} = \sum_n E_{vib}^n \quad (\text{B.9})$$

with the kinetic energy of the n th vibrational eigenmode

$$E_{vib}^n = \frac{\dot{\eta}_n^2}{2}. \quad (\text{B.10})$$

The kinetic energy E_{kin} without the three translational and three rotational modes is called the vibrational energy E_{vib} .

In the molecular dynamics calculations the system is often strongly deformed and far away from the equilibrium state. Therefore, we employ the kinetic energy of the eigenmodes to analyze the vibrational excitations. The approach was applied successfully for the investigation of the vibrational relaxation in charged and electronically excited C_{60} by Zhang and coworkers [185, 186, 188].

The vibrational mode analysis is done by transforming the cartesian coordinates used in the molecular dynamics calculations to the vibrational coordinates with Eq. (B.6) and calculating the kinetic energy E_{vib}^n of each vibrational mode with Eq. (B.10).

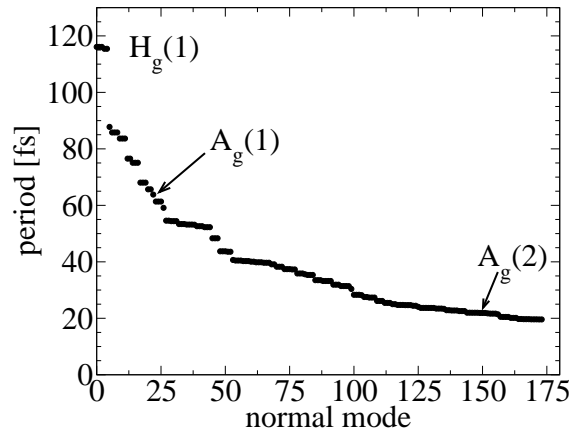


Figure B.1: The periods for all vibrational modes of C_{60} .

B.2 Normal modes of C_{60}

The buckyball molecule has 174 intramolecular modes with a wide range of vibrational periods T between 20 fs and 120 fs. A general survey can be found in section 11 in the book of Dresselhaus [165] where the modes are categorized by their symmetry properties.

In Figure B.1 we show the vibrational spectrum calculated with our DFT code. Various kinds of modes can be distinguished, which are not easy to depict due to their complicated structure. A selection of the eigenvectors of all modes with A_g and H_g symmetry is shown in Fig. B.2. The modes with the highest symmetry are the (non-degenerate) A_g modes: the so-called breathing mode $A_g(1)$ ($T=67$ fs) and the pentagonal pinch mode $A_g(2)$ ($T=20$ fs). In both cases the icosahedral symmetry I_h of the equilibrium configuration is conserved. The breathing mode changes only the C_{60} diameter, whereas the pentagonal pinch mode $A_g(2)$ involves tangential atomic displacements leading to a change of the ratio of the pentagonal edge length to the hexagon-hexagon edge length.

The H_g modes have much lower symmetry and are degenerate with five eigenvectors for the same eigenfrequency. The most interesting mode is the oblate-prolate mode $H_g(1)$ with the lowest frequency (experimental value in [223, 244]: $273 \text{ cm}^{-1} \equiv 122 \text{ fs}$). Some snapshots of one of the five $H_g(1)$ vibrations are displayed in Figure B.3 showing the change between the oblate and prolate geometry. More generally, two groups of vibrational modes can be distinguished. The vibrational modes with radial atomic displacements have in most cases smaller frequencies than modes with tangential atomic displacements.

The periods of the vibrational modes, calculated here with the local density approximation (LDA) and the minimal basis expansion, will be underestimated by 5 % in comparison with the experimental results. For instance, we find a period of 64 fs (exp.: 67 fs) resp. 116 fs (exp.: 122 fs) [223, 244] for the breathing mode $A_g(1)$ resp. for the oblate-prolate mode $H_g(1)$.

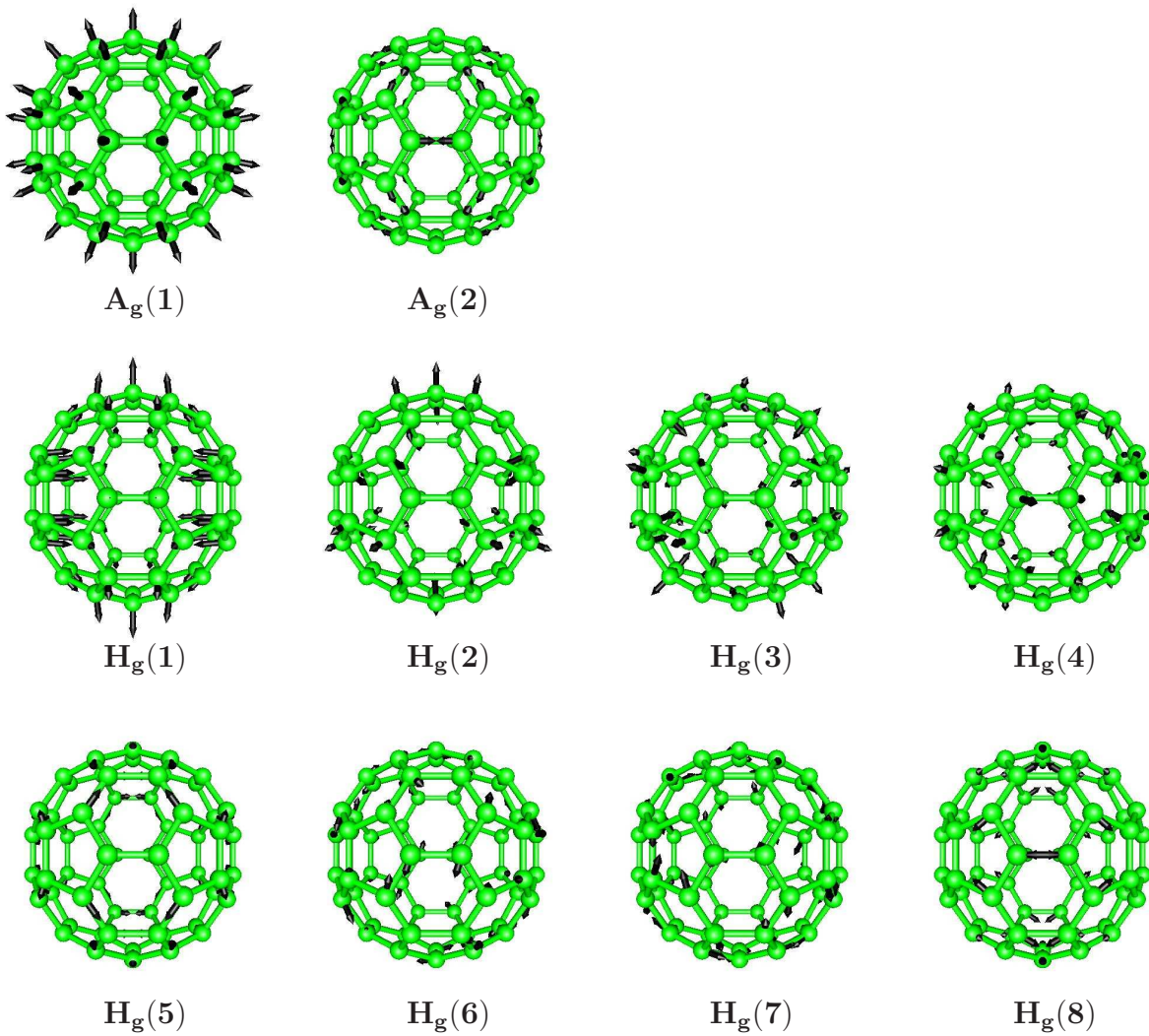


Figure B.2: The eigenvectors with A_g and H_g symmetry of C_{60} indicated by arrows for the nuclear displacements. Note, that the H_g modes shown here are not uniquely defined due to the fivefold degeneracy.

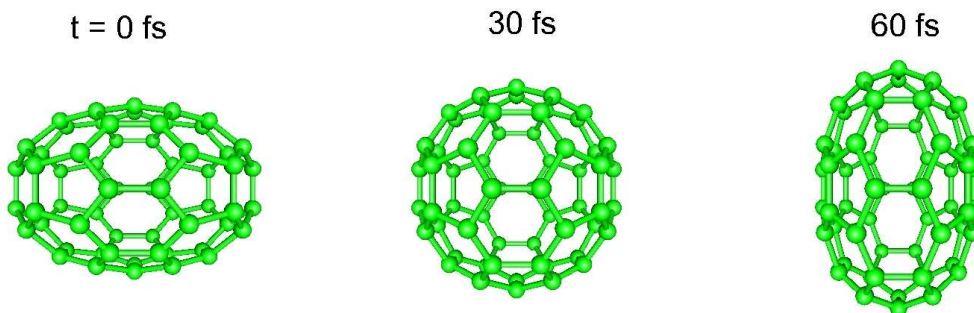


Figure B.3: The oblate-prolate mode $H_g(1)$ of C_{60} for half a cycle.

C

C.1 Classical trajectory model for asymmetrical fullerene-fullerene collisions

Here, we show the analytical results for the classical trajectory model consisting of two interacting springs (see Eq. (4.8)). For the exit channel the EOMs cannot be solved analytically. Therefore, the full dynamics is always calculated numerically using a Runge-Kutta method. However, in the entrance channel the interaction is harmonic which allows us to solve the problem in principle analytically. Here, we show the general case of two different springs as well as the special case of identical springs which corresponds to $C_{60} + C_{70}$ resp. $C_{60} + C_{60}$ collisions.

In the entrance channel the EOMs (Eq. (4.8)) are reduced to a system of coupled linear ordinary differential equations (ODE) of second order ($\omega^2 = \frac{k}{\mu}, \omega_i^2 = \frac{k_i}{\mu_i}$):

$$\ddot{R} = -\omega^2 (R - 0.5 (D_1 + D_2) - d_{int}) \quad (C.1)$$

$$\ddot{D}_i = -\omega_i^2 (D_i - D_i^0) + \omega^2 (R - 0.5 (D_1 + D_2) - d_{int}) \quad (C.2)$$

or to linear ODEs of first order:

$$\underbrace{\frac{d}{dt} \begin{pmatrix} R \\ D_1 \\ D_2 \\ \dot{R} \\ \dot{D}_1 \\ \dot{D}_2 \end{pmatrix}}_{\mathbf{x}} = \underbrace{\begin{pmatrix} 0 & 0 & 0 & 1 & 0 & 0 \\ 0 & 0 & 0 & 0 & 1 & 0 \\ 0 & 0 & 0 & 0 & 0 & 1 \\ -\omega^2 & \frac{\omega^2}{2} & \frac{\omega_2^2}{2} & 0 & 0 & 0 \\ \omega^2 & -(\omega_1^2 + \frac{\omega^2}{2}) & -\frac{\omega^2}{2} & 0 & 0 & 0 \\ \omega^2 & -\frac{\omega^2}{2} & -(\omega_2 + \frac{\omega^2}{2}) & 0 & 0 & 0 \end{pmatrix}}_A \begin{pmatrix} R \\ D_1 \\ D_2 \\ \dot{R} \\ \dot{D}_1 \\ \dot{D}_2 \end{pmatrix}. \quad (C.3)$$

The transformation $R \rightarrow R - 0.5 (D_1 + D_2) + d_{int}$, $D_i \rightarrow D_i - D_i^0$ has been performed to eliminate the inhomogenities in (C.1),(C.2). The eigenvalue equation $|A - \lambda I| = 0$ gives

$$\lambda^6 + (\omega_1^2 + \omega_2^2 + 2 \omega^2) \lambda^4 + \left(\omega_1^2 \omega_2^2 + \frac{3}{2} \omega^2 (\omega_1^2 + \omega_2^2) \right) \lambda^2 + \omega_1^2 \omega_2^2 \omega^2 = 0. \quad (C.4)$$

By means of the substitution $\Lambda = \lambda^2$ we arrive at a cubic equation which can be solved by using Cardano's equations. Three pairs of pure imaginary eigenvalues $\lambda_{j\pm} = \pm i \Omega_j$ with the eigenfrequencies Ω_j ($\Omega_j \in \mathbb{R}_+$) occur. Even the analytical solution of the eigenvalues is very complicated and not shown here. In principle, the eigenvectors can be calculated with the help of the eigenfrequencies Ω_j . However, the analytical solution of the eigenvectors

will be even more complicated. Alternatively, we calculate the eigenfrequencies Ω_j and the eigenvector matrix U numerically. With an exponential ansatz for the general solution using the eigenvalues $\lambda_{j\pm}$ and the eigenvectors $\mathbf{U}_{j\pm}$ the problem can be solved.

For the initial conditions (going back to the original coordinates)

$$R(0) = d_{int} + 0.5 (D_1^0 + D_2^0), \quad \dot{R}(0) = v \quad (\text{C.5})$$

$$D_1(0) = D_1^0, \quad \dot{D}_1(0) = 0 \quad (\text{C.6})$$

$$D_2(0) = D_2^0, \quad \dot{D}_2(0) = 0 \quad (\text{C.7})$$

the final solution is given by

$$R(t) = \sum_{j=1}^3 a_j \sin(\Omega_j t) + d_{int} + 0.5 (D_1^0 + D_2^0), \quad (\text{C.8})$$

$$D_1(t) = \sum_{j=1}^3 b_j \sin(\Omega_j t) + D_1^0, \quad (\text{C.9})$$

$$D_2(t) = \sum_{j=1}^3 c_j \sin(\Omega_j t) + D_2^0. \quad (\text{C.10})$$

The coefficients $\mathbf{A}_j = (a_j, b_j, c_j)$ are defined as

$$\mathbf{A}_j = -2 \Im(c_j) \Re(\tilde{\mathbf{U}}_{j+}) \quad j = 1 \dots 3 \quad (\text{C.11})$$

with $\tilde{\mathbf{U}}_{j+}$ composed from the first three components of the eigenvector \mathbf{U}_{j+} and with the coefficient c_j defined by the system of linear equations for the initial conditions:

$$\mathbf{x}_0 = U \mathbf{c} \quad (\text{C.12})$$

$$\text{with } \mathbf{x}_0 = (0, 0, 0, v, 0, 0)^T. \quad (\text{C.13})$$

C.2 Analytical solution for symmetrical fullerene-fullerene collisions

In the case of identical springs ($\omega \equiv \omega_1 = \omega_2$, $D^0 \equiv D_1^0 = D_2^0$), the problem is simplified by setting $D \equiv D_1 = D_2$. The system of ODEs is reduced to four equations

$$\frac{d}{dt} \begin{pmatrix} R \\ D \\ \dot{R} \\ \dot{D} \end{pmatrix} = \underbrace{\begin{pmatrix} 0 & 0 & 1 & 0 \\ 0 & 0 & 0 & 1 \\ -\omega^2 & \omega^2 & 0 & 0 \\ \omega^2 & -(\omega^2 + \omega_1^2) & 0 & 0 \end{pmatrix}}_A \begin{pmatrix} R \\ D \\ \dot{R} \\ \dot{D} \end{pmatrix}. \quad (\text{C.14})$$

As in the general case mentioned above, the eigenvalue equation $|A - \lambda I| = 0$ has to be solved, which gives the fundamental eigenfrequencies of the system ($\kappa = \frac{k_1}{k} = \frac{\omega_1^2}{\omega^2}$):

$$\Omega_{1/2} = \omega \sqrt{\kappa + 1 \pm \sqrt{\kappa^2 + 1}} = \omega f_{1/2}(\kappa). \quad (\text{C.15})$$

The solution $R(t), D(t)$ for the initial conditions

$$R(0) = D^0 + d_{int}, \quad \dot{R}(0) = v \quad (\text{C.16})$$

$$D(0) = D^0, \quad \dot{D}(0) = 0 \quad (\text{C.17})$$

is

$$R(t) = v \sum_{j=1}^2 a_j \sin(\Omega_j t) + D^0 + d_{int}, \quad (\text{C.18})$$

$$D(t) = v \sum_{j=1}^2 b_j \sin(\Omega_j t) + D^0 \quad (\text{C.19})$$

with the amplitudes

$$a_{1/2} = \frac{1}{2 f_{1/2}(\kappa)} \left(1 \mp \frac{\kappa}{\sqrt{\kappa^2 + 1}} \right), \quad (\text{C.20a})$$

$$b_{1/2} = \mp \frac{1}{2 f_{1/2}(\kappa)} \frac{1}{\sqrt{\kappa^2 + 1}}. \quad (\text{C.20b})$$

Bibliography

- [1] P. Agostini, F. Fabre, G. Mainfray, G. Petite, and N. K. Rahman, *Free-Free Transitions Following Six-Photon Ionization of Xenon Atoms*, Phys. Rev. Lett. **42(17)**, 1127–1130 (Apr 1979).
- [2] A. Giusti-Suzor, X. He, O. Atabek, and F. H. Mies, *Above-threshold dissociation of H_2^+ in intense laser fields*, Phys. Rev. Lett. **64(5)**, 515–518 (Jan 1990).
- [3] X. F. Li, A. L’Huillier, M. Ferray, L. A. Lompré, and G. Mainfray, *Multiple-harmonic generation in rare gases at high laser intensity*, Phys. Rev. A **39(11)**, 5751–5761 (Jun 1989).
- [4] T. Zuo and A. D. Bandrauk, *Charge-resonance-enhanced ionization of diatomic molecular ions by intense lasers*, Phys. Rev. A **52(4)**, R2511–R2514 (Oct 1995).
- [5] C. Horn, M. Wollenhaupt, M. Krug, T. Baumert, R. de Nalda, and L. Bañares, *Adaptive control of molecular alignment*, Phys. Rev. A **73(3)**, 031401 (2006).
- [6] Robert J. Levis, Getahun M. Menkir, and Herschel Rabitz, *Selective Bond Dissociation and Rearrangement with Optimally Tailored, Strong-Field Laser Pulses*, Science **292(5517)**, 709–713 (2001).
- [7] M. Lezius, S. Dobosz, D. Normand, and M. Schmidt, *Explosion Dynamics of Rare Gas Clusters in Strong Laser Fields*, Phys. Rev. Lett. **80(2)**, 261–264 (Jan 1998).
- [8] A. Bandrauk, Y. Fujimura, and R. J. Gordon, editors, *Laser Control and Manipulation of Molecules*, ACS Symposium Series Vol. 821, Oxford University, Oxford (2002).
- [9] A. H. Zewail, editor, *Femtochemistry: Ultrafast Dynamics of the Chemical Bond*, Vols. 1 and 2, World Scientific, Singapore (1994).
- [10] A. Stolow, *Femtosecond Time-resolved Photoelectron Spectroscopy of Polyatomic Molecules*, Ann. Rev. Phys. Chem. **54**, 89 (2003).
- [11] Atsushi Iwamae, Akiyoshi Hishikawa, and Kaoru Yamanouchi, *Extraction of molecular dynamics in intense laser fields from mass-resolved momentum imaging maps: application to Coulomb explosion of NO*, Journal of Physics B: Atomic, Molecular and Optical Physics **33(2)**, 223–240 (2000).

- [12] Etienne Gagnon, Predrag Ranitovic, Xiao-Min Tong, C. L. Cocke, Margaret M. Murnane, Henry C. Kapteyn, and Arvinder S. Sandhu, *Soft X-ray-Driven Femtosecond Molecular Dynamics*, *Science* **317(5843)**, 1374–1378 (2007).
- [13] J. Gagnon, Kevin F. Lee, D. M. Rayner, P. B. Corkum, and V. R. Bhardwaj, *Coincidence imaging of polyatomic molecules via laser-induced Coulomb explosion*, *Journal of Physics B: Atomic, Molecular and Optical Physics* **41(21)**, 215104 (6pp) (2008).
- [14] Richard S. Judson and Herschel Rabitz, *Teaching lasers to control molecules*, *Phys. Rev. Lett.* **68(10)**, 1500–1503 (Mar 1992).
- [15] A. Assion, T. Baumert, M. Bergt, T. Brixner, B. Kiefer, V. Seyfried, M. Strehle, and G. Gerber, *Control of Chemical Reactions by Feedback-Optimized Phase-Shaped Femtosecond Laser Pulses*, *Science* **282(5390)**, 919–922 (1998).
- [16] K. Ohmori, *Wave-Packet and Coherent Control Dynamics*, *Ann. Rev. Phys. Chem.* **60**, 487 (2009).
- [17] M. Wollenhaupt V. Engel and T. Baumert, *Femtosecond Laser Photoelectron Spectroscopy on Atoms and Small Molecules: Prototype Studies in Quantum Control*, *Ann. Rev. Phys. Chem.* **56**, 25 (2005).
- [18] Markus Drescher, Michael Hentschel, Reinhard Kienberger, Gabriel Tempea, Christian Spielmann, Georg A. Reider, Paul B. Corkum, and Ferenc Krausz, *X-ray Pulses Approaching the Attosecond Frontier*, *Science* **291(5510)**, 1923–1927 (2001).
- [19] J. Itatani, J. Levesque, D. Zeidler, Hiromichi Niikura, H. Pepin, J. C. Kieffer, P. B. Corkum, and D. M. Villeneuve, *Tomographic imaging of molecular orbitals*, *Nature* **432**, 867 (2004).
- [20] S. Kanai, S. Minemoto, and H. Sakai, *Quantum interference during high-order harmonic generation from aligned molecules*, *Nature* **435**, 470 (2005).
- [21] Edward S. Smyth, Jonathan S. Parker, and K.T. Taylor, *Numerical integration of the time-dependent Schrödinger equation for laser-driven helium*, *Computer Physics Communications* **114(1-3)**, 1 – 14 (1998).
- [22] J. S. Parker, K. J. Meharg, G. A. McKenna, and K. T. Taylor, *Single-ionization of helium at Ti:Sapphire wavelengths: rates and scaling laws*, *Journal of Physics B: Atomic, Molecular and Optical Physics* **40(10)**, 1729–1743 (2007).
- [23] Martin Winter, Rüdiger Schmidt, and Uwe Thumm, *Multidimensional quantum-beat spectroscopy: Towards the complete temporal and spatial resolution of the nuclear dynamics in small molecules*, *Phys. Rev. A* **80(3)**, 031401 (Sep 2009).

-
- [24] Martin Winter, Rüdiger Schmidt, and Uwe Thumm, *Quantum-beat analysis of the rotational-vibrational dynamics in D_2^+* , accepted by New J. Phys. (2010).
- [25] D. C. Rapaport, *The Art of Molecular Dynamics Simulations*, Cambridge University Press (2001).
- [26] T. Helgaker, P. Jørgensen, and J. Olsen, editors, *Molecular electronic-structure theory*, John Wiley & Sons LTD, Chichester (2000).
- [27] Tsuyoshi Kato and Hirohiko Kono, *Time-dependent multiconfiguration theory for electronic dynamics of molecules in intense laser fields: A description in terms of numerical orbital functions*, The Journal of Chemical Physics **128(18)**, 184102 (2008).
- [28] E. Runge and E. K. U. Gross, *Density-Functional Theory for Time-Dependent Systems*, Phys. Rev. Letters **52**, 997 (1984).
- [29] U. Saalmann and R. Schmidt, *Non-adiabatic Quantum Molecular Dynamics, Basic Formalism and Case Study*, Z. Phys. D **38**, 153 (1996).
- [30] R. Car and M. Parrinello, *Unified Approach for Molecular Dynamics and Density-Functional Theory*, Phys. Rev. Lett. **55**, 2471 (1985).
- [31] U. Saalmann and R. Schmidt, *Excitation and Relaxation in Atom-Cluster Collisions*, Phys. Rev. Lett. **80**, 3213 (1998).
- [32] T. Kunert and R. Schmidt, *Excitation and Fragmentation Mechanisms in Ion-Fullerene Collisions*, Phys. Rev. Lett. **86**, 5258 (2001).
- [33] O. Knospe, J. Jellinek, U. Saalmann, and R. Schmidt, *Charge transfer in cluster-atom collisions*, Eur. Phys. J. D **5**, 1 (1999).
- [34] Z. Roller-Lutz, Y. Wang, H. O. Lutz, U. Saalmann, and R. Schmidt, *Strong temperature dependence of laser-enhanced charge transfer in collisions of sodium clusters with sodium atoms*, Phys. Rev. A **59**, R2555 (1999).
- [35] O. Knospe, J. Jellinek, U. Saalmann, and R. Schmidt, *Charge transfer and fragmentation in cluster-atom collisions*, Phys. Rev. A **61**, 022715–1 (2000).
- [36] M. Ehrich, U. Werner, H. O. Lutz, T. Kaneyasu, K. Ishii, K. Okuno, and U. Saalmann, *Simultaneous charge polarization and fragmentation of N_2 molecules in slow keV collisions with Kr_8^+ ions*, Phys. Rev. A **65(3)**, 030702 (Feb 2002).
- [37] J. A. Fayeton, M. Barat, J. C. Brenot, H. Dunet, Y. J. Picard, U. Saalmann, and R. Schmidt, *Detailed experimental and theoretical study of collision-induced dissociation of Na_2^+ ions on He and H_2 targets at keV energies*, Phys. Rev. A **57(2)**, 1058–1068 (Feb 1998).

-
- [38] R. Schmidt, O. Knospe, and U. Saalman, *Adiabatic and non-adiabatic cluster collisions*, Nuovo Cimento A **110**, 1201 (1997).
- [39] Ulf Saalman and Rüdiger Schmidt, *Non-adiabatic quantum molecular dynamics: Reaction mechanisms in atom-cluster collisions*, volume 500, pp. 720–724, AIP (2000).
- [40] F. Grossmann, U. Saalman, and R. Schmidt, *Laser- and collision-induced nonadiabatic wave-packet dynamics in sodium molecules*, Annalen der Physik **9**, 785 (2000).
- [41] R. Schmidt, *Classical description of heavy-ion collisions*, Sov. J. Part. Nucl. **13**, 501 (1982).
- [42] R. V. Jolos, R. Schmidt, and J. Teichert, *One-body collisions and classical collective dynamics in heavy-ion reactions*, Nuclear Physics A **429(1)**, 139 – 172 (1984), ISSN 0375-9474.
- [43] T. Kunert and R. Schmidt, *Non-adiabatic quantum molecular dynamics: General formalism and case study H_2^+ in strong laser fields.*, Eur. Phys. J. D **25**, 15 (2003).
- [44] Thomas Kunert, *Time-dependent density functional theory in basis expansion*, Ph.D. thesis, TU Dresden (2003).
- [45] Mathias Uhlmann, *Dynamics of diatomic molecules in intense laser fields*, Ph.D. thesis, TU Dresden (2005).
- [46] M. Uhlmann, T. Kunert, and R. Schmidt, *Error of finite basis expansions in time-dependent calculations of atom-laser interaction*, Phys. Rev. E **72**, 036704 (2005).
- [47] M. Uhlmann, T. Kunert, and R. Schmidt, *Non-adiabatic quantum molecular dynamics: ionization of many-electron systems*, J. Phys. B **39**, 2989 (2006).
- [48] M. Uhlmann, T. Kunert, F. Grossmann, and R. Schmidt, *Mixed classical-quantum approach to excitation, ionization, and fragmentation of H_2^+ in intense laser fields*, Phys. Rev. A **67**, 013413 (2003).
- [49] M. Uhlmann, T. Kunert, and R. Schmidt, *Molecular alignment of fragmenting H_2^+ and H_2 in strong laser fields*, Phys. Rev. A **72**, 045402 (2005).
- [50] T. Kunert, F. Grossmann, and R. Schmidt, *Nonadiabatic dynamics of ethylene in femtosecond laser-pulses*, Phys. Rev. A **72**, 023422 (2005).
- [51] J. Handt et. al., *Density Functional Study of the Orientation-Dependent Ionization of N_2 and O_2 by intense laser fields*, to be published.
- [52] J. Handt, T. Kunert, and R. Schmidt, *Fragmentation and cis-trans isomerization of diimide in fs laser-pulses*, Chem. Phys. Lett. **428**, 220 (2006).

-
- [53] T. Laarmann, I. Shchatsinin, A. Stalmashonak, M. Boyle, N. Zhavoronkov, J. Handt, R. Schmidt, C.P. Schulz, and I.V. Hertel, *Control of Giant Breathing Motion in C₆₀ with Temporally Shaped Laser Pulses*, Phys. Rev. Lett. **98**, 058302 (2007).
- [54] Rüdiger Schmidt and Jan Handt, *Laser- and Collision-Induced Collective Vibrational Excitations in Fullerenes*, volume 1197, pp. 144–151, AIP Conference Proceedings (2009).
- [55] J. Handt and R. Schmidt, *A two-dimensional classical trajectory model for fullerene-fullerene collisions*, to be published.
- [56] J. Handt and R. Schmidt, in preparation.
- [57] A. D. Becke and K. E. Edgecombe, *A simple measure of electron localization in atomic and molecular systems*, J. Chem. Phys. **92**, 5397 (1990).
- [58] B. Silvi and A. Savin, *Classification of chemical bonds based on topological analysis of electron localization functions*, Nature **371**, 683 (1994).
- [59] N. F. Mott and H. S. W. Massey, *The Theory of Atomic Collisions*, Oxford University Press, Oxford (1965).
- [60] D. Marx, *An Introduction to Ab Initio Molecular Dynamics Simulations*, in J. Groten-dorst, S. Bluegel, and D. Marx, editors, *Computational Nanoscience: Do it Yourself!*, volume 31, p. 195, John von Neumann Institute for Computing, NIC Series (2006).
- [61] D. Marx and J. Hutter, *Ab Initio Molecular Dynamics: Basic Theory And Advanced Methods*, Cambridge University Press (2009).
- [62] G. Cicotti, D. Frenkel, and I. R. McDonald, *Simulation of Liquids and Solids*, North-Holland, Amsterdam (1987).
- [63] M. P. Allen and D. J. Tildesley, *Computer Simulation of Liquids*, Clarendon Press, Oxford (1987).
- [64] W. Kohn and L. J. Sham, *Self-Consistent Equations Including Exchange and Correlation Effects*, Phys. Rev. **140**, A1133 (1965).
- [65] P. Ehrenfest, *Bemerkung über die angenäherte Gültigkeit der klassischen Mechanik innerhalb der Quantenmechanik*, Z. Phys. **45**, 455 (1927).
- [66] N. L. Doltsinis and D. Marx, *First principles molecular dynamics involving excited states and nonadiabatic transitions*, J. Theor. Comput. Chem. **1**, 319 (2002).

- [67] N. L. Doltsinis, *Nonadiabatic Dynamics: Mean-Field and Surface Hopping*, in J. Grotenndorst, D. Marx, and A. Muramatsu, editors, *Quantum Simulations of Complex Many-Body Systems: From Theory To Algorithms, Lecture Notes*, volume 10, p. 377, John von Neumann Institute for Computing, NIC Series (2002).
- [68] J. C. Tully and R. K. Preston, *Trajectory Surface Hopping Approach to Nonadiabatic Molecular Collisions: The Reaction of H^+ with D_2* , J. Chem. Phys. **55**, 562 (1971).
- [69] J. C. Tully, *Molecular dynamics with electronic transitions*, J. Chem. Phys. **93**, 1061 (1990).
- [70] D. S. Sholl and J. C. Tully, *A generalized surface hopping method*, J. Chem. Phys. **109**, 7702 (1998).
- [71] N. L. Doltsinis and D. Marx, *Nonadiabatic Car-Parrinello Molecular Dynamics*, Phys. Rev. Lett. **88**, 166402–1 (2002).
- [72] Irmgard Frank, Jürg Hutter, Dominik Marx, and Michele Parrinello, *Molecular dynamics in low-spin excited states*, J. Chem. Phys. **108**(10), 4060–4069 (1998).
- [73] C. F. Craig, W. R. Duncan, and O. V. Prezhdo, *Trajectory Surface Hopping in the Time-Dependent Kohn-Sham Approach for Electron-Nuclear Dynamics*, Phys. Rev. Lett. **95**, 163001 (2005).
- [74] O. V. Prezhdo and P. J. Rossky, *Mean-field molecular dynamics with surface hopping*, J. Chem. Phys. **107**, 825 (1997).
- [75] G. A. Worth, H.-D. Meyer, and L. S. Cederbaum, *Multidimensional dynamics involving a conical intersection: Wavepacket calculations using the MCTDH method*, in W. Domcke, D. R. Yarkony, and H. Koppel, editors, *Conical Intersections*, pp. 573–607, World Scientific Co., Singapore (2004).
- [76] H.-D. Meyer, F. Gatti, and G. A. Worth, editors, *Multidimensional Quantum Dynamics: MCTDH Theory and Applications*, Wiley-VCH, Weinheim (2009).
- [77] Oriol Vendrell, Michael Brill, Fabien Gatti, David Lauvergnat, and Hans-Dieter Meyer, *Full dimensional (15-dimensional) quantum-dynamical simulation of the protonated water-dimer III: Mixed Jacobi-valence parametrization and benchmark results for the zero point energy, vibrationally excited states, and infrared spectrum*, The Journal of Chemical Physics **130**(23), 234305 (2009).
- [78] Oriol Vendrell, Fabien Gatti, and Hans-Dieter Meyer, *Full dimensional (15 dimensional) quantum-dynamical simulation of the protonated water-dimer IV: Isotope effects in the infrared spectra of $D(D_2O)_2^+$, $H_2(O)_2^+$, and $D(H_2O)_2^+$ isotopologues*, J. Chem. Phys. **131**(3), 034308 (2009).

-
- [79] D. Marx and M. Parrinello, *Ab initio path-integral molecular dynamics: basic ideas*, J. Chem. Phys. **104**, 4077 (1996).
- [80] D. Marx, M. E. Tuckerman, J. Hutter, and M. Parrinello, *The nature of the hydrated excess in water*, Nature **397**, 601 (1999).
- [81] M. Ben-Nun and T.J. Martínez, *Nonadiabatic molecular dynamics: Validation of the multiple spawning method for a multidimensional problem*, J. Chem. Phys. **108**, 7244 (1998).
- [82] Eric J. Heller, *Frozen Gaussians: A very simple semiclassical approximation*, J. Chem. Phys. **75(6)**, 2923–2931 (1981).
- [83] Frank Grossmann, *A Hierarchy of Semiclassical Approximations Based on Gaussian Wavepackets*, Comments At. Mol. Phys. **34**, 141 (1999).
- [84] A. Toniolo, C. Ciminelli, M. Persico, and T. J. Martínez, *Simulation of the photodynamics of azobenzene on its first excited state: Comparison of full multiple spawning and surface hopping treatments*, The Journal of Chemical Physics **123(23)**, 234308 (2005).
- [85] Aaron M. Virshup, Chutintorn Punwong, Taras V. Pogorelov, Beth A. Lindquist, Chaehyuk Ko, and T. J. Martínez, *Photodynamics in Complex Environments: Ab Initio Multiple Spawning Quantum Mechanical/Molecular Mechanical Dynamics*, J. Phys. Chem. B **113**, 3280 (2009).
- [86] Hanneli R. Hudock, Benjamin G. Levine, Alexis L. Thompson, Helmut Satzger, D. Townsend, N. Gador, S. Ullrich, Albert Stolow, and T. J. Martínez, *Ab Initio Molecular Dynamics and Time-Resolved Photoelectron Spectroscopy of Electronically Excited Uracil and Thymine*, J. Phys. Chem. A **111**, 8500 (2007).
- [87] Joshua D. Coe and T. J. Martinez, *Ab initio multiple spawning dynamics of excited state intramolecular proton transfer: the role of spectroscopically dark states*, Molecular Physics **106**, 537545 (2008).
- [88] T. J. Martínez, *Insights for Light-Driven Molecular Devices from Ab Initio Multiple Spawning Excited-State Dynamics of Organic and Biological Chromophores*, Acc. Chem. Res. **39**, 119 (2006).
- [89] I. Horenko, C. Salzmann, B. Schmidt, and C. Schütte, *Quantum-classical Liouville approach to molecular dynamics: Surface hopping Gaussian phase-space packets*, J. Chem. Phys. **117**, 11075 (2002).

- [90] Illia Horenko, Burkhard Schmidt, and Christof Schütte, *A theoretical model for molecules interacting with intense laser pulses: The Floquet-based quantum-classical Liouville equation*, J. Chem. Phys. **115**(13), 5733–5743 (2001).
- [91] T. Kreibich, R. van Leeuwen, and E. K. U. Gross, *Multicomponent density-functional theory for electrons and nuclei*, Phys. Rev. A **78**, 022501 (2008).
- [92] P. Hohenberg and W. Kohn, *Inhomogeneous Electron Gas*, Phys. Rev. **136**, B864 (1964).
- [93] O. Knospe, R. Schmidt, and G. Seifert, *Adiabatic Cluster Dynamics*, in W. L. Hase, editor, *Advances In Classical Trajectory Methods*, volume 4 of *Molecular Dynamics Of Clusters, Surfaces, Liquids, And Interfaces*, p. 153, JAI PRESS INC. (1999).
- [94] O. Knospe and R. Schmidt, *Fullerene Collisions*, in J. Jellinek, editor, *Theory of Atomic and Molecular Clusters*, p. 111, Springer: Berlin (1999).
- [95] R. Ehlich, E. E. B. Campbell, O. Knospe, and R. Schmid, *Collisional dynamics of C₆₀ with noble-gas-atoms studied by molecular dynamics with empirical two- and three-body forces*, Z. Physik D **28**, 153 (1993).
- [96] R. Ehlich, O. Knospe, and R. Schmidt, *Molecular dynamics studies of inelastic scattering and fragmentation in collisions of with rare-gas atoms*, Journal of Physics B: Atomic, Molecular and Optical Physics **30**(23), 5429–5449 (1997).
- [97] Donald W. Brenner, *Empirical potential for hydrocarbons for use in simulating the chemical vapor deposition of diamond films*, Phys. Rev. B **42**(15), 9458–9471 (Nov 1990).
- [98] Donald W. Brenner, *Erratum: Empirical potential for hydrocarbons for use in simulating the chemical vapor deposition of diamond films*, Phys. Rev. B **46**(3), 1948 (Jul 1992).
- [99] J. Schulte and G. Seifert, *DFT-LDA molecular dynamics of molecular collision processes*, Chemical Physics Letters **221**(3-4), 230 – 236 (1994).
- [100] G. Seifert and J. Schulte, *On the formation of deuterium fullerene complexes in collisions of C₆₀ with D₂*, Physics Letters A **188**(4-6), 365 – 370 (1994).
- [101] R. Schmidt, G. Seifert, and H. O. Lutz, *Cluster-cluster collisions. I. Reaction channels - fusion, deep inelastic and quasielastic collisions*, Physics Letters A **158**(5), 231 – 236 (1991).
- [102] G. Seifert, R. Schmidt, and H. O. Lutz, *Cluster-cluster collisions. II. Cluster molecules – a stable state of matter?*, Physics Letters A **158**(5), 237 – 241 (1991).

-
- [103] O. Knospe, A. V. Glotov, G. Seifert, and R. Schmidt, *Theoretical studies of atomic cluster-cluster collisions*, J. Phys. B: At. Mol. Opt. Phys. **29**, 5163 (1996).
- [104] R. Schmidt, J. Schulte, O. Knospe, and G. Seifert, *$C_{60}+C_{60}$ collisions. I. Multifragmentation and collective flow effects*, Phys. Lett. A **194**, 101 (1994).
- [105] J. Schulte, O. Knospe, G. Seifert, and R. Schmidt, *$C_{60}+C_{60}$ collisions. II. Mass and angular distributions*, Phys. Lett. A **198**, 51 (1995).
- [106] M.A.L. Marques, Alberto Castro, George F. Bertsch, and Angel Rubio, *octopus: a first-principles tool for excited electron-ion dynamics*, Comput. Phys. Commun. **151**, 60–78 (2003).
- [107] Alberto Castro, Heiko Appel, Micael Oliveira, Carlo A. Rozzi, Xavier Andrade, Florian Lorenzen, M. A. L. Marques, E. K. U. Gross, and Angel Rubio, *octopus: a tool for the application of time-dependent density functional theory*, Phys. Stat. Sol. B **243**, 2465–2488 (2006).
- [108] Y. Kawashita, T. Nakatsukasa, and K. Yabana, *Time-dependent density-functional theory simulation for electron – ion dynamics in molecules under intense laser pulses*, Journal of Physics: Condensed Matter **21(6)**, 064222 (5pp) (2009).
- [109] D. Dundas, *Accurate and efficient non-adiabatic quantum molecular approach for laser-matter interactions*, J. Phys. B: Mol. Opt. Phys. **37**, 2883 (2004).
- [110] <http://www.dymol.org/>.
- [111] J. P. Perdew and Y. Wang, *Accurate and simple analytic representation of the electron-gas correlation-energy*, Phys. Rev. B **45**, 13244 (1992).
- [112] Konstantin N. Kudin, Gustavo E. Scuseria, and Eric Cancès, *A black-box self-consistent field convergence algorithm: One step closer*, The Journal of Chemical Physics **116(19)**, 8255–8261 (2002).
- [113] C. W. Ueberhuber, *Numerical Computation*, volume 2, Springer (1997).
- [114] P. Nordling and P. Fritzson, *Parallelization of the CVODE ordinary differential equation solver with applications to rolling bearing simulation*, Lect. notes comput. sc. **919**, 892 (1995).
- [115] M. J. DeWitt, E. Wells, and R. R. Jones, *Ratiometric Comparison of Intense Field Ionization of Atoms and Diatomic Molecules*, Phys. Rev. Lett. **87**, 153001–1 (2001).

-
- [116] Domagoj Pavičić, Kevin F. Lee, D. M. Rayner, P. B. Corkum, and D. M. Villeneuve, *Direct Measurement of the Angular Dependence of Ionization for N_2 , O_2 , and CO_2 in Intense Laser Fields*, Physical Review Letters **98(24)**, 243001 (2007).
- [117] X. M. Tong, Z. X. Zhao, and C. D. Lin, *Theory of molecular tunneling ionization*, Phys. Rev. A **66**, 033402–1 (2002).
- [118] L. V. Keldysh, *Ionization in the field of a strong electromagnetic wave*, Zh. Eksp. Teor. Fiz. **47**, 1945 (1964).
- [119] F. H. M. Faisal, *Multiple absorption of laser photons by atoms*, Journal of Physics B: Atomic and Molecular Physics **6(4)**, L89–L92 (1973).
- [120] Howard R. Reiss, *Effect of an intense electromagnetic field on a weakly bound system*, Phys. Rev. A **22(5)**, 1786–1813 (1980).
- [121] H. R. Reiss, *Complete Keldysh theory and its limiting cases*, Phys. Rev. A **42(3)**, 1476–1486 (1990).
- [122] J. Muth-Böhm, A. Becker, and F. H. M. Faisal, *Suppressed Molecular Ionization for a Class of Diatomics in Intense Femtosecond Laser Fields*, Phys. Rev. Lett. **85**, 2280 (2000).
- [123] A. Jaroń-Becker, A. Becker, and F. H. M. Faisal, *Ionization of N_2 , O_2 , and linear carbon clusters in a strong laser pulse*, Phys. Rev. A **69**, 023410 (2004).
- [124] T. K. Kjeldsen and L. B. Madsen, *Strong-field ionization of diatomic molecules and companion atoms: Strong-field approximation and tunneling theory including nuclear motion*, Phys. Rev. A **71**, 023411 (2005).
- [125] T. D. G. Walsh, F. A. Ilkov, J. E. Decker, and S. L. Chin, *The tunnel ionization of atoms, diatomic and triatomic molecules using intense $10.6 \mu\text{m}$ radiation*, Journal of Physics B: Atomic, Molecular and Optical Physics **27(16)**, 3767–3779 (1994).
- [126] C. Guo, M. Li, J. P. Nibarger, and G. N. Gibson, *Single and double ionization of diatomic molecules in strong laser fields*, Phys. Rev. A **58(6)**, R4271–R4274 (1998).
- [127] D. Dundas and J. M. Rost, *Molecular effects in the ionization of N_2 , O_2 , and F_2 by intense laser fields*, Phys. Rev. A **71**, 013421 (2005).
- [128] X. Chu and S. I. Chu, *Role of the electronic structure and multielectron responses in ionization mechanisms of diatomic molecules in intense short-pulse lasers: An all-electron ab initio study*, Phys. Rev. A **70**, 061402(R) (2004).

-
- [129] S. I. Chu, *Recent development of self-interaction-free time-dependent density functional theory for nonperturbative treatment of atomic and molecular multiphoton processes in intense laser fields*, J. Chem. Phys. **123**, 062207 (2005), invited article for a special issue of Journal of Chemical Physics.
- [130] I. V. Litvinyuk, K. F. Lee, P. W. Dooley, D. M. Rayner, D. M. Villeneuve, and P. B. Corkum, *Alignment-Dependent Strong Field Ionization of Molecules*, Phys. Rev. Lett. **90**, 233003–1 (2003).
- [131] A. S. Alnaser, S. Voss, X-M. Tong, C. Maharjan, P. Ranitovic, B. Ulrich, T. Osipov, B. Shan, Z. Chang, and C. L. Cocke, *Effects Of Molecular Structure on Ion Disintegration Patterns In Ionization of O₂ and N₂ by short laser pulses*, Phys. Rev. Lett **93**, 113003–1 (2004).
- [132] S. Voss, A. S. Alnaser, X-M. Tong, C. Maharjan, P. Ranitovic, B. Ulrich, B. Shan, Z. Chang, C. D. Lin, and C. L. Cocke, *High resolution kinetic energy release spectra and angular distributions from double ionization of nitrogen and oxygen by short laser pulses*, J. Phys. B **37**, 4239 (2004).
- [133] K.P. Huber and G. Herzberg, editors, *Molecular Spectra and Molecular Structure*, IV. Constants of Diatomic Molecules, Van Nostrand Reinhold Co. (1979).
- [134] R. M. Dreizler and E. K. U. Gross, *Density Functional Theory, An Approach to the Quantum Many-Body Problem*, Springer-Verlag (1990).
- [135] R. M. Dreizler and E. K. U. Gross, *Density Functional Theory II, Relativistic and Time Dependent Extensions, Topics in Current Chemistry 181*, Springer-Verlag (1996).
- [136] P. J. Linstrom and W. G. Mallard, editors, *NIST Chemistry WebBook, NIST Standard Reference Database Number 69*, National Institute of Standards and Technology, Gaithersburg MD, 20899; <http://webbook.nist.gov> (2010).
- [137] A. S. de Wijn, M. Lein, and S. Kümmel, *Strong-field ionization in time-dependent density functional theory*, EPL (Europhysics Letters) **84(4)**, 43001 (6pp) (2008).
- [138] G. Lagmago Kamta and A. D. Bandrauk, *Imaging electron molecular orbitals via ionization by intense femtosecond pulses*, Phys. Rev. A **74(3)**, 033415 (2006).
- [139] F. C. De Schryver, S. De Feyter, and G. Schweitzer, editors, *Femtochemistry*, Wiley-VCH (2001).
- [140] Robert R. Birge, *Nature of the primary photochemical events in rhodopsin and bacteriorhodopsin*, Biochimica et Biophysica Acta (BBA) - Bioenergetics **1016(3)**, 293 – 327 (1990).

- [141] R. W. Schoenlein, L. A. Peteanu, R. A. Mathies, and C. V. Shank, *The first step in vision: Femtosecond isomerization of rhodopsin*, *Science* **254**, 412 (1991).
- [142] Yusheng Dou and Roland E. Allen, *Detailed dynamics of a complex photochemical reaction: Cis-trans photoisomerization of stilbene*, *J. Chem. Phys.* **119**, 10658 (2003).
- [143] T. Nägele, R. Hoche, W. Zinth, and J. Wachtveitl, *Femtosecond photoisomerization of cis-azobenzene*, *Chem. Phys. Letters* **272**, 489 (1997).
- [144] M. J. Cook, A. Nygard, Z. Wang, and D. A. Russell, *An evanescent field driven mono-molecular layer photoswitch: coordination and release of metallated macrocycles*, *Chem. Comm.* p. 1056 (2002).
- [145] K. M. Tait, J. A. Parkinson, S. P. Bates, W. J. Ebenezer, and A. C. Jones, *The novel use of NMR spectroscopy with in situ laser irradiation to study azo photoisomerisation*, *J. Photochem. and Photobiol. A: Chem.* **154**, 179 (2003).
- [146] A. Natansohn and P. Rochon, *Photoinduced Motions in Azo-Containing Polymers*, *Chem. Rev.* **102**, 4139 (2002).
- [147] T. Hugel, N. B. Holland, A. Cattani, L. Moroder, M. Seitz, and H. E. Gaub, *Single-Molecule Optomechanical Cycle*, *Science* **296**, 1103 (2002).
- [148] W. Domcke and G. Stock, *Theory of Ultrafast Nonadiabatic Excited-State Processes and their Spectroscopic Detection in Real Time*, *Adv. Chem. Phys.* **100**, 1 (1997).
- [149] S. Hahn and G. Stock, *Quantum-mechanical modeling of the femtosecond isomerization of rhodopsin*, *J. Phys. Chem.* **104**, 1146 (2000).
- [150] T. Schultz, J. Quenneville, B. Levine, A. Toniolo, T. Martinez, S. Lochbrunner, M. Schmitt, J. P. Schaffer, M. Zgierski, and A. Stolow, *Mechanism and Dynamics of Azobenzene Photoisomerization*, *J. Am. Chem. Soc.* **125**, 8098 (2003).
- [151] M. Ben-Nun and T.J. Martínez, *Photodynamics of ethylene: ab initio studies of conical intersections*, *Chem. Phys.* **259**, 237 (2000).
- [152] Ivano Tavernelli, Ute F. Röhrig, and Ursula Rothlisberger, *Molecular dynamics in electronically excited states using time-dependent density functional theory.*, *Molecular Physics* **103(6-8)**, 963 – 981 (2005).
- [153] T. H. Dunning, Jr., *Gaussian basis sets for use in correlated molecular calculations. I. The atoms boron through neon and hydrogen*, *J. Chem. Phys.* **90**, 1007 (1989).
- [154] R. A. Back, C. Willis, and D. A. Ramsay, *The near-ultraviolet absorption spectrum of diimide. a re-examination*, *Can. J. Chem.* **56**, 1575 (1978).

-
- [155] H. R. Tang, *Direct Detection of Aqueous Diazene: Its UV Spectrum and Concerted Dismutation*, Inorg. Chem. **33**, 1388 (1994).
- [156] M. Carlotti, J. W. C. Johns, and A. Trombetti., *The n_5 Fundamental Bands of N_2H_2 and N_2D_2* , Can. J. Chem. **52**, 340 (1974).
- [157] H. J. A. Jensen, P. Jørgensen, and T. Helgaker, *The Ground-State Potential Energy Surface of Diazene*, J. Am. Chem. Soc. **109**, 2895 (1987).
- [158] J. Andzelm, C. Sosa, and R. A. Eades, *Theoretical Study of Chemical Reactions Using Density Functional Methods with Nonlocal Corrections*, J. Phys. Chem. **97**, 4664 (1993).
- [159] C. Angeli, R. Cimiraglia, and H. Hofmann, *On the competition between the inversion and rotation mechanisms in the cis-trans thermal isomerization of diazene*, Chem. Phys. Letters **259**, 276 (1996).
- [160] K. Kim, I. Shavitt, and J. E. Del Bene, *Theoretical study of the di-imide (N_2H_2) molecule in ground and $n \rightarrow \pi^*$ excited states*, J. Chem. Phys. **96**, 7573 (1992).
- [161] X. Pu, Ning-Bew Wong, Ge Zhou, Jiande Gu, and Anmin Tian, *Substituent effects on the trans/cis isomerization and stability of diazenes*, Chem. Phys. Lett. **408**, 101 (2005).
- [162] M. J. Frisch, G. W. Trucks, H. B. Schlegel, G. E. Scuseria, M. A. Robb, J. R. Cheeseman, V. G. Zakrzewski, J. A. Montgomery, Jr., R. E. Stratmann, J. C. Burant, S. Dapprich, J. M. Millam, A. D. Daniels, K. N. Kudin, M. C. Strain, O. Farkas, J. Tomasi, V. Barone, M. Cossi, R. Cammi, B. Mennucci, C. Pomelli, C. Adamo, S. Clifford, J. Ochterski, G. A. Petersson, P. Y. Ayala, Q. Cui, K. Morokuma, D. K. Malick, A. D. Rabuck, K. Raghavachari, J. B. Foresman, J. Cioslowski, J. V. Ortiz, A. G. Baboul, B. B. Stefanov, G. Liu, A. Liashenko, P. Piskorz, I. Komaromi, R. Gomperts, R. L. Martin, D. J. Fox, T. Keith, M. A. Al-Laham, C. Y. Peng, A. Nanayakkara, C. Gonzalez, M. Challacombe, P. M. W. Gill, B. Johnson, W. Chen, M. W. Wong, J. L. Andres, C. Gonzalez, M. Head-Gordon, E. S. Replogle, and J. A. Pople, *Gaussian 98, Revision A.7*, Gaussian, Inc., Pittsburgh PA, 1998.
- [163] M. Klessinger and J. Michl, *Excited States and Photochemistry of Organic Molecules*, VCH (1995).
- [164] H. W. Kroto, J. R. Heath, S. C. O'Brien, R. F. Curl, and R. E. Smalley, *C_{60} : Buckminsterfullerene*, Nature **318**, 162 (1985).
- [165] M. S. Dresselhaus, G. Dresselhaus, and P. C. Eklund, *Science of Fullerenes and Carbon Nanotubes*, Academic Press (1996).

- [166] I. V. Hertel, H. Steger, J. de Vries, B. Weisser, C. Menzel, B. Kamke, and W. Kamke, *Giant plasmon excitation in free C_{60} and C_{70} molecules studied by photoionization*, Phys. Rev. Lett. **68**(6), 784–787 (Feb 1992).
- [167] G. F. Bertsch, A. Bulgac, D. Tomnek, and Y. Wang, *Collective plasmon excitations in C_{60} clusters*, Phys. Rev. Lett **67**, 2690 (1991).
- [168] D. Bauer, F. Ceccherini, A. Macchi, and F. Cornolti, *C_{60} in intense laser pulses: Nonlinear dipole response and ionization*, Phys. Rev. A **64**, 063203 (2001).
- [169] S. W. J. Scully, E. D. Emmons, M. F. Gharaibeh, R. A. Phaneuf, S. Schippers, A. Müller, H. S. Chakraborty, M. E. Madjet, and J. M. Rost, *Photoexcitation of a Volume Plasmon in C_{60} Ions*, Phys. Rev. Lett **94**, 065503 (2005).
- [170] M. E. Madjet, H. S. Chakraborty, J. M. Rost, and S. T. Manson, *Photoionization of C_{60} : a model study*, Journal of Physics B: Atomic, Molecular and Optical Physics **41**(10), 105101 (8pp) (2008).
- [171] V. R. Bhardwaj, P. B. Corkum, and D. M. Rayner, *Internal Laser-Induced Dipole Force at Work in C_{60} Molecule*, Phys. Rev. Lett. **91**, 203004 (2003).
- [172] V. R. Bhardwaj, P. B. Corkum, and D. M. Rayner, *Recollision during the High Laser Intensity Ionization of C_{60}* , Phys. Rev. Lett. **93**(4), 043001 (Jul 2004).
- [173] Thomas Brabec, Michel Côté, Paul Boulanger, and Lora Ramunno, *Theory of Tunnel Ionization in Complex Systems*, Phys. Rev. Lett. **95**(7), 073001 (Aug 2005).
- [174] A. Jaroń-Becker, A. Becker, and F. H. M. Faisal, *Saturated Ionization of Fullerenes in Intense Laser Fields*, Physical Review Letters **96**(14), 143006 (2006).
- [175] E. E. B. Campbell, K. Hansen, K. Hoffmann, G. Korn, M. Tchapyguine, M. Wittmann, and I. V. Hertel, *From Above Threshold Ionization to Statistical Electron Emission: The Laser Pulse-Duration Dependence of C_{60} Photoelectron Spectra*, Phys. Rev. Lett **84**, 2128 (2000).
- [176] I.V. Hertel, T. Laarmann, and C.P. Schulz, *Ultrafast excitation, ionization, and fragmentation of C_{60}* , volume 50 of *Advances In Atomic, Molecular, and Optical Physics*, pp. 219 – 286, Academic Press (2005).
- [177] M. Boyle, M. Hedén, C. P. Schulz, E. E. B. Campbell, and I. V. Hertel, *Two-color pump-probe study and internal-energy dependence of Rydberg-state excitation in C_{60}* , Phys. Rev. A **70**, 051201 (2004).

-
- [178] S. C. O'Brien, J. R. Heath, R. F. Curl, and R. E. Smalley, *Photophysics of buckminsterfullerene and other carbon cluster ions*, The Journal of Chemical Physics **88**(1), 220–230 (1988).
- [179] Chunhui Xu and Gustavo E. Scuseria, *Tight-binding molecular dynamics simulations of fullerene annealing and fragmentation*, Phys. Rev. Lett. **72**(5), 669–672 (Jan 1994).
- [180] Harald O. Jeschke, Martin E. Garcia, and J. A. Alonso, *Nonthermal fragmentation of C_{60}* , Chemical Physics Letters **352**(3-4), 154 – 162 (2002).
- [181] S. Díaz-Tendero, M. Alcamí, and F. Martín, *Coulomb Stability Limit of Highly Charged C_{60}^{q+} Fullerenes*, Phys. Rev. Lett. **95**(1), 013401 (Jun 2005).
- [182] Riadh Sahnoun, Katsunori Nakai, Yukio Sato, Hirohiko Kono, Yuichi Fujimura, and Motohiko Tanaka, *Theoretical investigation of the stability of highly charged C_{60} molecules produced with intense near-infrared laser pulses*, The Journal of Chemical Physics **125**(18), 184306 (2006).
- [183] Yukio Sato, Hirohiko Kono, Shiro Koseki, and Yuichi Fujimura, *Description of Molecular Dynamics in Intense Laser Fields by the Time-Dependent Adiabatic State Approach: Application to Simultaneous Two-Bond Dissociation of CO_2 and Its Control*, J. Am. Chem. Soc. **125**, 8019 (2003).
- [184] Chunhui Xu and Gustavo E. Scuseria, *Tight-binding molecular dynamics simulations of fullerene annealing and fragmentation*, Phys. Rev. Lett. **72**(5), 669–672 (Jan 1994).
- [185] G. P. Zhang, X. F. Zong, X. Sun, Thomas F. George, and Lakshmi N. Pandey, *Relaxation process of charge transfer in C_{60} : A normal mode analysis*, Physics Letters A **220**(4-5), 275 – 280 (1996).
- [186] G. P. Zhang, X. Sun, Thomas F. George, and Lakshmi N. Pandey, *Normal mode analysis for a comparative study of relaxation processes of charge transfer and photoexcitation in C_{60}* , The Journal of Chemical Physics **106**(15), 6398–6403 (1997).
- [187] G. P. Zhang, X. Sun, and T. F. George, *Laser-induced ultrafast dynamics in C_{60}* , Phys. Rev. B **68**, 165410 (2003).
- [188] G. P. Zhang and T. F. George, *Controlling Vibrational Excitations in C_{60} by Laser Pulse Durations*, Phys. Rev. Lett. **93**, 147401 (2004).
- [189] B. Torralva, T. Niehaus, M. Elstner, S. Suhai, T. Frauenheim, and R. E. Allen, *Response of C_{60} and C_n to ultrashort laser pulses*, Phys. Rev. B **64**, 153105 (2001).

- [190] K. P. Meletov, E. Liarokapis, J. Arvanitidis, K. Papagelis, D. Palles, G. A. Kourouklis, and S. Ves, *On the nature of the laser irradiation induced reversible softening of phonon modes in C_{60} single crystals*, Chemical Physics Letters **290(1-3)**, 125 – 130 (1998).
- [191] S. B. Fleischer, B. Pevzner, D. J. Dougherty, H. J. Zeiger, G. Dresselhaus, M. S. Dresselhaus, E. P. Ippen, and A. F. Hebard, *Coherent phonons in alkali metal-doped C_{60}* , Applied Physics Letters **71(19)**, 2734–2736 (1997).
- [192] Donald S. Bethune, Gerard Meijer, Wade C. Tang, and Hal J. Rosen, *The vibrational Raman spectra of purified solid films of C_{60} and C_{70}* , Chem. Phys. Lett. **174**, 219 (1990).
- [193] Donald S. Bethune, Gerard Meijer, Wade C. Tang, Hal J. Rosen, William G. Golden, Hajime Seki, Charles A. Brown, and Mattanjah S. de Vries, *Vibrational Raman and infrared spectra of chromatographically separated C_{60} and C_{70} fullerene clusters*, Chemical Physics Letters **179(1-2)**, 181 – 186 (1991).
- [194] C. S. Yannoni, P. P. Bernier, D. S. Bethune, G. Meijer, and J. R. Salem, *NMR determination of the bond lengths in C_{60}* , J. Am. Chem. Soc. **113**, 3190 (1991).
- [195] K. Hedberg and L. Hedberg, *Bond lengths in free molecules of buckminsterfullerene, C_{60} , from gas-phase electron diffraction.*, Science **254(5030)**, p410 (1991).
- [196] R.C. Haddon, L.E. Brus, and Krishnan Raghavachari, *Electronic structure and bonding in icosahedral C_{60}* , Chemical Physics Letters **125(5-6)**, 459 – 464 (1986).
- [197] Masa aki Ozaki and Akira Taahashi, *On electronic states and bond lengths of the truncated icosahedral C_{60} molecule*, Chemical Physics Letters **127(3)**, 242 – 244 (1986).
- [198] Henry Ajie, Marcos M. Alvarez, Samir J. Anz, Rainer D. Beck, Franq̄ois Diederich, K. Fostirooulos, Donald R. Huffman, Wolfgang Krätschmer, Yves Rubin, Kenneth E. Schriver, Dilip Sensharma, and Robert L. Whetten, *Characterization of the soluble all-carbon molecules C_{60} and C_{70}* , J. Phys. Chem. **94**, 8630–8633 (1990).
- [199] J. R. Heath, R. F. Curl, and R. E. Smalley, *The UV absorption spectrum of C_{60} (buckminsterfullerene): A narrow band at 3860 [A-ring]*, The Journal of Chemical Physics **87(7)**, 4236–4238 (1987).
- [200] G. P. Zhang and Thomas F. George, *Normal-mode selectivity in ultrafast Raman excitations in C_{60}* , Physical Review B (Condensed Matter and Materials Physics) **73(3)**, 035422 (2006).
- [201] S. Dexheimer and et al., *Ultrafast Phenomena VIII*, in J. L. Martin, A. Migus, G.A. Mourou, and A.H. Zewail, editors, *Springer Ser. Chem. Phys.*, volume 55, p. 81, Springer-Verlag, Berlin (1993).

-
- [202] H. Hohmann, C. Callegari, S. Furrer, D. Grosenick, E. E. B. Campbell, and I. V. Hertel, *Photoionization and Fragmentation Dynamics of C₆₀*, Phys. Rev. Lett **73**, 1919 (1994).
- [203] B. Feuerstein and U. Thumm, *Fragmentation of H₂⁺ in strong 800-nm laser pulses: Initial-vibrational-state dependence*, Physical Review A **67**(043405), 1–8 (2003).
- [204] E. E. B. Campbell and F. Rohmund, *Fullerene reactions*, Rep. Prog. Phys. **63**, 1061 (2000).
- [205] H. Shen, P. Hvelplund, D. Mathur, A. Bárány, H. Cederquist, N. Selberg, and D.C. Lorents, *Fullerene-fullerene collisions: Fragmentation and electron capture*, Phys. Rev. A **52**, 3847 (1995).
- [206] H. Bräuning, R. Trassl, A. Diehl, A. Theiß, E. Salzborn, A. A. Narits, and L. P. Presnyakov, *Resonant Electron Transfer in Collisions between Two Fullerene Ions*, Phys. Rev. Lett. **91**, 168301–1 (2003).
- [207] U. Kadhane, A. Kelkar, D. Misra, A. Kumar, and L. C. Tribedi, *Effect of giant plasmon excitations in single and double ionization of C₆₀ in fast heavy-ion collisions*, Phys. Rev. A **75**, 041201–1 (2007).
- [208] S. Cheng, H. G. Berry, W. Dunford, H. Esbensen, D. S. Gemmell, E. P. Kanter, and T. LeBrun, *Ionization and fragmentation of C₆₀ by highly charged, high-energy xenon ions*, Phys. Rev. A **54**, 3182 (1996).
- [209] F. Rohmund, E. B. Campbell, O. Knospe, G. Seifert, and R. Schmidt, *Collision Energy Dependence of Molecular Fusion and Fragmentation in C₆₀⁺ and C₆₀ Collisions*, Phys. Rev. Lett. **76**, 3289 (1996).
- [210] E. B. Campbell, A. V. Glotov, A. Lassesson, and R. D. Levine, *Cluster-cluster fusion*, C. R. Physique **3**, 341 (2002).
- [211] A. Glotov, O. Knospe, R. Schmidt, and E. B. Campbell, *Molecular fusion of fullerenes*, Eur. Phys. J. D **16**, 333 (2001).
- [212] D. H. Robertson, D. W. Brenner, and C. T. White, *Temperature-Dependent Fusion of Colliding C₆₀ Fullerenes from Molecular Dynamics Simulations*, J. Phys. Chem. **99**, 15721 (1995).
- [213] F. Rohmund, A. V. Glotov, K. Hansen, and E. B. Campbell, *Experimental studies of fusion and fragmentation of fullerenes*, J. Phys. B **29**, 5143 (1996).
- [214] R. Schmidt and H. O. Lutz, *Fusion and stability of colliding atomic nuclei, atomic clusters, and liquid droplets*, Phys. Rev. A **45**(11), 7981–7984 (Jun 1992).

- [215] Keivan Esfarjani, Yuichi Hashi, Jun Onoe, Kazuo Takeuchi, and Yoshiyuki Kawazoe, *Vibrational modes and IR analysis of neutral photopolymerized C_{60} dimers*, Phys. Rev. B **57(1)**, 223–229 (Jan 1998).
- [216] Shigeru Tsukamoto and Tomonobu Nakayama, *First-principles electronic structure calculations for peanut-shaped C_{120} molecules*, Science and Technology of Advanced Materials **5(5-6)**, 617–620 (2004).
- [217] Douglas L. Strout, Robert L. Murry, Chunhui Xu, Wade C. Eckhoff, Gregory K. Odom, and Gustavo E. Scuseria, *A theoretical study of buckminsterfullerene reaction products: $C_{60} + C_{60}$* , Chem. Phys. Lett. **576**, 214 (1993).
- [218] R. Schmidt, V. D. Toneev, and G. Wolschin, *Mass transport and dynamics of the relative motion in deeply inelastic heavy-ion collisions*, Nuclear Physics A **311(1-2)**, 247 – 263 (1978).
- [219] H. Haken and H. C. Wolf, *Molekülphysik und Quantenchemie*, Springer-Verlag (1992).
- [220] X. Q. Wang, C. Z. Wang, and K. M. Ho, *Vibrational modes in C_{70} : A first-principles study*, Phys. Rev. B **51(13)**, 8656–8659 (Apr 1995).
- [221] D. R. McKenzie, C. A. Davis, D. J. H. Cockayne, D. A. Muller, and A. M. Vassallo, *The structure of the C_{70} molecule*, Nature **622**, 355 (1992).
- [222] Alexander V. Nikolaev, T. John S. Dennis, Kosmas Prassides, and Alan K. Soper, *Molecular structure of the C_{70} fullerene*, Chemical Physics Letters **223(3)**, 143 – 148 (1994).
- [223] K.-A. Wang, A. M. Rao, P. C. Eklund, M. S. Dresselhaus, and G. Dresselhaus, *Observation of higher-order infrared modes in solid C_{60} films*, Phys. Rev. B **48(15)**, 11375–11380 (Oct 1993).
- [224] P. Bowmar, W. Hayes, M. Kurmoo, P. A. Pattenden, M. A. Green, P. Day, and K. Kikuchi, *Raman and infrared determination of vibrational fundamentals of single-crystal C_{60} and derivatives and of C_{70}* , J. Phys. Condens. Matter **6**, 3161 (1994).
- [225] Giovanni Onida, Wanda Andreoni, Jorge Kohanoff, and Michele Parrinello, *Ab initio molecular dynamics of C_{70} . Intramolecular vibrations and zero-point motion effects*, Chemical Physics Letters **219(1-2)**, 1 – 7 (1994).
- [226] R. .E. Stratmann, G. E. Scuseria, and M. J. Frisch, *Density Functional Study of the Infrared Vibrational Spectra of C_{70}* , J. Raman Spectr. **29**, 483–487 (1999).
- [227] L. Chen, B. Wei, J. Bernard, R. Brédy, and S. Martin, *Nuclear-stopping-induced fast multifragmentation in $Ar^+ - C_{60}$ collisions*, Phys. Rev. A **71(4)**, 043201 (Apr 2005).

-
- [228] J. B. Krieger, Yan Li, and G. J. Iafrate, *Derivation and application of an accurate Kohn-Sham potential with integer discontinuity*, Physics Letters A **146(5)**, 256 – 260 (1990).
- [229] X. Chu and S. I. Chu, *Self-interaction-free time-dependent density-functional theory for molecular processes in strong fields: High-order harmonic generation of H_2 in intense laser fields*, Phys. Rev. A **63(2)**, 023411 (2001).
- [230] R. van Leeuwen and E. J. Baerends, *Exchange-correlation potential with correct asymptotic behavior*, Phys. Rev. A **49(4)**, 2421–2431 (Apr 1994).
- [231] P. R. T. Schipper, O. V. Gritsenko, S. J. A. van Gisbergen, and E. J. Baerends, *Molecular calculations of excitation energies and (hyper)polarizabilities with a statistical average of orbital model exchange-correlation potentials*, The Journal of Chemical Physics **112(3)**, 1344–1352 (2000).
- [232] I. V. Hertel, I. Shchatsinin, T. Laarmann, N. Zhavoronkov, H.-H. Ritze, and C. P. Schulz, *Fragmentation and Ionization Dynamics of C_{60} in Elliptically Polarized Femtosecond Laser Fields*, Physical Review Letters **102(2)**, 023003 (2009).
- [233] I. Shchatsinin, H.-H. Ritze, C. P. Schulz, and I. V. Hertel, *Multiphoton excitation and ionization by elliptically polarized, intense short laser pulses: Recognizing multielectron dynamics and doorway states in C_{60} vs. Xe* , Phys. Rev. A **79(5)**, 053414 (2009).
- [234] M. Fischer, J. Handt, and R. Schmidt, in progress.
- [235] Altarelli, *Xfel technical design report. Technical report. DESY* (2006).
- [236] H. Wabnitz, L. Bittner, A. R. B. de Castro, R. Dohrmann, P. Gurtler, T. Laarmann, W. Laasch, J. Schulz, A. Swiderski, K. von Haefen, T. Moller, B. Faatz, A. Fateev, J. Feldhaus, C. Gerth, U. Hahn, E. Saldin, E. Schneidmiller, K. Sytchev, K. Tiedtke, R. Treusch, and M. Yurkov, *Multiple ionization of atom clusters by intense soft X-rays from a free-electron laser*, Nature **420**, 482 (2002).
- [237] Ulf Saalman and Jan-Michael Rost, *Ionization of Clusters in Strong X-Ray Laser Pulses*, Phys. Rev. Lett. **89(14)**, 143401 (2002).
- [238] Christian Siedschlag and Jan-Michael Rost, *Small Rare-Gas Clusters in Soft X-Ray Pulses*, Phys. Rev. Lett. **93(4)**, 043402 (2004).
- [239] Christian Gnodtke, Ulf Saalman, and Jan M. Rost, *Ionization and charge migration through strong internal fields in clusters exposed to intense x-ray pulses*, Phys. Rev. A **79(4)**, 041201 (Apr 2009).

-
- [240] Sebastian Krause, *Das Wasserstoffatom im starken VUV-Laserfeld*, Diplomarbeit, TU Dresden (2009).
- [241] T. Burnus, M. A. L. Marques, and E. K. U. Gross, *Time-dependent electron localization function*, Phys. Rev. A **71**, 010501 (2005).
- [242] M.A.L. Marques A. Castro, T. Burnus and E.K.U. Gross, *Time-dependent electron localization function: A tool to visualize and analyze ultrafast processes*, in O. Kün and L. Wöste, editors, *Analysis and Control of Ultrafast Photoinduced Reactions*, volume 87, p. 553, Springer Series in Chemical Physics (2007).
- [243] A. Savin, B. Silvi, and F. Coionna, *Topological analysis of the electron localization function applied to delocalized bonds*, Can. J. Chem. **74**, 1088 (1996).
- [244] Z. H. Dong, P. Zhou, K.-A. Wang, J.M. Holden, P.C. Eklund, M.S. Dresselhaus, and G. Dresselhaus, *Observation of higher-order Raman modes in C₆₀ films*, Phys. Rev. B **48**, 2862 (1993).

Danksagung

An dieser Stelle möchte ich all jenen danken, durch deren Hilfe und Unterstützung diese Arbeit möglich wurde. Ein besonderer Dank gebührt Herrn Prof. Rüdiger Schmidt, der mir die Möglichkeit auf diesem interessanten Gebiet zu promovieren.

Herzlich möchte ich auch dem Max-Planck-Institut für Physik komplexer Systeme (MPI-PKS) bzw. der International Max Planck Research School for "Dynamical Processes in Atoms, Molecules and Solids" für die finanzielle Unterstützung danken. Insbesondere gaben sie mir die Möglichkeit, verschiedenste aktuelle Forschungsgebiete in den internen Seminaren bzw. an verschiedenen Sommer-/und Winterschulen kennenzulernen, die mein physikalischen Horizont sehr erweitern konnten.

Einen großen Dank auch an die Gruppe von Herrn Prof. Hertel am Max-Born-Institut Berlin, insbesondere an Tim Laarmann und Claus-Peter Schulz, für die gute Zusammenarbeit in Zusammenhang mit den Laser-Fulleren-Experimenten.

Für das zur Verfügungstellen von Rechnerkapazitäten an den PC-Clustern, danke ich dem Zentrum für Informationsdienste und Hochleistungsrechnen (ZIH) an der TU Dresden und dem MPI-PKS – ohne dies wäre diese Arbeit so nicht möglich gewesen.

Außerdem vielen Dank an die gesamte Arbeitsgruppe, namentlich Frank Großmann, Christoph Goletz, Werner Koch, Sebastian Krause, Martin Winter und Michael Fischer, für die vielen Diskussionen zur Physik, Computerfragen und anderes.

Für das Korrekturlesen der Arbeit danke ich insbesondere Werner Koch, Sebastian Krause, Martin Winter, Michael Fischer und Martin Schlesinger. Weiterhin möchte ich mich bei allen Mitarbeitern des Instituts für Theoretische Physik für die angenehme Arbeitsatmosphäre danken.

Erklärung

Hiermit versichere ich, daß ich die vorliegende Arbeit ohne unzulässige Hilfe Dritter und ohne Benutzung anderer als der angegebenen Hilfsmittel angefertigt habe. Die aus fremden Quellen direkt oder indirekt übernommenen Gedanken sind als solche kenntlich gemacht. Die Arbeit wurde bisher weder im Inland noch im Ausland in gleicher oder ähnlicher Form einer anderen Prüfungsbehörde vorgelegt.

Die vorliegende Arbeit habe ich unter Betreuung von Prof. Rüdiger Schmidt am Institut für Theoretische Physik angefertigt. Ich erkenne die Promotionsordnung der Fakultät Mathematik und Naturwissenschaften an der Technische Universität Dresden vom 20. März 2000 an.

Dresden, den 15.01.2010

Jan Handt